Title
Induced Nanoscale Curvature Localizes Endocytic Sites and Rescues Clathrin Knockdown

Author
Cail, Robert

Publication Date
2021

Peer reviewed|Thesis/dissertation

Induced Nanoscale Curvature Localizes Endocytic Sites and Rescues Clathrin Knockdown

By

Robert Caleb Cail

A dissertation submitted in partial satisfaction of the

requirements for the degree of

Doctor of Philosophy

in

Biophysics

in the

Graduate Division

of the

University of California, Berkeley

Committee in charge:

Professor David Drubin, Chair
Professor James Hurley
Professor James Olzmann
Professor Roberto Zoncu

Fall 2021

Abstract

Induced Nanoscale Curvature Localizes Endocytic Sites and Rescues Clathrin Knockdown

by

Robert Caleb Cail

Doctor of Philosophy in Biophysics

University of California, Berkeley

Professor David Drubin, Chair

Clathrin-mediated endocytosis (CME) depends on plasma membrane remodeling, which results in production of an endocytic vesicle approximately 100 nm across. Remodeling of a flat patch of membrane into a spherical vesicle occurs below the resolution limit of the light microscope, making elucidation of the molecular mechanisms underlying this shape change difficult. To study how the cell generates nanoscale curvature for CME, I developed a high-throughput nanofabrication process that mimics endocytic membrane curvature, and focused on how this curvature affects both normal and perturbed CME. I began by producing a mold with nanoscale ridges (nanoridges) through electron-beam lithography and reactive ion etching, and characterized the mold to ensure suitable structures were formed. I then used the mold to optimize a UV-nanoimprint lithography method of stamp-and-lift substrate manufacturing, allowing the production of one glass-like substrate every ~15 minutes. I characterized the substrates and verified that they induce a cellular response by reliably bending the ventral cell membrane into curved shapes and by reorganizing the endocytic machinery along the sites of high induced curvature.

To determine how induced plasma membrane curvature affects endocytosis, I screened genome-edited cells expressing fluorescent CME proteins or fluorescent membrane markers and developed computational tools to quantify the enrichment of endocytic proteins on curved membranes, finding that proteins across stages of CME are strongly enriched by the highest curvature induced by our substrates (75 nm ridge diameter). I then characterized the response of endocytic sites to induced curvature, finding an increase in endocytic lifetimes with high curvature that decreases as the curvature decreases, as well as an increase in mean-square displacement of endocytic sites on nanoridges specifically at late stages of CME, while the fluorescence profiles of CME proteins on nanoridges were indistinguishable from control cells.

Finally, I chose to examine how protein disruptions affected endocytosis on flat Ormocomp substrates, and whether induced curvature might rescue the resulting perturbations to CME. I found that induced curvature did not rescue CME from AP2 or FCHo1/2 knockdown, indicating that stable curvature cannot bypass nucleation or early stabilization of cargo-adaptor interactions. However, AP2 localizes to nanoridges even in the absence of FCHo1/2, thought to be key stabilizers of AP2, evidence that AP2 has some intrinsic affinity for high membrane curvature. I found that induced curvature rescues endocytic site localization after clathrin

disruption, evidence that clathrin's essential function in CME is curvature stabilization. I further characterized these clathrin-knockdown sites on regions of induced membrane curvature and found that the sites turn over with a nearly identical fluorescence intensity profiles to sites in control cells, albeit with a longer lifetime, and found that endocytic cargo uptake was partially rescued by induced curvature in clathrin knockdown cells. With these data, I put forward a model in which clathrin's key role at an endocytic site is to stabilize the evolving curvature, but that with induced curvature, an endocytic site may proceed to scission without a coat. Indeed, I found evidence through electron microscopy for formation of exactly such vesicles in clathrin-knockdown cells grown on nanofabricated ridges. These data demonstrate the fundamental importance of membrane shape in control of cell biological processes, examples of which are predicted to include endocytosis of ECM proteins and viral particles.

Dedicated To
My parents, who gave me the chance,
All my labmates, who showed me how,
David Drubin, who taught me everything I know about science,
And Brendan, who saw me through it all.

TABLE OF CONTENTS

Chapter 1: Cell membrane curvature as a signal for biochemical processes
Introduction……..1
Energetics of membrane curvature……..1
Equilibrium effects: Membrane curvature drives protein affinity……...7
Consequences of curvature on chemical kinetics……..11
An integrated view: curvature as a control mechanism in complex processes……...13
Outstanding questions in membrane curvature……..15
Mechanisms of curvature evolution in CME……15

Chapter 2: Electron-beam lithography/UV-nanoimprint lithography as a method of microscopy substrate manufacturing
Introduction to Lithography……...17
Nanofabrication: theory and methods……19
Electron-Beam Lithography……...22
Overview of substrate nanofabrication process……23
UV-NIL for biological experiments……...24

Chapter 3: Endocytic sites localize to nanoridge substrates as a function of curvature, altering endocytic kinetics but not other parameters
The cellular response to induced curvature……...30
Endocytic proteins localize to substrates as a function of curvature……33
Endocytic sites on nanoridges are valid CCPs with increased lifetime……41

Chapter 4: Clathrin disruption, but not other disruptions, is rescued by induced curvature
Background……....50
Nucleation stage: AP2 knockdown is not rescued by induced curvature……..52
Stabilization stage: FCHo1/2 knockdown is not rescued by induced curvature, but AP2 still localizes to regions of high curvature……50
Invagination module: Clathrin knockdown is rescued by induced curvature……....55
Curvature-rescued clathrin KD sites are dynamic with longer lifetimes……...58

Chapter 5: Conclusions and future directions
Outstanding questions about Ormocomp substrates……..65
Questions concerning CCP characteristics and disruptions to CME……66
In vitro generation of supported lipid bilayers on curved substrates can answer novel questions in biophysics……..67
Other curvature-dependent processes on substrates……....69

References……..71

List of Figures

Figure 1.1: Curvature of cell membranes
Figure 1.2: Methods of studying curvature
Figure 1.3: Binding constants are a function of curvature
Figure 1.4: Effect of curvature on chemical kinetics
Figure 1.5: Curvature integrates signals and commits a process to completion

Figure 2.1: Lithography depends on differential reactions
Figure 2.2: Soft lithography as stamp-and-expose system
Figure 2.3: Planar processing and top-down/bottom-up lithography
Figure 2.4: Electron beam lithography
Figure 2.5: Chemical etching vs reactive ion etching
Figure 2.6: Ormocomp substrate manufacturing
Figure 2.7: Ormocomp's properties for TIRF microscopy
Figure 2.8: Ormocomp nanoridges by SEM and cellular response to nanoridges

Figure 3.1: Hypothesis of induced curvature in CME
Figure 3.2: SKMEL2 cellular response to nanoridges
Figure 3.3: MDA-MB-231 cellular response to nanoridges
Figure 3.4: Thin-section TEM of nanoridges to measure membrane curvature
Figure 3.5: TIRF microscopy on Ormocomp ridges
Figure 3.6: Survey of endocytic proteins on nanoridges
Figure 3.7: Cell membrane area increase on nanoridges
Figure 3.8: Enrichment score for endocytic proteins
Figure 3.9: Dynamics of CME sites on induced curvature
Figure 3.10: Fluorescence intensity of AP2/CLTA on nanoridges
Figure 3.11: Characterization of CCPs on substrates
Figure 3.12: Unroofed cells bear curvature-sensing response

Figure 4.1: Modular nature of CME
Figure 4.2: AP2 KD is not rescued by nanoridges
Figure 4.3: Decrease in endocytic puncta after AP2 KD
Figure 4.4: Decrease of CCP number and lifetime after FCHo1/2 knockdown
Figure 4.5: Clathrin knockdown is rescued by induced curvature
Figure 4.6: Clathrin knockdown sites are canonical endocytic sites with longer lifetimes
Figure 4.7: Uptake of fluorescent transferrin after knockdowns
Figure 4.8: Trafficked transferrin after clathrin knockdown

Common abbreviations

CME: Clathrin-mediated endocytosis
CCP/CCV: Clathrin-coated pit/clathrin-coated vesicle
AP2: Adaptor protein 2
DNM2: Dyamin2
CLTA: Clathrin light chain A
CLTC/CHC: Clathrin heavy chain
FCHo1/2: F-BAR containing, Cip4-Homology proteins 1 and 2
Tfn: Transferrin
GFP/RFP: Green fluorescent protein/red fluorescent protein
PIP_2: Phosphatidylinositol 4,5-bisphosphate
GUV/SUV: Giant unilamellar vesicle/small unilamellar vesicle
EBL: Electron-beam lithography
RIE: Reactive-ion etching
ICP: Inductively-coupled plasma
UV-NIL: Ultraviolet nanoimprint lithography

Acknowledgements

I would like to express my deepest gratitude to so many people who helped me along the way: In the Drubin/Barnes lab, every amazing member of the lab helped me throughout graduate school but I must especially emphasize my gratitude to Charlotte Kaplan, Matthew Akamatsu, Daniel Serwas, Julian Hassinger, Ross Pedersen, Zane Bergman, Julia Torvi, Cyna Shirazinejad, Meiyan Jin, and Paul Marchando, who guided me, advised me, helped me with experiments, and generally were a joy to work with. At the UC Berkeley EM lab, I must thank Danielle Jurgens, Guangwei Min, and Reena Zalpuri for their assistance with electron microscopy. From the Molecular Foundry at LBL, I must thank Stefano Cabrini, Giuseppe Calefiore, Stefano Dallorto, Daniel Staaks, Michael Elowson, and Scott Dhuey for a million assistances in training, technical support, and general nanofabrication help. The entirety of the Hurley lab and Groves lab were very helpful with advice and ideas, and the whole UC Berkeley Biophysics Graduate Group was a wonderfully supportive group, no one more than Kate Chase. A huge thank you goes to my thesis committee, for their help in my qualifying exam and onwards, with wonderful advice and assistance--especially Jim Hurley, who has been a great mentor to me through the years. And finally, I must say the biggest thank you to David Drubin, who has been a fantastic advisor, dedicating so many hours of his time to my scientific betterment. I thank you all for all the personal, scientific, and professional help. I wouldn't have made it through without each of these people.

Chapter 1

Cell membrane curvature, during endocytosis and beyond, is a signal for biochemical processes

Cells live and move in a three-dimensional world, interacting with and constrained by the shapes of their environment. A key parameter in human physiology is the ability of the cell to both produce and respond to 3-dimensional shape, across size scales; for instance, cells must press the membrane forward to migrate, and in doing so must induce specific protrusions to move around obstacles, or respond to a neighboring cell forming such protrusions (Zhao et al., 2012; Sitarska et al., 2021; Hayer et al., 2016). Managing these feats of growth, migration, and homeostasis in shape-dependent contexts requires cross-talk between membrane shape and biochemical activity, with chemical cues causing physical changes and physical cues driving chemical reactions (Baumgart et al., 2011). In this chapter, I focus on membrane curvature, where it comes from, and how it serves as a mechanistic signal in biology. I will explain curvature across size scales and explore how it acts as a signal source in various cell biological processes, from migration to division to endocytosis. I will dissect some of the causes and consequences of curvature as a biological signal. I will then focus on molecular mechanisms in clathrin-mediated endocytosis, which requires a progression of curvature from flat to spherical membrane within a short time and with high physical constraints.

Introduction

Curvature as a mathematical concept is a quantitative measure of how closely a surface approximates a sphere, and what the radius of said sphere would be (Fig 1.1A). The measure of curvature of a sphere is the inverse of its radius, or 1/R, and thus has units of m^-1. For the sake of non-spherical biological membranes, curvature can typically be treated to satisfactory accuracy by locally defining two parameters: the two principal curvatures. If one projects the maximum radius and minimum radius of the shape onto planes, then the principal curvatures are the inverses of the radii of the two circles resulting from this projection.

The curvature of a membrane can be quantified in two main ways, each of which presents advantages for certain situations (Fig 1.1B). The *Guassian curvature* (K) is the product of the two principal curvatures, while the *mean curvature* (H) is the arithmetic mean of the two principal curvatures. Gaussian curvature is a simple quantification of how closely a surface resembles a sphere (for positive values) or a saddle (for negative values). Positive and negative Gaussian curvature appear throughout the cell and across scales, for instance in COPII-coated vesicle transport from the ER to the Golgi, where the protein Sar1 induces a spherical bud that forms on the ER (Lee et al., 2005). However, whenever one direction has no curvature, the Gaussian curvature term disappears. Thus, for shapes such as a cylinder, which appear throughout biology from bacillus bacteria to filopodial membrane protrusions, the Gaussian curvature is zero, but the mean curvature reveals that the membrane is still bent (Faix and Rottner, 2006; Bratton et al., 2018).

Energetics of membrane curvature

Lipid bilayer curvature is an intrinsic property dictated by the composition of the bilayer (Fig 1.1C). For perfectly homogenous DOPC membranes reconstituted *in vitro,* there is no intrinsic curvature because of the ideal packing of lipid tails and head groups (Schmidt et al., 2012).

However, upon introduction of more complex (and realistic) membrane chemistries, the equilibrium state of the bilayer changes. PIP_2, with its bulky head group and large number of negative charges, induces positive curvature on the leaflet on which it appears; this is coupled to negative curvature on the other leaflet "beneath" the PIP_2 (Shukla et al., 2019). The tail groups of lipids can also influence their effects on bilayer curvature: while DOPC bears an essentially cylindrical shape, allowing for even packing, introduction of other tail domains creates positive or negative curvature based on their wedge- or cone-like shapes, respectively. For instance, lipids with one mono-unsaturated tail domain, such as POPE, create a kink in the tail leading to a more conical shape, inducing a wedge and therefore locally negative curvature (Snead et al., 2014).

Transitions away from the equilibrium curvature of a lipid bilayer require energetic input (Baumgart et al., 2014). Helfrich (1973) employed a continuum mechanics model and elastic theory to derive a commonly-used physical model of the lipid bilayer, in which there is a cost to inducing both Gaussian and mean curvatures according to the following equation:

$$f_c = \frac{k_c}{2}(2H - c_0)^2 + k_G K$$

Where f_c is the energy per unit area, k_c and k_G are the bending rigidities for mean and Gaussian curvature respectively, c_0 is the initial curvature of the membrane, and H and K are the mean and Gaussian curvatures of the final shape. Integrating this equation over the area of the membrane in question yields the Helfrich Free Energy (F_H), a measure of the total energetic input required to create a desired shape.

To create a spherical vesicle from an initially flat membrane, this equation can be reduced. The initial curvature, c_0, is zero for flat membranes. To make a radially symmetric, spherical vesicle, the integral over the area dA is simply the surface area of a sphere, or $4\pi R^2$. If one makes the simplifying assumption that the mean and Gaussian bending rigidities are equivalent (ie, there is the same penalty for bending in each direction, and this rigidity is K_B), this integral reduces to the following:

$$\frac{K_B}{2}\int(\frac{2}{R})^2 dA = \frac{K_B}{2} * \frac{4}{R^2} * 4\pi R^2$$

Which is equal to $8\pi K_B$. Thus, creating a spherical vesicle from a flat membrane is independent of the radius of the desired sphere. K_B is typically around 20-30 K_bT, where K_b is the Boltzmann constant and T the temperature, so the total energetic requirement of vesiculation is on the order of 500 K_bT, which corresponds to hydrolysis of approximately 20 ATP molecules (Milo and Phillips, 2015). Thus, the energy required to create a spherical vesicle (under low turgor pressure, as is present in mammalian cells) is relatively low, and the difficult parts from a cellular perspective are efficient selection of sites/cargoes, coordination of correct membrane size to bend, and assembly of bending machinery to create curvature.

Establishing and maintaining curvature

The cell employs various mechanisms to achieve membrane bending, across scales ranging from nanometers to tens of microns (Antonny, 2011; McMahon and Gallop, 2005) (Fig 1.1D). Direct insertion of transmembrane proteins, lipidated amino acids, or amphipathic helices creates localized bending in the membrane. Direct and indirect scaffolding, in which shaped proteins like the banana-shaped BAR domain bind to the membrane and induce bending to conform to their structure, can create larger and longer-lasting membrane shapes. Force production from

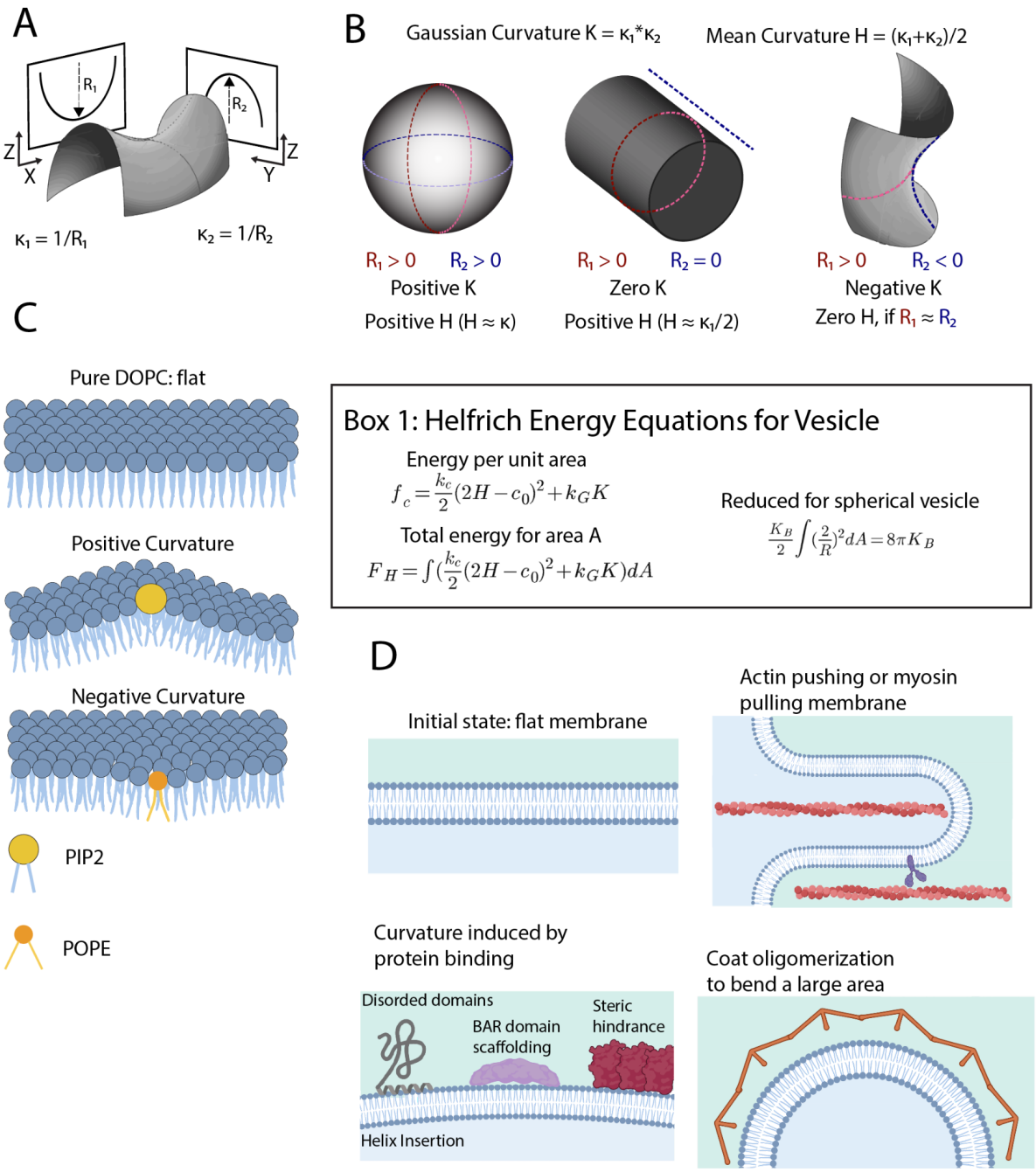

Figure 1.1: Curvature of cell membranes. A) Principal curvatures are determined from the maximum radii of the circles that can be projected onto planes from the shape of interest. B) Gaussian and mean curvatures are the product and average, respectively, of the principal radii for the shape of interest. C) Cell membranes have intrinsic curvatures as a consequence of their lipid makeups. D) Proteins create curvature through various direct (membrane attachment, actomyosin/kinesin force production) or indirect (coat scaffolding) mechanisms to produce shapes for various downstream purposes.

cytoskeletal filaments pushing (in the case of actin) or pulling (in the case of kinesin and myosin) consume ATP to create invaginations. One common theme in membrane curvature is the dependence on oligomerization of protein subunits to coordinate shape changes on scales larger than an individual protein; for instance, septins, a cytoskeletal filament, can sense curvature on the order of 1 micron diameter, which is 100 times larger than an individual septin filament (Bridges et al, 2016). The septins achieve this curvature-sensitivity by inserting an amphipathic helix into the membrane, which is essential for local curvature changes, but require large-scale oligomerization to sense the full micron-scale curvature (Cannon et al., 2019).

Methods to study curvature

In vitro systems have various methods for creating both Gaussian and non-Gaussian curvatures in equilibrium and non-equilibrium states. These methods have yielded enormous biophysical insights into curvature generation and sensation (Fig 1.2A).

To create equilibrium-state positive Gaussian curvature, one can simply create spherical lipid vesicles of a given radius and therefore known curvature. Typically, small unilamellar vesicles (SUVs) are employed in this research, with sizes of 200 nm and less (Lin et al., 2012). These vesicles can be fed into a pelleting assay to determine binding affinities of proteins to given curvatures, or directly visualized on a microscope to monitor affinity in real time (Faúndez et al., 1998). For instance, using a substrate tether, the Stachowiak lab developed a method to attach SUVs to a microscope slide and measure the relative affinity of different proteins involved in CME for vesicles (Snead and Stachowiak, 2018). Using this system, they found that proteins across the stages of CME have higher affinity for lipids at smaller radius, and they discovered the previously unappreciated contribution of intrinsically disordered domains (IDDs) in sensing high curvature (Busch et al., 2015; Zeno et al., 2018; Zeno et al., 2021) . Larger-scale vesicles, such as the giant unilamellar vesicle (GUV), have been employed to study curvature generation with reconstituted systems, as in the induction of negative-curvature tubules by the ESCRT complex to concentrate cargoes, or the I-BAR protein IRSp53, preferentially localizing the HIV-1 Gag protein as a key step in viral egress (Wollert and Hurley, 2010; Inamdar et al., 2021). An advantage of GUV systems is the ability to create localized highly positive or highly negative curvature by selectively localizing proteins inside or outside the GUV, which, due to its large size, is essentially flat on the scale of individual protein subunits (Baumgart et al., 2011).

GUV systems also allow for precise, nanoscale control of mean and Gaussian curvature creation from the surface of the vesicle. While the tension of these artificial membranes is generally much lower than the tension of live human cells, the ease of controlling their chemical characteristics, and their controlled deformability, allow creation of specific membrane shapes (Tian and Baumgart, 2009). By using an optical trap to pull a membrane tubule, known as a membrane tether, from a GUV, curvatures on the order of an endocytic vesicle (<100 nm) can be induced. The extent of mean curvature is controlled by altering the pressure on the vesicle, allowing for thinner or thicker membrane tubules, according to the Laplace equation (Waugh et al., 1992). Membrane tether systems can be monitored on fluorescence microscopes while controlling membrane shape, allowing for both high specificity and sensitivity of biochemical and physical parameters. Interestingly, for low-tension membranes, the highest energetic barrier is to create the initial tether exvagination from the GUV; once a tubule is pulled out, a lower, constant force exertion extends the tether and therefore lengthens the tubule (Koster et al., 2005). This property

indicates that the necessary energetic transition is in the formation of the initial spherical shape, and that there is a reservoir of bilayer lipids that allows for flow along a tubule. These systems have been employed in the study of positive-curvature systems such as the N-BAR domain, negative-curvature systems such as the I-BAR, or transmembrane proteins such as the bacterial ion channel (Ayton et al., 2009; Prévost et al., 2015; Aimon et al., 2014). Studies using GUV tethers provide unique insights into curvature preference and molecular mechanisms of protein activity, such as dynamin's GTPase-coupled membrane scission mechanism (Roux et al., 2010).

The production of curvature from supported lipid bilayers (SLBs) is also an attractive approach for membrane studies. Formation of supported lipid bilayers on glass coverslips with inward invaginations creates localized negative curvature, and has been shown to induce the localization of the ESCRT complex, specifically at the neck of the invagination at a specific interface of negative membrane curvature (Lee et al., 2015). However, producing nanofabricated glass is complex, with few labs having access to the machinery required. SLBs on glass beads also create nanoscale curvature with high precision, and using relatively unadhered or "floppy" membranes allows the production of membrane tubules from SLBs on flat glass surfaces or beads, creating nanoscale curvature easily but at the expense of some precision relative to nanofabricated surfaces (Mornet et al., 2005; Dar et al., 2017).

While studies of reconstituted vesicles and lipid bilayers have provided many molecular insights, such studies lack the full complexity of living cells. In contrast, inducing curvature in *in vivo* systems allows for cellular context to be included in tandem with membrane curvature. For instance, growing cells on a nanopillar array induces curvature on the size scale of a single endocytic site, and induces the localization and turnover of AP2, dynamin2, clathrin, and many other endocytic proteins (Zhao et al., 2017). Additionally, formation of Giant Plasma Membrane Vesicles, or GPMVs, creates GUV-like vesicles with endogenous cell membrane compositions and many cytoplasmic elements of the live cell contained within them (Baumgart et al., 2007). These vesicles can be studied using similar methods to fully reconstituted GUVs, such as membrane tethers, allowing a combination approach for precise control of size and shape with more complete cellular context present (Moreno-Pescador et al., 2019). Together, these systems have been highly useful in cataloging the protein's response to membrane curvature and the capacity of proteins to influence the membrane physically and chemically. Clever combinations of *in vitro* and *in vivo* curvature studies will continue to provide biophysical insights of membrane remodeling and scission.

Inducing or sensing: a question of scale

The question of whether a protein induces or senses curvature is one that persists within cell biology (Fig 1.2B) (McMahon and Boucrot, 2015). In reconstituted systems, the division is frequently a function of protein concentration within the model system: at low concentrations, the proteins such as amphiphysin *sense* curvature by preferentially localizing to higher-curvature areas over lower-curvature ones (Busch et al., 2015). Above some threshold of critical concentration, however, proteins *induce* curvature by forcing the membrane into their preferred radius (Blood and Voth, 2006). Thus, a protein might take two paths to shaping the membrane beneath it: by first binding to flat membrane, then imposing a curvature, or by binding to an already-curved membrane (curved through the previous templating of curvature by some other active mechanism, or by thermal fluctuations). In either case, the Gibbs energy released by the

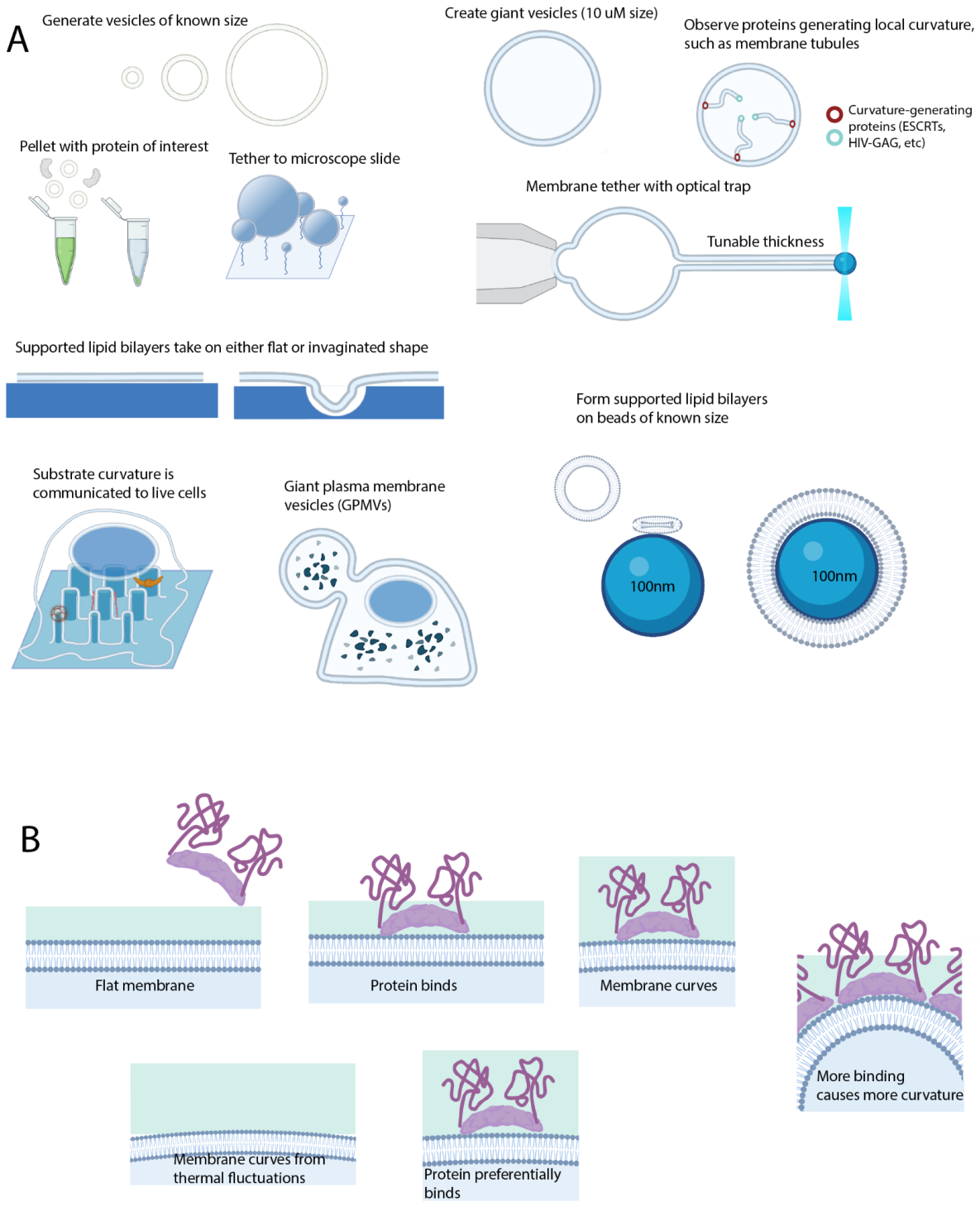

Figure 1.2: Methods of studying curvature. A) *In vitro* methods to generate curvature including vesicle formation (and assays with vesicles of various specific sizes), supported lipid bilayer (SLB) formation with templated shapes, and cultured-cell induced curvature methods. B) The process of curvature formation from a protein either binding to a flat membrane and inducing curvature (top) or binding to a pre-curved membrane (bottom). The Gibbs energy change is the same from either mode of curvature formation, and forming stable curvature requires multiple protein copies.

binding of the protein to the membrane would be equivalent because the enthalpy change is independent of the path taken. Viewed through this lens, the ability to induce curvature is a function of the Gibbs free energy change from multiple protein-membrane interactions being sufficient to overcome the tension of the membrane such that the protein-membrane interactions win out and the membrane bends (Stachowiak et al., 2013). Determining how the interaction between curvature sensing and curvature generating plays out within the cell, during dynamic processes like mitochondrial division or endosomal budding where the protein copy number is low, is an important area of active research. Sensing curvature and generating curvature are not mutually exclusive, as initial curvature generation by one molecule promotes binding by more of the same protein type, in a positive feedback loop.

Equilibrium effects: Membrane curvature drives protein affinity

Specific curvatures *in vitro* and *in vivo* drive the localization of proteins (Fig 1.3A). *In vitro*, the bacterial ion channel KvAP preferentially sorts into membrane tubules with highest affinity for a tubule of radius 7nm, whereas the integral membrane protein AQP0 evenly sorts to membranes irrespective of curvature (Aimon et al., 2014). *In vivo*, the bacterial actin-related protein MreB creates filaments that preferentially localize along the high mean curvature sides of an E. coli cell, and this curvature-sensitive formation is essential for synthesis of the cell wall and correct cell division after budding (Hussain et al., 2018). Table 1 contains a non-exhaustive list of proteins that have been shown, *in vitro* and *in vivo*, to have affinity for membranes of a particular curvature.

Protein binding drives membrane curvature

Conversely, there are many examples of protein binding to the membrane and inducing curvature, through well-mapped mechanisms (Fig 1.3B). SNARE proteins are a well-studied example: through their coiled-coil formation, activated by SNARE-containing membranes in close proximity, SNAREs induce membrane fusion and result in a high-positive-curvature tubule structure (Dhara et al., 2020). The shiga toxin protein induces membrane tubules after infection, in a manner dependent on actin polymerization and the tryptophan at residue 34 (Römer et al., 2007). The COPII complex on purified membranes produces a bead-necklace phenotype of positive Gaussian curvature on membrane tubules, indicating an important transitional step between mean and Gaussian positive curvatures (Bacia et al., 2011). Thus, there is cross-talk between membrane curvature and protein binding, with binding both relying on and resulting in membrane curvature: the physical and chemical processes are strongly related to each other.

The Hill Coefficient is a function of curvature

To understand the extent of membrane shape effects on protein binding, biochemists employ equilibrium-state measurements of protein-ligand interactions such as the Hill equation (Heck 1971):

$$\theta = \frac{[\mathrm{L}]^n}{K_d + [\mathrm{L}]^n}$$

Where θ is the fraction of ligand-bound binding sites, [L] is the concentration of ligand, K_d is the dissociation constant, and n is the Hill coefficient. The Hill coefficient changes as a function of

substrate shape: for instance, the value of n for Cytochrome c doubles from 2.2 to 4.4 as the membrane takes on negative Gaussian curvature (Elmer-Dixon et al., 2020). Clathrin itself

Table 1: Membrane proteins with affinity for curvature

Protein	Preferred Radius	Type of Curvature	Method	Citation(s)
amphiphysin/ BIN1/ Endophilin	5-20 nm	Positive mean/ Positive Gaussian	X-ray diffraction, Negative stain EM	Peter et al., 2004, Casal et al., 2006, Farsad et al., 2001
KvAP	18 nm	Positive *or* negative Gaussian	GUV tether assay	Aimon et al., 2014
WAVE complex/	115 nm	Negative Gaussian	Substrate-grown migrating cells	Pipathsouk et al., 2021
ArfGAP1	37 nm	Positive Gaussian	Circular dichroism of purified protein on liposomes	Drin et al., 2007
IRSp53	18 nm	Negative mean	GUV tether assay	Prevost et al., 2015
Megainin	3.4 nm	Positive mean	All-atom simulations	Gómez-Llobregat et al., 2016
Synuclein	7 nm	Positive mean	Purified liposomes	Westphal and Chandra, 2013
CHMP4B	67 nm	Negative Gaussian	Supported lipid bilayers	Lee et al., 2015
EHD2	45 nm	Positive mean	Negative-stain EM	Daumke et al., 2007
PICK1	38 nm	Positive Gaussian	Single-liposome curvature affinity	Herlo et al., 2018

demonstrates a Hill coefficient of at least 6, indicating high cooperativity in its effect on membrane budding, and the dissociation constant is also a function of membrane curvature (Moskowitz et al., 2005; Zeno et al., 2021). With the effect of curvature on n and K_d, it is easy to model the positive feedback loop of curvature on the proportion of ligand-bound binding sites on proteins.

Domains have overlapping or complementary functions in curvature formation

The domain architecture of proteins contributes to the differential response to size and shapes of curvatures (Fig 1.3C). The canonical BAR domain, for instance, is associated with high mean but not Gaussian curvature; attachment of an intrinsically disordered domain, however, causes proteins to prefer Gaussian rather than mean curvature (Snead et al., 2019). This domain architecture is present in many endocytic proteins: FCHo1, FCHo2, FBP17, amphiphysin, BIN1, TOCA1, and SNX9, to name a few proteins, bear these complementary domain structures and participate in membrane reshaping (Dawson et al., 2006). Complementary domain structure has been proposed to act as a mechanism for modulating curvature preference dynamically in live cells: while the intrinsically-disordered region of amphiphysin may assist in clathrin polymerization at positive Gaussian curvature, the BAR domain may assistant in vesicular neck formation and dynamin recruitment to the neck, which has negative Gaussian curvature (Kessels and Qualmann, 2021). How these domains coordinate *in vivo*, where the components function within a network of multiple binding partners, is an emerging topic, especially in clathrin-mediated endocytosis.

Downstream consequences of curvature affinity

The natural affinity of certain proteins for curved membrane surfaces drives sorting of proteins and their downstream binding partners (Fig 1.3D). In autophagy, for instance, the protein PI3KC3 nucleates the formation of the autophagosome membrane, but its localization to the phagophore depends on the curvature-sensing component of the scaffolding protein Barkor/ATG14(L); the coincidence of high membrane curvature and PI(3)P causes enhanced binding of autophagic formation proteins PI3KC3, LC3, and ATG16, enhancing their activity (Fan et al., 2011). Within the pathway for clathrin-mediated endocytosis, the adaptor protein AP2 must become concentrated in a forming clathrin-coated pit to successfully form a vesicle for cargo uptake; AP2 has been demonstrated through superresolution microscopy to prefer 50-nanometer Gaussian curvature, thus enriching cargoes in a curvature-dependent manner (Roy et al., 2021). Thus, the curvature-binding characteristics of one component of a complex can create a sorting mechanism for other subunits within the complex.

The association of curvature-sensing proteins with membranes also affects diffusion, both of lipids and of other proteins, forming a sort of fence to create localized areas of distinct concentration (Fig 1.3E). The yeast BAR domain proteins Syp1, Bzz1, and Rvs161/167 create stable lipid microdomains, blocking the egress of PI lipids from an endocytic site (Zhao et al., 2013). The feedback loop of curvature and non-diffusive microdomain formation has extensive effects on physical parameters like microdomain size, lifetime, and membrane tension (Mahapatra et al., 2021). These effects on sorting and diffusion work in tandem with the Brownian ratchet mechanism of curvature stabilization, in which coat polymerization irreversibly forms stable curvature necessary for downstream activity (Henrichsen et al., 2006).

Figure 1.3: Binding constants are a function of curvature. A) Membrane curvature drives the binding of bacterial proteins KvAP and MreB, which aligns itself along the curved edge of the bacteria and not across it. B) Protein binding of SNAREs, Shigella toxin, or COPII to lipid bilayers drives membrane curvature. C) BAR domains alone create high mean curvature such as the tubule pictured, whereas a BAR domain coupled to an intrinsically disordered protein (present in full-length amphiphysin) creates Gaussian curvature such as a vesicle. D) Example of downstream consequence of curvature-dependent binding on autophagosome formation by activation of PI3K in curvature-sensing mechanism. E) Curvature-dependent binding limits lipid diffusion out of an endocytic site.

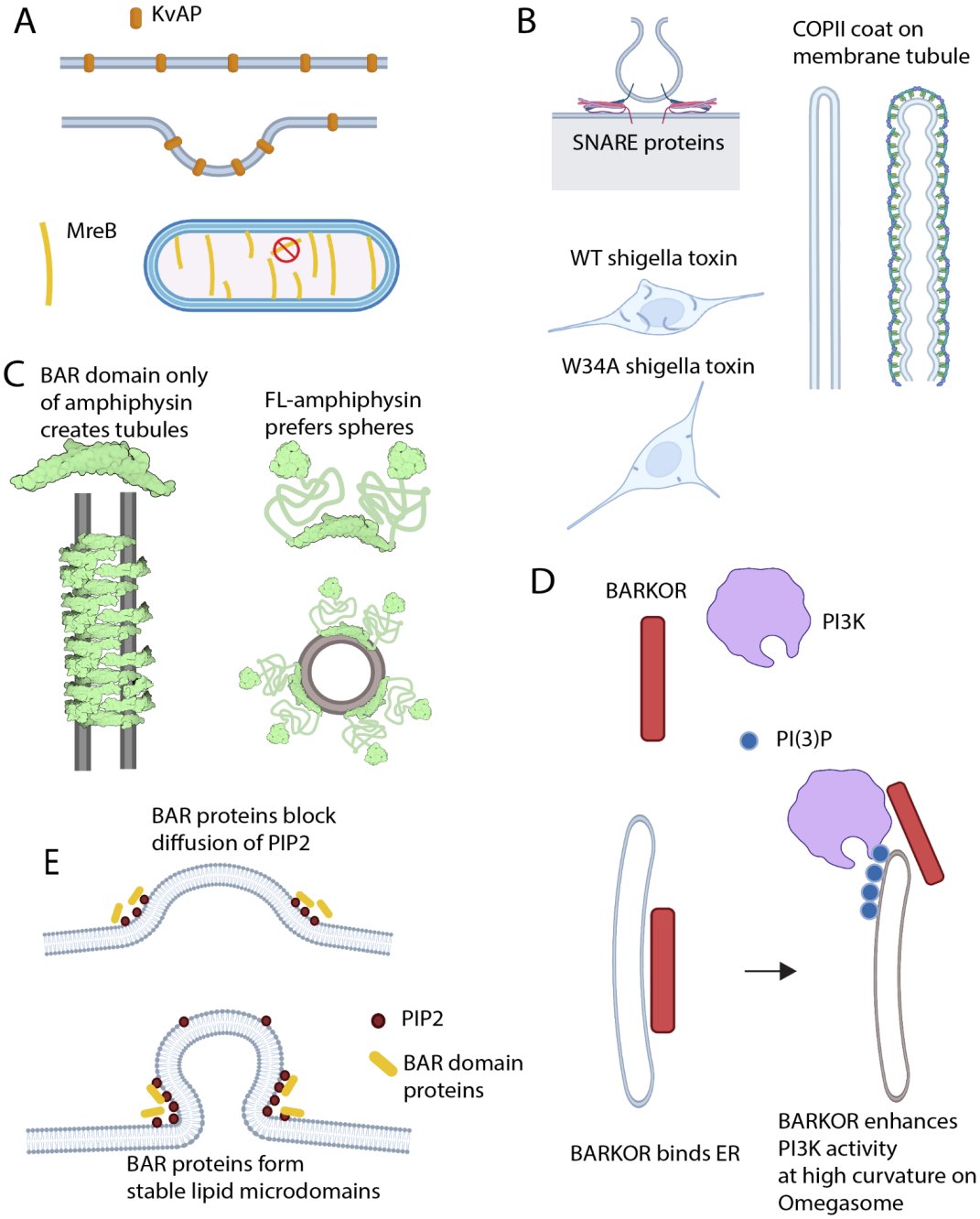

Consequences of curvature on chemical kinetics

In addition to the effect on affinities, measured through equilibrium-state partitioning of curvature-sensing proteins, curvature has been shown to affect enzymatic activity on lipids within membranes (Fig 1.4A). Phosphatidylinositol-specific phospholipase C (PI-PLC) from *Bacillus* organisms has been shown to have higher catalytic activity on membranes of smaller radius, in a manner dependent both on the binding affinity of the enzyme for the membrane and also on the hydrolytic activity of the catalytic site (Wehbi et al., 2003; Ahyayauch et al., 2005). The specificity of the enzyme diacylglycerol kinase epsilon (DGK-epsilon), a key protein in the PI cycle that forms phosphatidic acid from diacylglycerol, is allosterically modulated by high membrane curvature, enhancing its activity on smaller membrane sites and quenching its activity at flatter membranes (Bozelli et al., 2019). The activity of membrane-acting enzymes is at times enhanced by the membrane-sensing properties of binding partners, as in the case of synaptojanin1 hydrolyzing PIP_2 more readily on vesicles of higher curvature, in a mechanism dependent on the curvature-sensing properties of its binding partner endophilin (Chang-Ileto et al., 2012).

This shape-dependent effect can be easily modeled from a collision-theory perspective of enzyme-catalyzed reactions (Fig 1.4B) (Pechukas, 1976). Collision theory posits that the rate constant k_f of a reaction is proportional to the number of collisions between the molecules reacting (Z), the ratio of collisions with the correct orientation (ρ), and the number of collisions with energy above the activation energy barrier (E_a), according to the following equation:

$$k_f = Z\rho e^{\frac{-Ea}{RT}}$$

With curvature-dependent kinetics, both Z and ρ change as a function of shape: there are more collisions on the high-curvature areas of membrane, and with increased access to head groups or the glycerol backbone as the lipids splay apart under curvature, the proportion of collisions with the correct orientation also increases. With these effects, the shape of the substrate can alter the catalysis of enzymes.

Effects of curvature-dependent kinetics in cell biology

Enzymatic control of reactions within the cell integrates local curvature as a signal to turn reactions on or off (Fig 1.4C). For instance, at the Golgi apparatus, the COPI coat assembles and disassembles to control budding of transport vesicles, and this cycle is controlled by the small GTPase Arf1; the GTPase activity of Arf1 is modulated by the curvature of the budding vesicle, which increases the activity of Arf1 by two orders of magnitude, stimulating COPI disassembly specifically at high curvature (Bigay et al., 2003). The switch from inactive to active enzymatic forms with curvature can be driven by conformational changes within the protein, as when ATG3's N-terminal helix becomes structured in the context of high membrane curvature, activating its LC3-conjugating activity specifically in the correct geometry (Fig 1.4D) (Ye et al., 2021). Enzymatic activity can also be switched using a scheme of coincidence detection: clathrin-coated vesicles at the *trans*-Golgi network depend on the coincidence of high curvature and diacylglycerol, which stimulate mechanical force production through the actin cytoskeleton (Anitei et al., 2017).

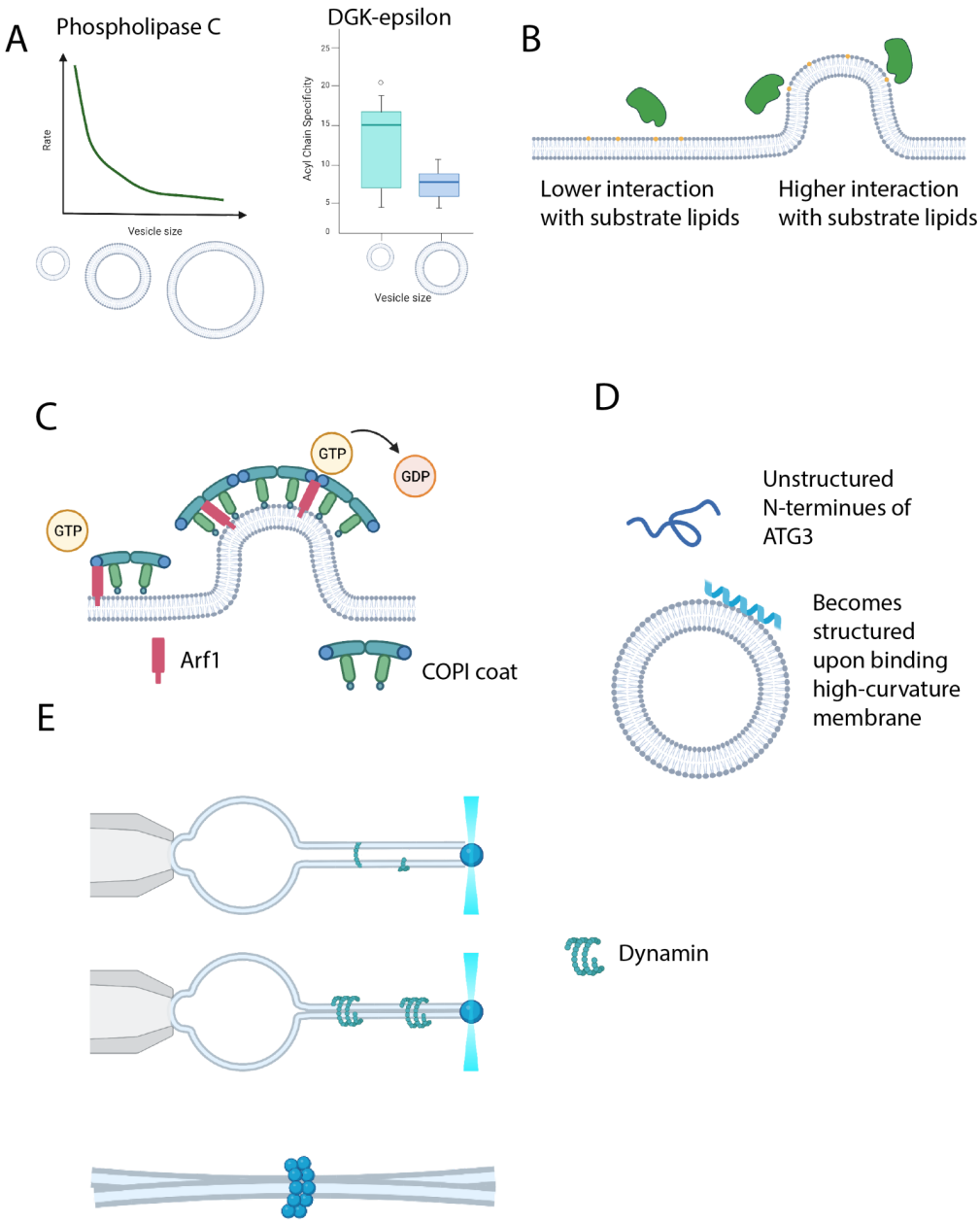

Figure 1.4: Effect of curvature on chemical kinetics. A) Smaller vesicles demonstrate higher rate of PLC activity and higher specificity of diacylglycerol kinase epsilon. B) Principle of curvature-dependent enhancement to collisions between enzyme and its membrane substrate, showing that with head-group splaying from curved membranes more of the substrate is accessible to the enzyme. C) COPI-coat depolymerization is controlled by the small GTPase Arf1, whose kinetic activity is stimulated by highly-curved packed lipids. D) A mechanism of curvature-sensing kinetic control: the N-terminus of the protein ATG3 becomes structured upon binding to high curvature, switching the enzyme into a higher-activity state. E) The special case of dynamin, where both the binding (top) and mechanochemical cycle (bottom) are modulated by curvature, showing both a binding and enzymatic effect of membrane shape.

A special and well-studied case of shape-dependent kinetics is the large GTPase dynamin, illustrative of various mechanisms discussed above (Fig 1.4E). Dynamin is among the few proteins that undergo physical movements after GTP hydrolysis (rather than ATP), and it forms rings around membrane tubules with curvature-sensing affinity (Roux et al., 2010). The GTPase cycle of dynamin is responsible for membrane constriction at the neck of a clathrin-coated pit, leading to vesicle scission. This GTPase activity is present even in purified dynamin/liposome systems (Sweitzer and Hinshaw, 1998). Dynamin's ability to bind to membranes as a function of curvature and undergo autoactivation of its catalytic activity demonstrate how, within one protein, there are multiple steps that depend on curvature as a signal--and how curvature is an essential step in the catalytic process, ensuring that dynamin only operates in the correct context. Other endocytic proteins assist in localizing and activating dynamin, indicating cooperativity in its activity that helps to fine-tune the process of vesicle scission (Meinecke et al., 2013).

An integrated view: curvature as a control mechanism in complex processes

Curvature can work as a signal integration mechanism for controlling the timing of discrete steps within a process, or to commit a process to completion (Fig 1.5). CME is a highly efficient process, with a low failure rate once a nascent site has been marked by adaptor protein/clathrin binding (Doyon et al., 2011; Hong et al., 2015). It has been shown experimentally that actin polymerization in CME is stimulated by the coincidence of high curvature and lipids PI(4,5)P2/PI(3)P (Fig 1.5A) (Deste et al., 2017). Indeed, the species of phosphoinositols present at CCPs varies with the stage of endocytosis, and therefore with curvature (Posor et al., 2015). Endocytosis is a process of curvature evolution over time, so cellular control over this process would naturally integrate signal sources that reflect on progress during CME. In this view, coincidence of curvature and lipid species is a natural timer to signal to the actin machinery that the vesicle has proceeded to the correct stage for internalization.

All chemical reactions are fundamentally stochastic in nature, wherein the rate constants are a statement of the probability of a reaction proceeding. Most dynamic processes within the cell are carried out by a relatively small number of molecules. For instance, there are only two gene copies in most eukaryotic cells and only ~26 dynamin2 molecules are present at the neck of an endocytic site (Elowitz et al., 2002; Grassart et al., 2014). With such small numbers of molecules, stochastic kinetics reign. Noise in a stochastic process is expected to cause high variance in molecular copy numbers. How biochemical reactions consistently produce the same outcome, such as reliably producing vesicles of the same size within a similar time period, is an unresolved question, but it necessarily involves robustness to or dampening of this noise.

In light of the differential affinity and activity that proteins have for the cell membrane as a function of curvature, it has been proposed that membrane curvature acts as a smoothing mechanism to reduce stochastic fluctuations and make enzyme-catalyzed processes more invariant (Fig 1.5B) (Liu et al., 2009). The complex feedback between protein binding, actomyosin force production, lipid hydrolysis, and neck formation are all dependent on the curvature of the endocytic site; introduction of stochastic noise terms to the biochemical equations governing these processes does not appreciably change modeled vesiculation rates. Thus, curvature itself, by controlling reactions within the system, provides robustness to the process of vesicle formation.

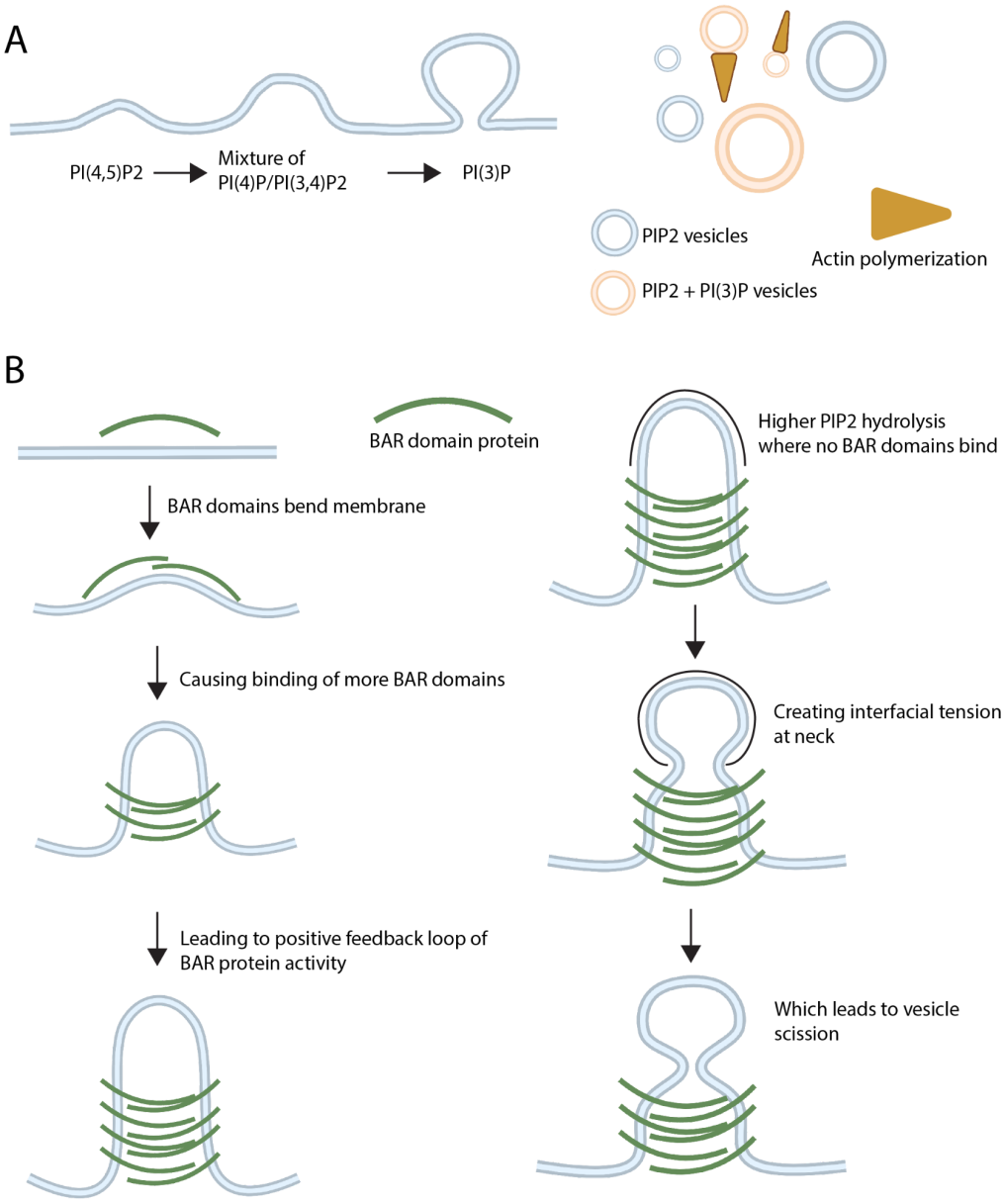

Figure 1.5. Curvature integrates signals and commits processes to completion. A) The lipid species is modulated over time, starting with PI(4,5)P2 but incorporating PI(4)P and PI(3,4)P2 as the 5-phosphate is released, followed by formation of PI(3)P, as the endocytic site internalizes and changes curvature; the lipid species present, along with the size of the vesicle, are both responsible for stimulating polymerization of an actin network, creating a pushing force into the cell. This acts as a timer for force production so that it occurs at a late stage of vesiculation, and commits the endocytic site to trafficking into the cell interior. B) BAR domain assembly on a flat membrane (left) is stochastic at first and then becomes more committed as curvature is formed, reflecting a positive feedback loop mechanism that smooths out the noise of binding and unbinding. Additionally, once the BAR domain proteins have formed a stable scaffold on the membrane (right), they act as a fence to specify regions permissive for PIP2 hydrolysis, leading to interfacial tension and scission at the vesicle neck, making vesiculation more reproducible in size and timing.

Outstanding questions in membrane curvature

While it is now possible to precisely measure affinities and kinetics as a function of membrane curvature, questions remain about how dynamic membrane bending is achieved. In particular, how does the cell dynamically modulate Gaussian curvature vs mean curvature (especially given that individual proteins often show affinity for one type over the other)? How do multi-domain proteins such as amphiphysin manage to bind to both positive and negative Gaussian curvature within the cell? How does the cell precisely and reproducibly create membrane structures of very similar curvature over nearly the same length of time? What specific cues activate curvature-sensing enzymes, such as turning on the membrane remodeling activity of dynamin2? Answering these questions will require multiple technical advances: 1) the development of novel reconstitution systems, in which vesicle curvature can be controlled across length scales with multi-component protein systems; 2) high-precision nanofabrication of substrates to induce curvature on *in vitro* and live cell membranes for kinetics measurements; and 3) incisive modeling of membranes with curvature present.

Mechanisms of curvature evolution in CME

One way to define endocytosis is as a process of curvature generation, from flat to spherical membrane. In clathrin-mediated endocytosis, the cell uses many of the mechanisms described above to achieve this complex curvature change, which happens within about 60 seconds, of a region of plasma membrane marked for endocytic uptake. The process requires dozens of proteins spread across a handful of conserved modules to produce an ~100-nm invagination at sites of clathrin-coated pits (CCPs) (McMahon and Boucrot, 2011). Vesiculation begins in the nucleation module with cargo molecules binding to adaptors such as AP2, followed by stabilization with early CCP-binding proteins such as FCHo1/2, EPS15, and the coat molecule clathrin stabilizing the endocytic site and establishing early curvature (Jackson et al., 2010; Henne et al., 2010). As the endocytic site matures, a feedback loop of curvature generation and stabilization occurs, with incorporation of more adaptors, cargoes, and curvature-generating proteins such as epsins, culminating in the production of a clathrin-coated vesicle and membrane scission catalyzed by the GTPase dynamin (Ehrlich et al., 2004; Ford et al., 2002; Grassart et al., 2014; Busch et al., 2015).

CCPs localize preferentially to sites of nanoscale curvature in cultured cells, suggesting that induced plasma membrane geometry play a regulatory role in CCP nucleation and dynamics (Zhao et al., 2017). Total internal reflection fluorescence (TIRF) microscopy is a standard method for studying CME in cultured mammalian cells because of its high signal-to-noise ratio for events occurring at the ventral membrane of a cell (Aguet et al., 2013). By monitoring the profile of fluorescently-tagged endocytic proteins over time, many mechanistic insights into CME activity can be gleaned, such as the temporal relationship between the endocytic modules and how select protein perturbations affect productive endocytosis. The Drubin lab has had many successes on this front (for instance, establishing the high success rate of CCPs) by using genome-edited cells, which stably express fluorescent fusion proteins under the control of endogenous loci, allowing for dynamic studies of CME in an unperturbed system. However, the shape changes occurring at a CCP are invisible to the light microscope because they are smaller than the diffraction limit of even the best optical system (~200 nm in X-Y and ~500 nm in Z). Thus, how the dynamic evolutionary shape change of endocytic membrane is achieved with a predictable order and

timing of events during CME is still an open question in cell biology. Experimentally, by inducing stable, nanoscale curvature on the plasma membrane, we can decouple curvature generation from the natural CME process.

Studying CCPs at sites of high curvature, especially in the context of disruptions to the endocytic machinery, promises to provide insights into how the cell achieves this complex 3-dimensional feat in a short period of time. In the following sections, I will describe a method of curvature induction in mammalian cells, demonstrate the effect of curvature on the localization and activity of normal endocytic pits, and reveal how induced curvature alters the activity of perturbed CCPs. Using induced curvature, I will show how the formation of a stable, U-shaped invagination shines light on the functions of the modules of CME, in particular demonstrating that induced curvature bypasses the function of clathrin and thus demonstrating that clathrin's essential role at CCPs is to stabilize nascent membrane curvature, acting as a Brownian ratchet.

Chapter 2
Introduction to electron-beam lithography, reactive-ion etching, and UV-nanoimprint lithography as a method of manufacturing substrates for microscopy

Introduction to Lithography

Lithography is one of the oldest fields of materials science, with roots dating back hundreds of years (Senefelder, 1911). The principle underpinning of all types of lithography, in its broadest implementation, is the use of materials with *differential solubilities* in water, oil, or another solvent (Thompson, 1983). By creating a shape on a solid substrate with semi-solid or curable materials, it is possible to create areas with high or low response to chemical etches because of the difference in solubility. This difference in etch rate allows for precise, controlled shapes to be drawn by structuring the reactions of chemicals: the control comes not from the etching chemical, but from the shape on the surface. In this sense, lithography is an inversion of the typical method of "writing" in which the ink is shaped into letters; in lithography, the substrate (analogous to paper) is shaped, and the ink is allowed to interact uniformly with the surface, but where it acts is controlled by the patterned substrate (Fig 2.1).

Lithography's application in biological sciences came soon after the development of cultured human cells, when researchers realized the potential of using high-precision lithographic methods to create templates that mimic features present in complex biological systems (Rovensky et al., 1971). The promise herein is vast: lithographic methods can bridge a key gap between *in vitro* and *in vivo* studies by combining the high-sensitivity techniques employed in biochemistry or cell biology studies with highly precise and reproducible, biologically-relevant structures (Kane et al., 1999). The earliest applications of lithography in cellular science include attempts to replicate the patterns of chemicals found within the human body—templating the localization of extracellular matrix, giving physical guides for cellular growth, or inducing stem cell development through modulating physical parameters of the environment (Chen et al., 1997; Hammerback et al., 1985; Engler et al., 2006).

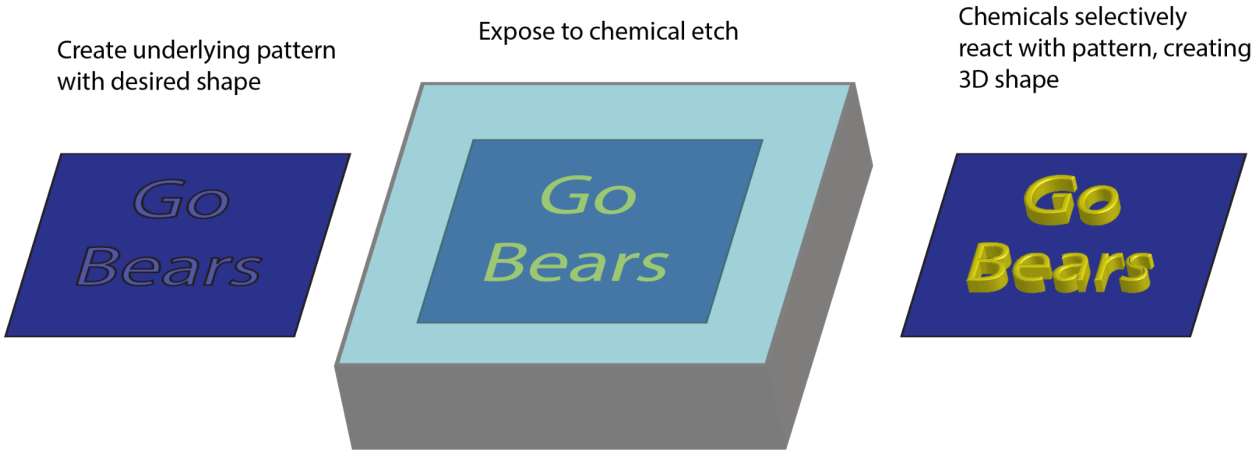

Figure 2.1: Lithography depends on creating a pattern on a substrate with a lighographic material, exposing the substrate to a chemical etch that reacts differently to sites on the substrate based on the presence or absence of the lithographic material, and developing the final structure.

Low-resolution techniques such as soft lithography have proved enormously productive in biological science (Whitesides et al., 2001). At its core, soft lithography is a method that involves shaping elastomeric materials into a mask of the desired shape, then stamping the mask to create a replica of the mask (Fig 2.2A). Because of the high speed of such micro-contact printing, soft lithography has been used widely across cell biology, biochemistry, and biotechnology: everything from co-culturing different cell types to high-throughput genomic sequencing is achieved through specialized soft lithography. Poly-dimethylsiloxane (PDMS) is a frequent choice for soft lithography in biological applications because of its low cost and ease of use. PDMS is illustrative of the paradigm of lithography in biological science: materials are 1) shaped by a mask to create an interesting structure, 2) chemically modified (often by UV exposure) to solidify them, then 3) applied to a biological problem where the shape, or the specific surface property of the material, is important to the biological context (Fig 2.2B).
The scale of the shapes created by lithographic methods is principally limited by the shape of the mask, and attempts to push the resolution of a mask to smaller and smaller sizes are limited by the cost, difficulty of the methods, and large amount of time required to create the correct mask. We sought to create substrates on the nanometer scale to induce highly localized cell membrane curvature. The following chapter explains how, in collaboration with the Molecular Foundry at LBL, we created a mold and applied it to a lithographic technique similar to soft lithography, termed UV-nanoimprint lithography (Bender et al., 2002).

The capacity to push lithographic design to produce smaller and smaller structures is a key problem in materials science research. It is of outsize importance to the manufacturing of processors for computers and cell phones, where the ability to pack transistors into small, closely-spaced integrated circuits leads to enormous advantages in terms of size, performance, manufacturing cost, and energy consumption (Wu et al., 2010). These benefits to technology have been the principal driving force behind theoretical and experimental advances in nanofabrication; the knock-on benefits to other fields such as photovoltaics, optics, biochemistry, and cell biology are relatively recent additions to this field (Tseng, 2008).

Nanofabrication: theory and methods
Nanofabrication could be reasonably conceived of as any of the class of processes capable of making structures below a half of a micron, or 500 nanometers, while most soft lithographic techniques build structures on the order of tens of microns, much more similar to the size of the average human cell. Nanofabrication was first achieved by—and still largely consists of—planar processing of the substrate, a general term for methods in which a 2-dimensional structure is projected onto a substrate, and the 3-dimensional shape of the final structure comes from later processing steps (Fig 2.3A) (Wolf, 1989). There are many types and methods of planar processing, but they can broadly be thought of as two categories: “top-down” or “bottom-up” (Fig 2.3B) (Biswas et al., 2012).

Bottom-up lithography is the process of building structures through controlled addition of select materials to form the desired shape. The methods employed include solid-state scanning probe lithography, in which a microscopic “fountain pen” deposits nanometer-scale liquids or gels to

Figure 2.2: Soft lithography as a stamp-and-expose system. A) Structured molds, such as from the material PDMS, can be used to stamp a material such as a glass coverslip in desired locations with the desired material. B) The mold is typically made through photolithography, in which a photomask is used to shape a liquid material that is then cured through heat or UV exposure to solidify. The scale of features producible in (A) is limited by the resolution of the photomask/curable material created in (B).

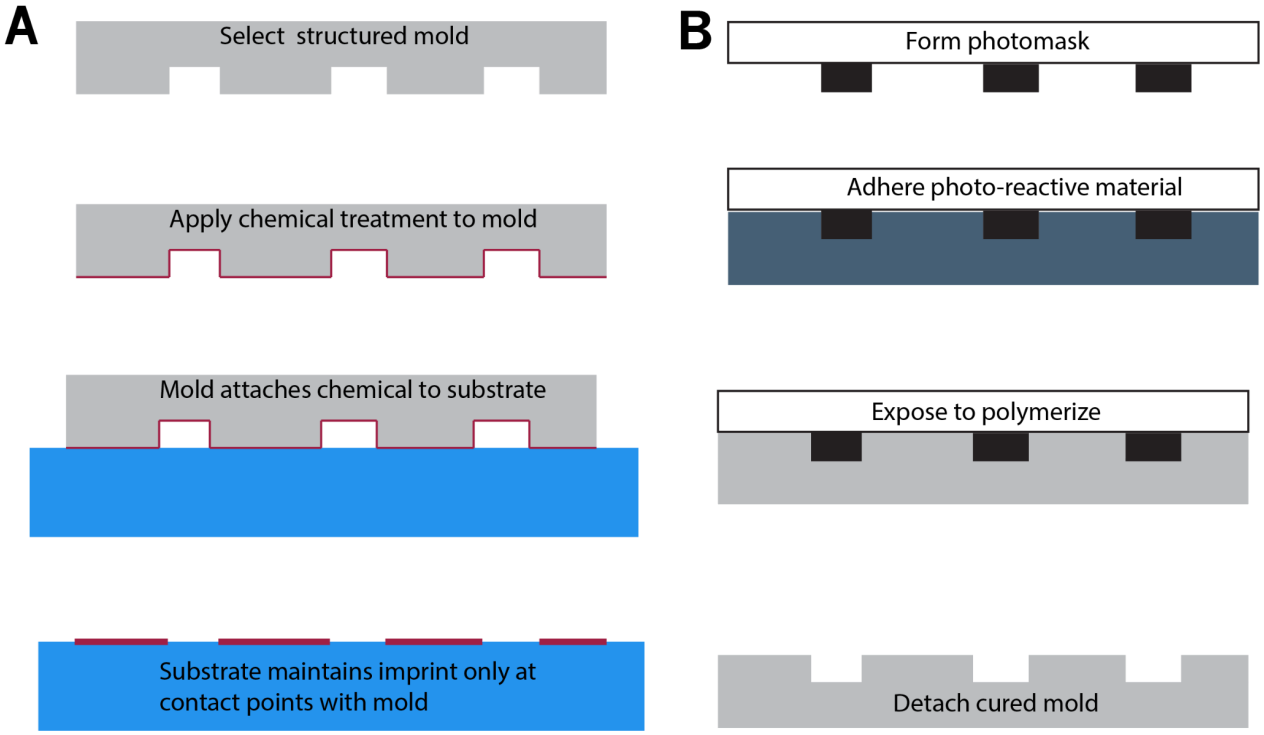

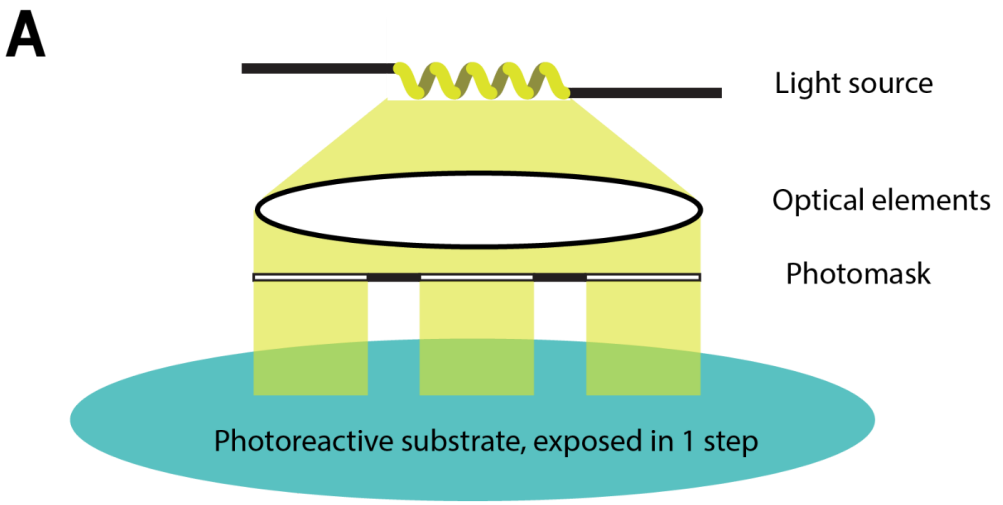

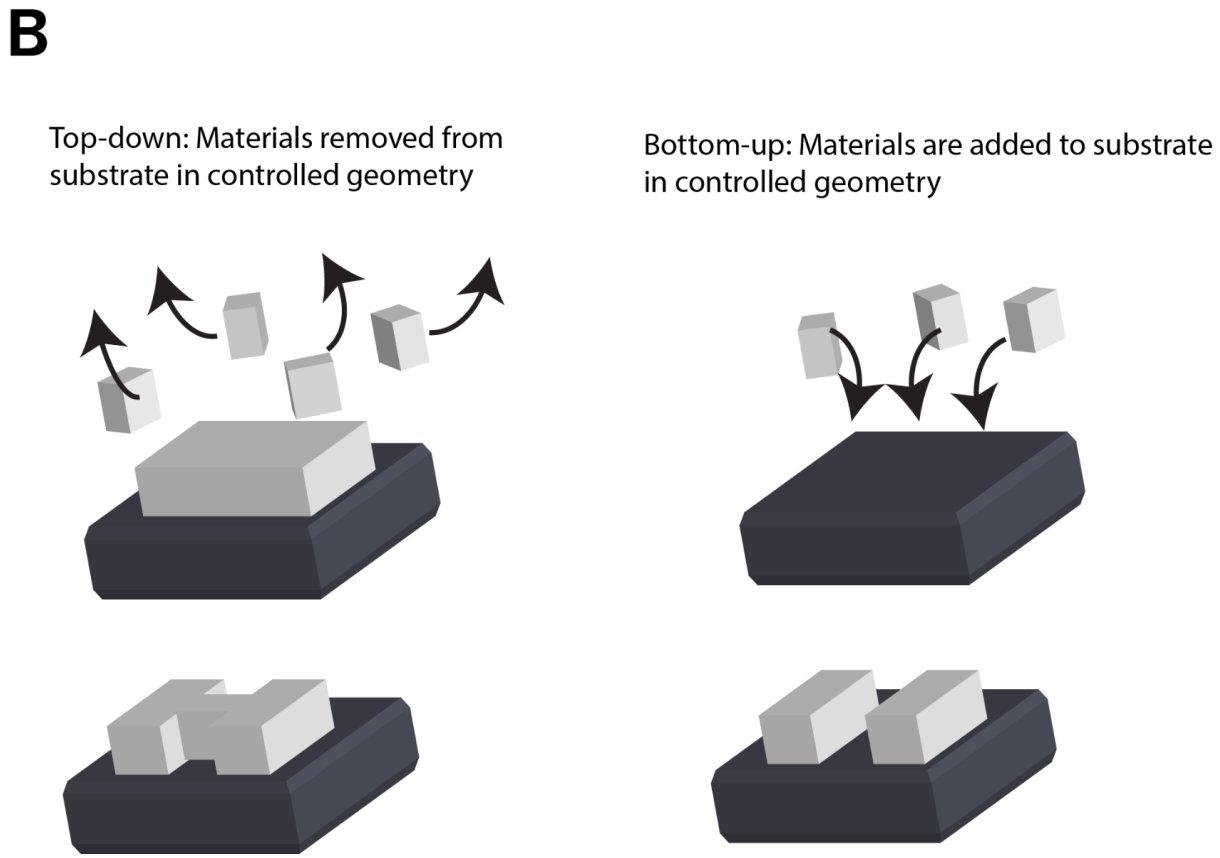

Figure 2.3: Planar processing and top-down/bottom-up mold formation in lithography. A) The most common form of photolithography to produce masks or substrates is planar processing, in which a 2D structure is projected onto a photoreactive substrate and a 3D structure is created from fine-tuned etching steps at later stages. B) Top-down and bottom-up etching processes, in which the photoreactive/exposed substrate materials from step (A) are either chewed away (top-down) or deposited (bottom-up) to produce the final 3D structure.

create shapes; self-assembled monolayer techniques, in which chemicals such as silanes are employed that spontaneously form layers of single-molecule thickness, in which all molecules have the same orientation; and atomic layer deposition, in which gas-phase atoms adhere to the surface of the substrate, one layer at a time, and the sequential addition of distinct chemical species controls the size and shape of the substrate (Cavallini et al., 2004).

Top-down lithography, by far a more common and high-throughput means of nanolithography, takes the opposite theoretical approach to that of bottom-up lithography (Biswas et al., 2012). Instead of sequential building of shapes by adding chemicals, in top-down lithography, layers or areas of substrate molecules are removed with high precision, and so the desired shape consists of what was left behind. The approach most typically employed in top-down lithography, widely adopted by processor manufacturing companies around the world, is photolithography: a mask of desired structure is placed above the substrate material, which must be reactive to the wavelength of light employed, and then exposure to light (typically in the UV range) causes a chemical change only in areas where the mask is light-permissive (Cui, 2008). This procedure creates differences between light and dark sections of the substrate beneath light and dark areas of the photomask. Further processing through chemical etches causes shapes to form according to the previous exposure to ultraviolet light. By repeatedly exposing the photoresist after precisely positioning the mask, shapes of incredibly high precision (down to 5 nanometers using the currently available commercial microprocessors) can be produced reliably in quite a high-throughput manner. In fact, as of 2016, the semiconductor industry produces *56 billion transistors per person per year* almost entirely through photolithography (Courtland, 2016).

Photolithography has a key limitation related to the production of a mask: how can photomasks with nanometric features be produced when the diffraction limit of photolithography is on the order of 200 nanometers? And how can one create shapes with unique, high-resolution features below the diffraction limit with only a limited number of permutations of a photomask's imprint pattern? The key advance in tackling these challenges in photolithography came by employing electrons, whose wavelength is far below that of even the highest-energy UV photon, and so the size of feature producible is far finer than is possible using photolithographic methods. The resolution limit of electron-based lithography methods is limited by factors other than electron diffraction and is on the order of single nanometers, which is significantly better than purely photolithographic methods for mask production, whose best resolution is closer to 500 nanometers (Cui 2008).

Electron-Beam Lithography

Electron-beam lithography (EBL) is the principal method for creating nanometer-scale shapes *de novo* (Fig 2.4). The method depends on a modified form of the scanning electron microscope (SEM), a tool for creating a tightly focused beam of electrons used to raster-scan over a surface (Fig 2.4A). A huge limitation of SEM—and the foundation of EBL—is the fact that electrons, unlike photons, interact strongly and usually irreversibly with the surface over which they are scanned (Broers et al., 1996). Thus, SEM often requires a metal surface, over which the electron beam can be dispersed, so as to not build up damaging charges. However, a key insight in materials science in the 1970s was that this buildup of charges can create useful, highly localized chemical modifications, in a largely predictable manner (Fig 2.4B).

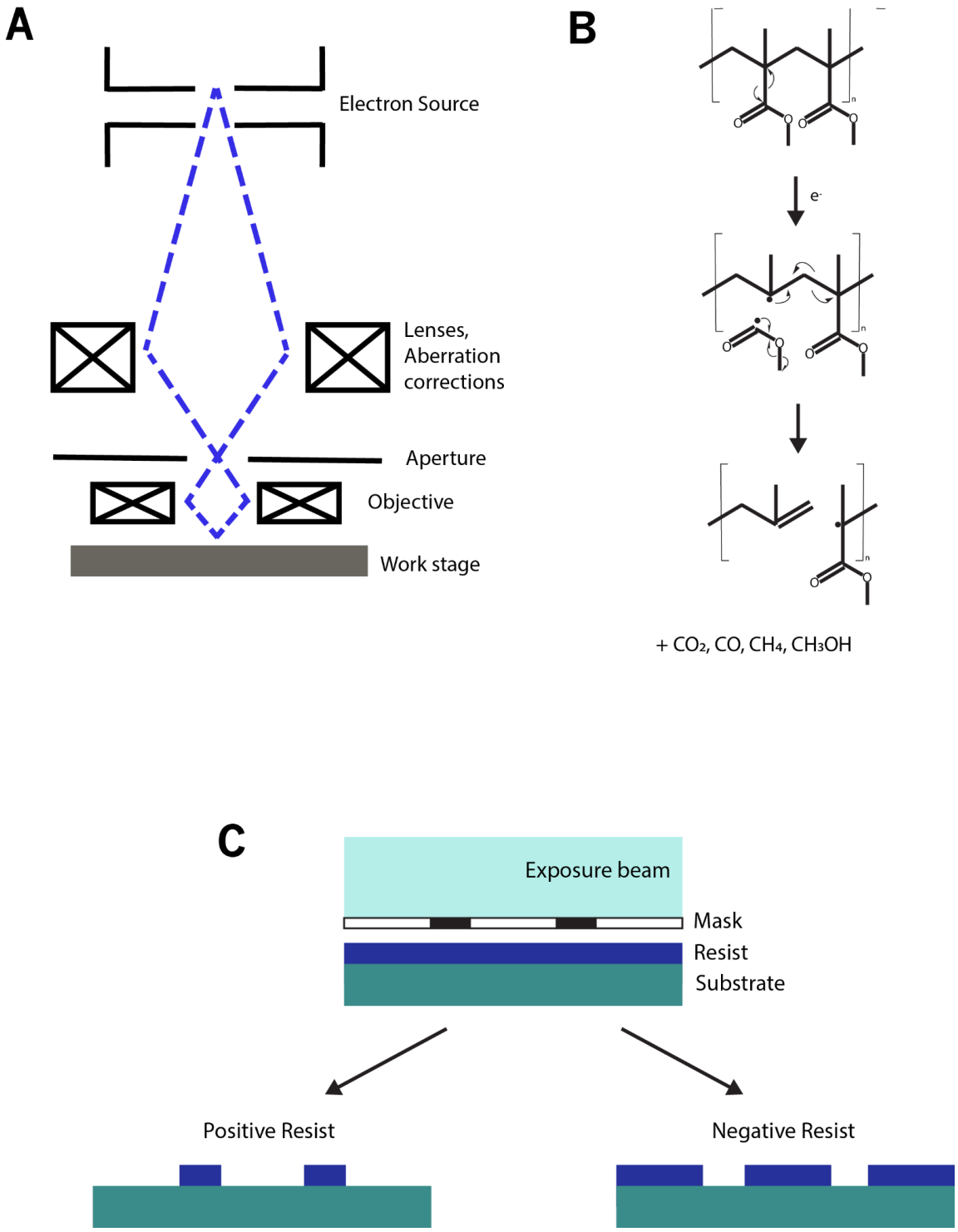

Figure 2.4 Electron-beam lithography to create smaller features on masks/molds. A) Schematic of the electron-beam lithograph, a modified form of the scanning electron microscope. B) Example chemical reaction of the resist polymethyl-methacrylate (PMMA) reacting to exposure to an electron beam, breaking an acrylate bond and shortening the polymer. C) Resists are classified as either positive or negative based on how they are etched away after electron-beam exposure.

To fully leverage these localized chemical reactions, materials scientists produced a number of materials termed *resists*. The resist is the material that interacts locally with the electron beam, for instance by breaking an acrylate bond in the material poly-methyl-methacrylate (PMMA) (Hiraoka, 1977). When an electron-induced chemical reaction occurs inside the resist, it changes its properties such as its acid-sensitivity or solubility in water. Resists are classified as either "positive" or "negative" (Fig 2.4C). A positive resist is one where the locations exposed to the electron beam are the locations etched. Thus, the shape written is the same as the ultimate shape created on the substrate. A negative resist, on the other hand, reacts to the etch only where the electron beam has *not* scanned, and so the final structure of the substrate is the inverse of the shape written with the electron beam. Thus, positive resists are generally much faster to make than negative, as the desired structures are usually small relative to the size of wafer.

The electron beam does not actually create the final shape of the substrate; it simply alters the chemical properties of the resist material atop the substrate wafer. The final shape is created on the wafer beneath the resist (Lee, 1969). By exposing the substrate/resist combination to chemical etching, the underlying substrate is etched away by a chemical reaction such as that from hydrofluoric acid (Fig 2.5). Importantly, the chemical reaction proceeds only in the select sections where the resist has (for positive resists) or has not (for negative resists) been exposed to the scanning electron beam. Thus, the shape written with the electron beam on the resist is carved with chemicals on the substrate. The depth of the shape is controlled by the extent of the chemical reaction from the etching reagents; longer exposure, or exposure to more etching agent, carves away more of the wafer and makes deeper shapes.

Chemical etching cannot be well controlled with wet chemicals; the chemical reaction proceeds isotropically from the sites of exposure (Fig 2.5A). To better control the shapes created by the etching step, materials scientists developed dry etching methods to induce anisotropic chemical reactions. In a dry etch, the etching chemical is in the gas phase rather than the liquid phase; the etch often comes from ions present in the gas phase, which is termed Reactive Ion Etching (RIE, Fig 2.5B) (Khan and Adesida, 1999). Because the gas-phase etching agents do not surround the wafer at sufficiently high concentration to carve away the underlying substrate, the chemical reaction is halted until the user induces the directionality of etching. This is carried out through coupling the gas-phase reactive ion etch with the directional control of an electric field. In the presence of a sufficiently strong electric field, gas-phase ions, which carry an electric charge, are pulled towards one pole, depending on the charge of the ion—positive ions to the negative electrode, and vice versa. Thus, by placing the substrate wafer at the positive electrode, negatively charged particles such as ionized sulfur hexafluoride are pulled to the positive electrode, where they react with the sections of wafer exposed by the electron beam lithograph.

Overview of substrate nanofabrication process

Nanofabrication is necessarily a multi-step process (Fig 2.6). The first step of planar processing is the selection of a suitable substrate. Very commonly, silicon wafers are the substrate of choice because of their relatively low cost and desirable material properties for later steps such as microprocessor fabrication. Highly pure crystalline silicon, sometimes doped with small amounts of other materials to change the charge-carrying properties (Jeon and Grischkoswky, 1991), is crystallized into a boule with purity of 99.9999999% or higher. This boule is cut into individual wafers, commonly 0.725mm thick; for our purposes, the wafer selected was 200mm across.

A

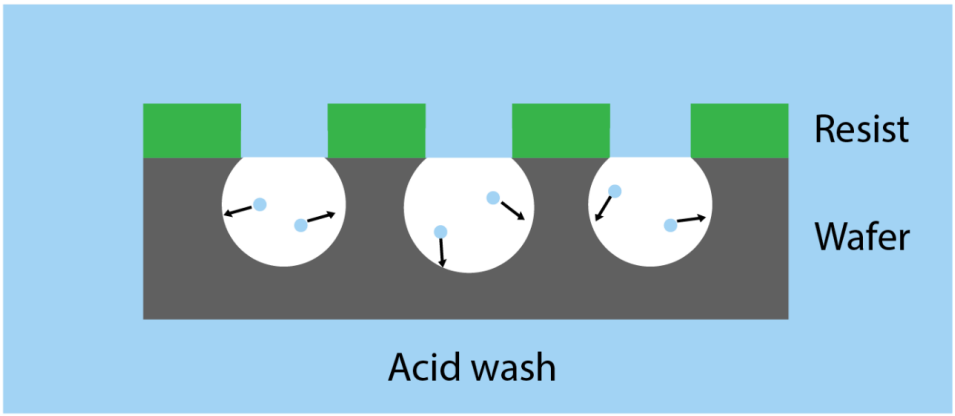

Chemical exposure creates isotropic etch

B

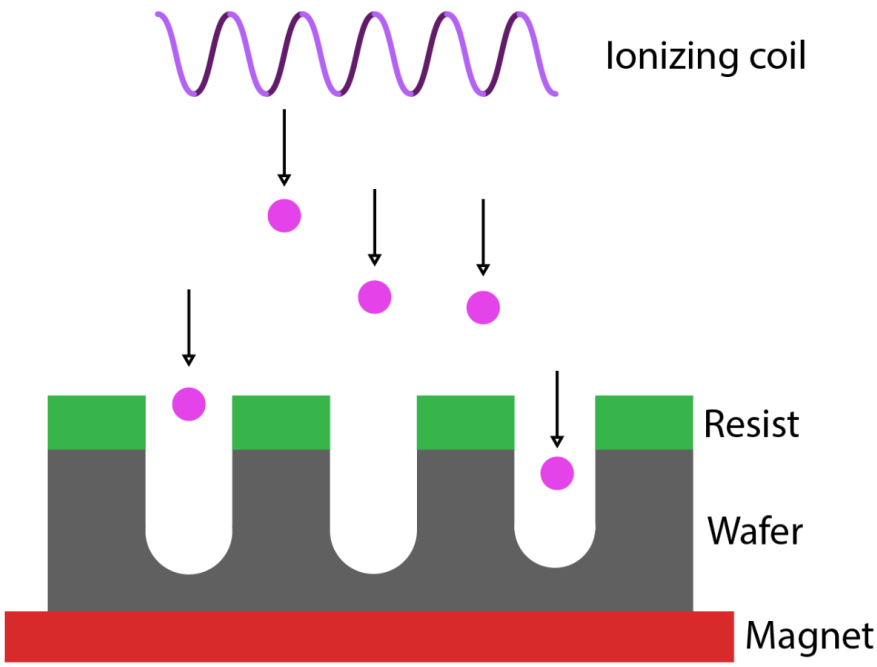

Reactive ion exposure creates anisotropic etch

Figure 2.5 Chemical etching vs reactive ion etching. A) Exposure of wafer/resist combo to a wet etch such as an acid wash creates isotropic shapes with poor 3D control, the only control comes from the time of exposure. B) Reactive ion etching allows for controlled 3D shape by only allowing the reaction to proceed along one direction within the wafer, thus creating anisotropic etches.

Once the silicon wafer was selected and prepared for nanofabrication (see Methods), the resist was selected for suitable mold creation. There are several considerations to weigh when selecting the resist best suited to the desired nanofabrication. Most importantly for our purposes, we had to consider 1) the extent of electron scattering, 2) the electron proximity effect, 3) the resolution available for the resist, 4) and time required for lithography. Electron scattering in the resist causes inconsistent widening of the features because the electrons scatter elastically upon entering the resist material, meaning imprecision on the nanometer scale--a problem that is exacerbated by deeper features, which were desired for this project. The electron proximity effect, similar to light's proximity effect reducing resolution when features are close together, necessitates writing features that are separated by sufficient space, usually ~3-5x the size of the feature. The resolution of a resist and the time required for feature-writing are inversely proportional to each other: high-resolution features require more electron writing time, which is cost-prohibitive at the Molecular Foundry. In consultation with the staff scientists of the LBL Molecular Foundry, we ruled out polymethyl methacrylate (PMMA) because of high electron scattering for deep features. We ruled out hydrogen silsesquioxane (HSQ) because of high time requirements for lithography, despite its otherwise promising properties. Based on the criteria of high aspect ratio desired for features, we selected the material ZEP520A, with the important caveats to feature design that the features should be spaced by at least a micron to avoid the electron proximity effect. Thus, we designed millimeter-long nanoridges, with thicknesses of 75, 120, 200, 300, 500, and 1000 nanometers, spaced at a pitch of 2 microns to avoid proximity issues. We sought to create rounded tops to the nanoridges in the etching stage, while maintaining straight edges, to induce a fibrilar shape on the ventral cell surface.

With substrate and resist chosen and adhered (see Methods), we proceeded to the electron-beam lithography step (Fig 2.6A). We created 16 test molds to test 4 different EBL doses with 4 different chemical etch rates. EBL doses are measured in microCuries per square centimeter (uC/cm^2), as a measure of radiation density, and we chose to test four values in the range of 100-250 uC/cm^2.

After EBL, we finished the shape on the silicon wafer using reactive ion etching to finalize the shapes. To create straight sides with a high-aspect-ratio and a round invagination at the bottom of the wafer, we turned to inductively coupled plasma RIE (ICP-RIE), which allows for very precise spatial control of etching (Fig 2.6A). By maintaining near-cryogenic temperatures for etching, the trajectory of ions is tightly controlled, allowing for increased anisotropic chemical etching. The ions derive from a plasma source located at the top of the ICP-RIE chamber; the ions are then pulled to the wafer by creating an electric field towards the bottom of the chamber, where the stage holds the silicon wafer/resist combination. We employed sulfur hexafluoride because of its high reaction rate with silicon, which helped create high aspect-ratio structures. After ICP-RIE, we characterized the nanofabricated structures under a scanning electron microscope (SEM) and selected the mold with most consistently straight sides and deepest invaginations.

UV-Nanoimprint Lithography for biological experiments

With the mold created and characterized through SEM, we next had to develop and optimize UV-NIL methods for repeated substrate manufacturing. A strong hydrophobic coating of fluorosilane was deposited on the wafer (see Methods), ensuring that a polymer would take on

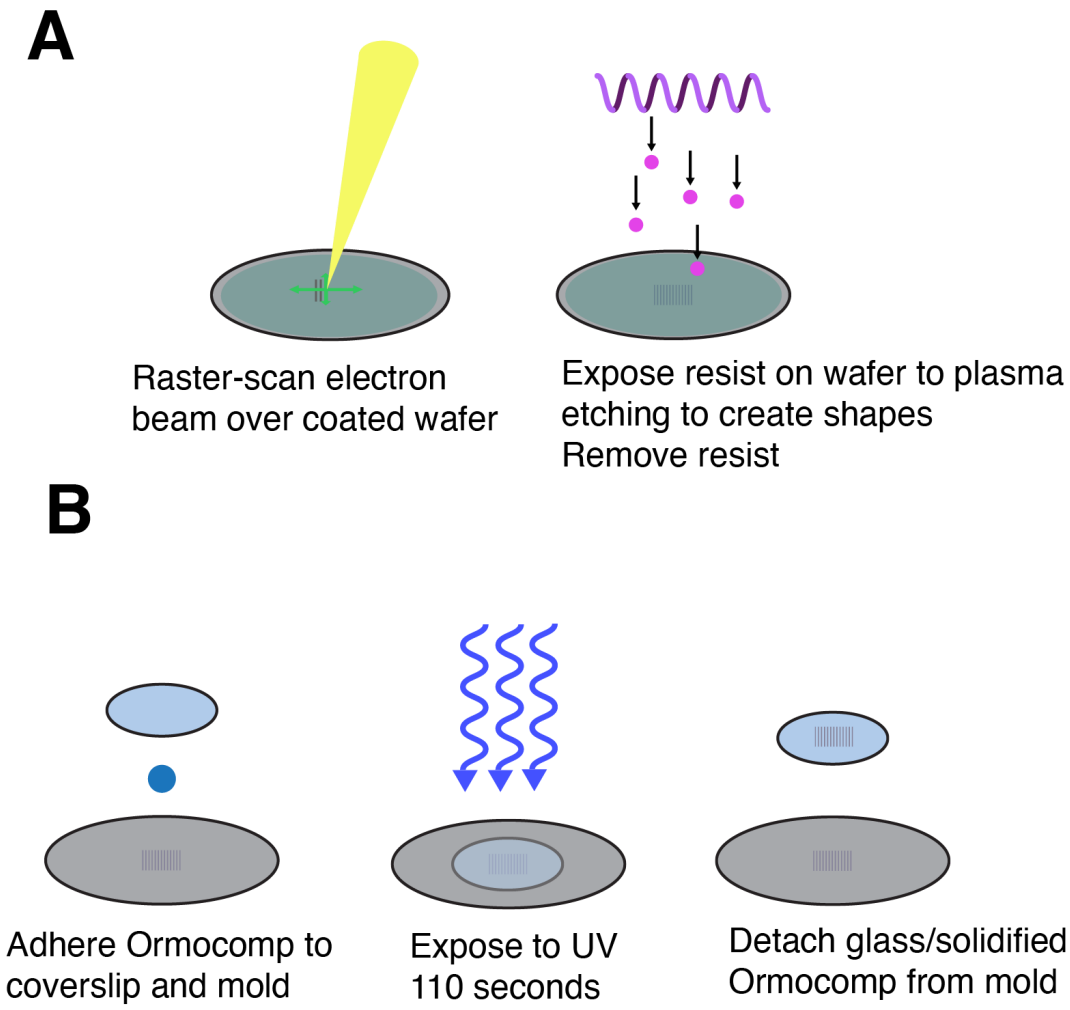

Figure 2.6: Step-by-step process of Ormocomp substrate manufacturing through UV-Nanoimprint lithography. A) Electron-beam lithography followed by sulfur hexafluoride inductively-coupled plasma reactive ion etching creates the nanofabricated ridges on the silicon wafer, which then serves as a mold. B) Process of Ormocomp adhesion followed by UV exposure to polymerize on the silicon substrate, creating a microscope coverslip that bears the nanofabricated shapes.

the nanoscale shape of the nanoridge mold while preferentially binding to a coated glass surface. We selected the organic-inorganic hybrid material Ormocomp for UV-NIL because of its near exact refractive index match to that of borosilicate glass, allowing for TIRF microscopy (Fig 2.7A). Ormocomp polymerizes through polyacrylate chemistry to form a solid, glass-like substrate upon intense UV exposure (Fig 2.7B). Through trial and error, we developed a method for reproducible substrate manufacturing (see Methods) that required only ~15 minutes per substrate (Fig 2.6C-E). Briefly, we adhered Ormocomp to the substrate and coverslip, polymerized Ormocomp through UV-crosslinking, and detached solid Ormocomp from the mold.

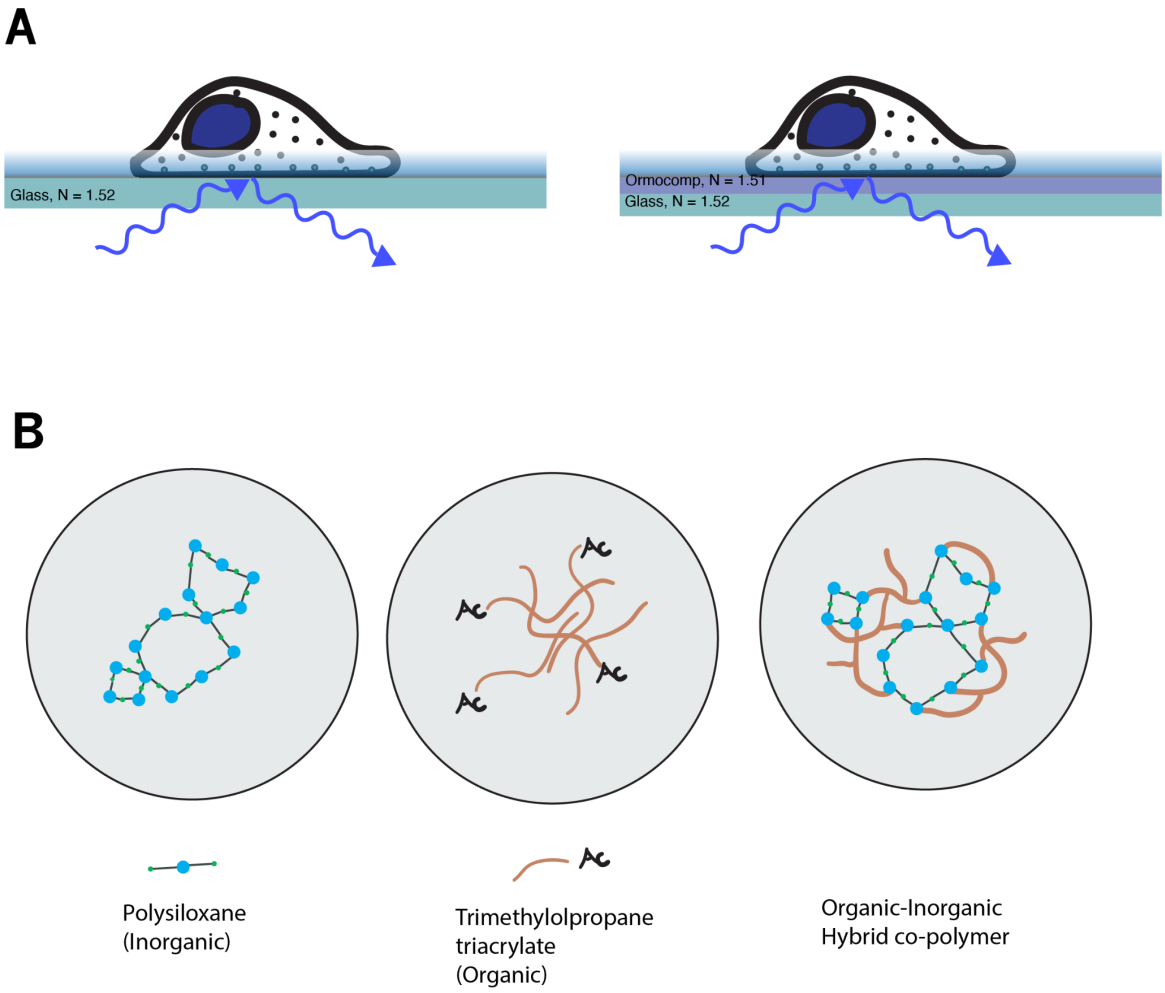

Figure 2.7: Ormocomp has good optical properties for TIRF. A) Schematic of the incident laser on the TIRF microscope reflecting off of the glass coverslip (left) or Ormocomp-coated coverslip (right), creating an evanescent field that selectively illuminates the bottom of the cell. B) The refractive index matching of Ormocomp comes from the polysiloxane material; the UV-induced polymerization is a consequence of the acrylate molecule TMPTA present in the material, creating an organic-inorganic hybrid material.

We then characterized the Ormocomp substrates through scanning electron microscopy (SEM) and thin-section TEM (Fig 2.8A). SEM revealed long, thin ridges of the desired thicknesses, with rounded tops visible at higher-angle SEM. TEM images revealed that the profile of the nanoridges was indeed a curved top, with a depth of approximately 300 nanometers for the 120-1000nm ridges and 200 nanometers for the 75nm ridge (Fig 2.8B). It was previously established that endocytic sites preferentially localize to sites of high positive curvature on quartz substrates (Zhao te al., 2017). When we imaged genome-edited MDA-MB-231 cells expressing AP2-TagRFP, we found a clear preference of endocytic sites for the high-curvature nanoridges, evidence that the same effect of CME protein localization was induced by UV-NIL-based Ormocomp nanoridges (Fig 2.8C).

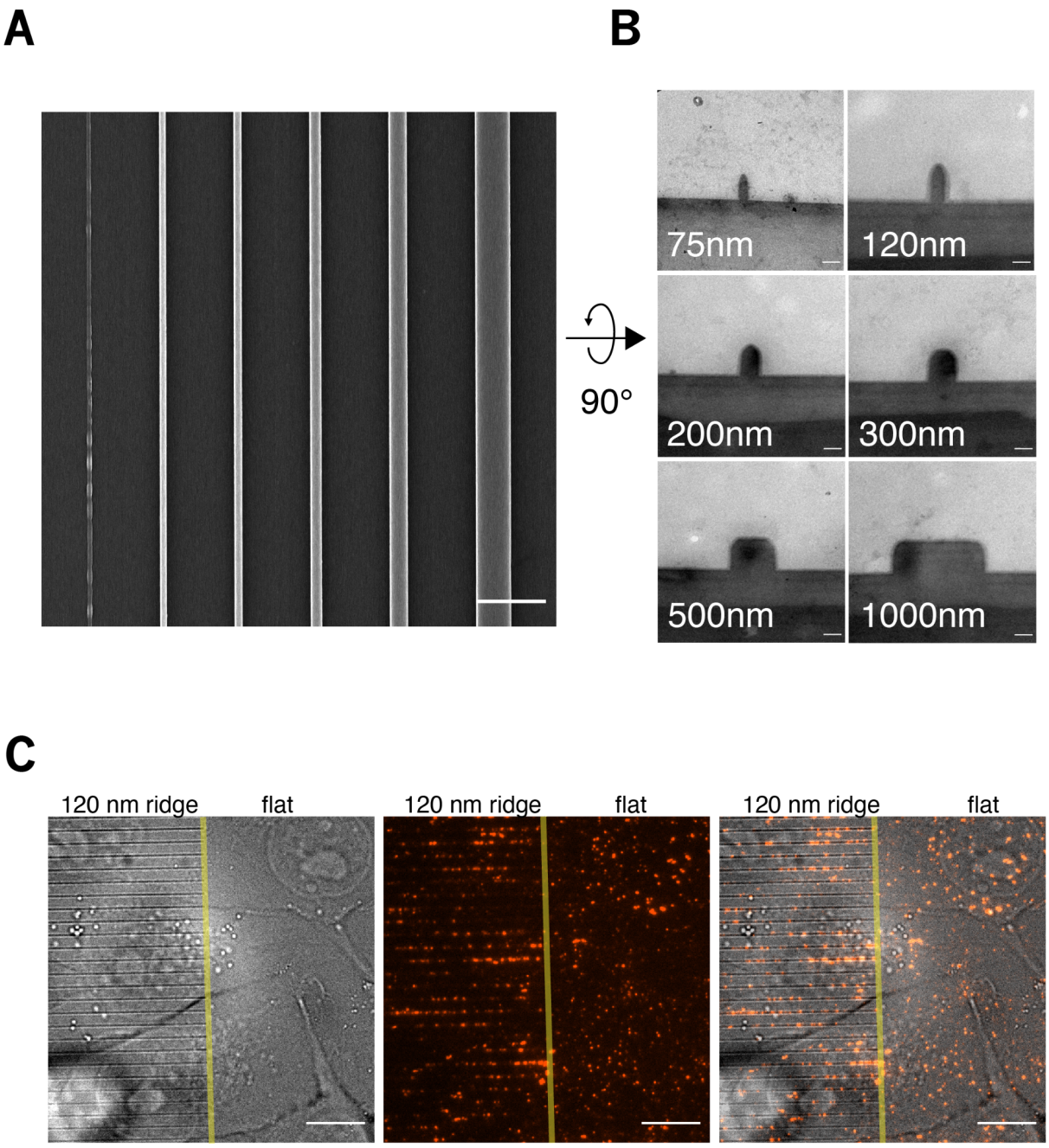

Figure 2.8 Ormocomp nanoridges and the response of cells to them. A) En-face SEM of platinum-coated nanoridges showing the millimeters-long, nanometer-scale ridges formed from the mold. Scale bar 2 microns. B) Thin-section TEM of the nanoridges showing their thicknesses in higher magnification and the pointed tip that induces curvature on the bottom of a cell plated on the Ormocomp substrates. Scale bar 100 nanometers. C) Sample image of cells on the edge of the 120-nm ridge section of an Ormocomp substrate, with AP2-RFP genome-edited and shown in the red channel. On the nanoridges, there is a striking rearrangement of the AP2 puncta, demonstrating that curvature reorganizes the endocytic machinery. Scale bar 10 microns.

Methods
Silicon molds were prepared for EBL by UV-Ozone cleaning for 2 minutes and baking at 150°C for 30 minutes, followed by coating in hexamethyldisilazane (HMDS) and curing at 150°C for 10 minutes. ZEP520A was prepared by dissolution in anisole, then adhered to HMDS-treated silicon substrate by spin coating at 5000rpm followed by baking at 150°C for 2 minutes. This wafer was then processed by EBL in Vistec VB300 electron beam lithograph with 100, 150, 200, and 250 uC/cm^2 with 100kV electron beam.

ICP-RIE was carried out in an Oxford Plasmalab RIE in liquid nitrogen-cooled chambers (-150°C) using 98% oxygen (O2) and 2% sulfur hexafluoride (SF6) at 5mTorr and 10mTorr for 60 or 120 seconds. ZEP520A was then removed from the silicon molds using acetone/IPA cold washes (4°C). SEM characterization of molds was carried out on Zeiss Gemini Supra 55 VP-SEM.

After nanoridges were etched and characterized, trichloroperfluoroctylsilane (fluorosilane) was deposited according to the following protocol: wafers were cleaned in UV-Ozone, then baked to dry at 180°C for 10 minutes. Fluorosilane was deposited in a gas phase at 150°C for 20 minutes under vacuum. This was repeated approximately every six months, or after piranha etching to clean the mold.

Piranha etching of the mold was performed approximately annually, as needed to clean the silicon wafer of residues left from UV-NIL. 20mL hydrogen peroxide was mixed with 80mL sulfuric acid and the wafer placed into the mixture for 10 minutes, followed by 7x washes with deionized water. The wafer was then left in deionized water until fluorosilane coating.
To produce Ormocomp substrates, corning #1 22mm circular glass coverslips were cleaned with isopropyl alcohol and dried for 5 minutes at 180°C, followed by spin-coating for 45 seconds at 2000rpm in 50 uL of HMDS, followed by another 5-minute incubation in the 180°C oven. 12.5 uL of Ormocomp was placed on the silicon mold atop the nanoridge structures. The HMDS-coated coverslip was placed onto the Ormocomp, and allowed to adhere for ~5 minutes. Once the Ormocomp had adhered to the substrate and coverslip, it was exposed to 14 mW UV light for 110 seconds, then detached from the mold and stored at RT for up to 6 weeks prior to use in biological experiments.

SEM of Ormocomp nanoridges was conducted on a Hitachi S-5000 SEM after sputter-coating in titanium to a thickness of 1-2 nm. TEM of nanoridges was conducted on a Tecnai 12 120kV TEM (FEI) and data recorded on UltraScan 1000 with Digital Micrograph 3 software (Gatan Inc.). Thin sections were cut from resin-embedded nanoridges on Ultracut E (Leica). Substrates were sterilized by exposure to UV irradiation for 12 minutes prior to use in cell culture.

Chapter 3

Endocytic sites localize to nanoridge substrates as a function of curvature, altering endocytic kinetics but not other parameters

The cellular response to induced curvature

We hypothesized that nanoscale curvature, on the same size scale of an endocytic pit, would stabilize the U-shaped high-energy intermediate of CME (Fig 3.1). Substrate micropatterning has been used for decades to study the effects of 3-dimensional context on cellular behavior; however, a key component of the utility of patterned substrates is the extent to which the cells respond to the substrate shape, or whether the cell's natural mechanics dominate the induced substrate. For instance, it has been demonstrated that cells have a threshold for ECM patterning of approximately 15% of substrate coverage; below this threshold, mouse B16 cells demonstrated adhesion and migration defects (Lenhert et al., 2004). Therefore, demonstrating the robustness of response to patterning is key in lithography studies.

Once Ormocomp nanofabrication had been optimized, it was first essential to determine the extent of the cell's physical response to substrate shape. Cultured human cells grow with a differential need for a substrate; for instance, suspension cells such as unstimulated T-lymphocytes do not respond strongly to substrate shape because they maintain a spherical shape during growth and division (Negulescu et al., 1996). We therefore undertook a screen of a few cell types commonly employed in the Drubin lab to determine which would best form curvature in response to nanopatterned Ormocomp features, and to test how robust and reproducible the response would be.

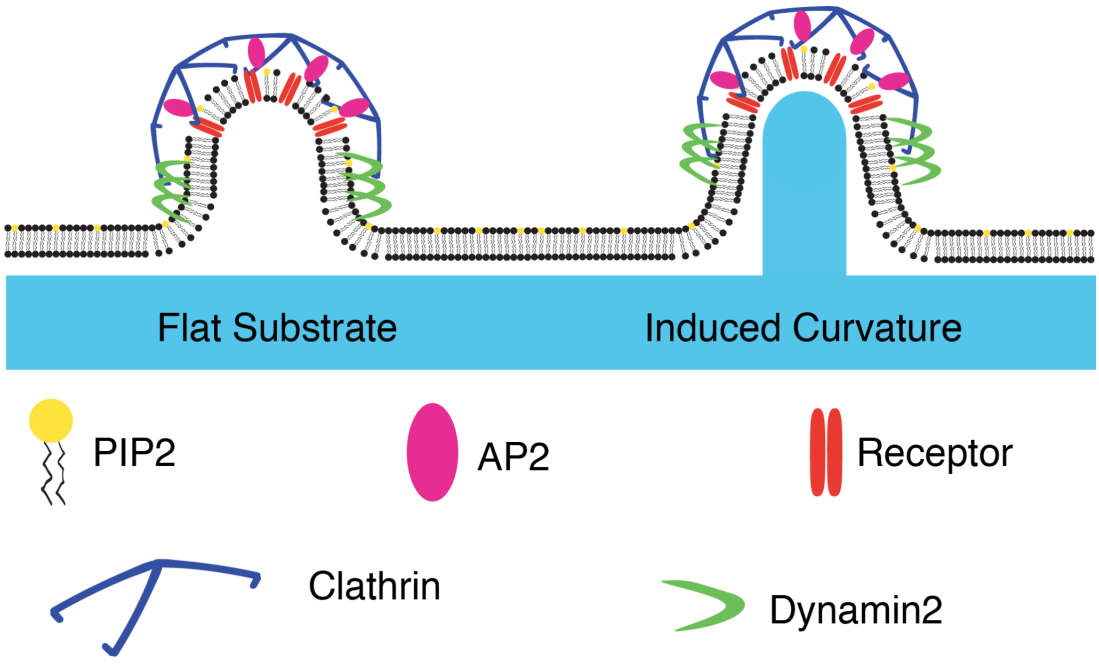

Figure 3.1: Induced curvature on the order of 100nm, the size of a CME site, stabilizes the endocytic machinery and assists in endocytic site formation.

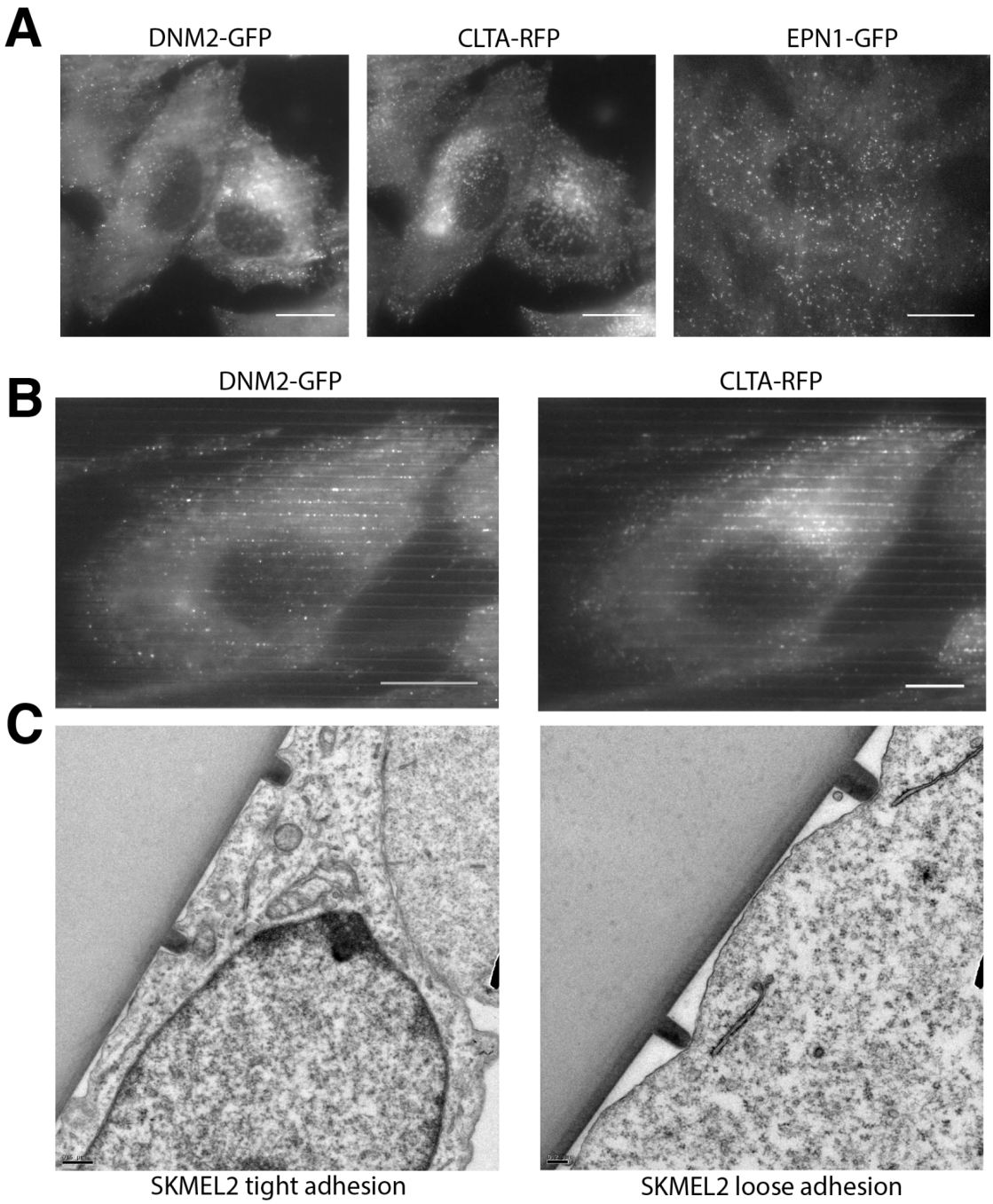

Figure 3.2 SKMEL2 cellular response to induced curvature. A) Genome-edited SKMEL2 cells expressing DNM2-GFP, CLTA-RFP, and EPN1-GFP on flat portions of the Ormocomp substrate, showing the cellular response is similar to that of microscopy glass. Scale bar 10 microns B) Genome-edited SKMEL2 cells on 75nm nanoridges, demonstrating a robust response of endocytic proteins to induced curvature. C) Thin-section TEM of SKMEL2 cells demonstrates the inconsistent response of the cell membrane to the nanoridge substrates.

We screened three cell types: induced pluripotent stem cells (iPSCs), transformed skin melanoma cells (SKMEL2), and transformed breast cancer-derived cells (MDA-MB-231, or MDA). The requirement that iPSC grow on a layer of matrigel presented an immediate roadblock to their use on nanoridge substrates (Kleinman et al., 1986). Attempts to create thin layers of matrigel on Ormocomp failed, and so the iPSC colonies could not adhere to the substrate and died.

SKMEL2 and MDA cells have no requirement for exogenous ECM to grow; they readily grow, spread, and demonstrate elongated morphology on Ormocomp in response to substrate curvature (Fig 3.2A). TIRF imaging of genome-edited SKMEL2 cells demonstrated a striking localization of endocytic proteins CLTA-RFP and DNM2-GFP to sites of higher curvature, evidence that these cells responded to the induced curvature by relocalizing the endocytic machinery (Fig 3.2B). TEM imaging of SKMEL2 cells revealed inconsistent adhesion to the nanoridges, indicating different radii of curvature in response to the same nanoridge size (Fig 3.2C). This inconsistency presented an experimental problem: if the membrane radius was different across two nanoridges, we could not be sure about the response to the nanoridge when imaging under a light microscope, where these differences are below the diffraction limit and so invisible to us.

MDA cells, however, also demonstrated a striking relocalization of endocytic sites to nanoridges, and TEM imaging revealed more consistent membrane diameter atop the nanoridges (Fig 3.3A, Fig 3.3B). In fact, the shape of membrane induced by the nanoridge was strikingly similar to the shape of membrane induced by collagen fibers on MDA cells, evidence that the shape of nanoridge chosen is relevant to normal biological activity (Elkhatib et al., 2017). The reproducible endocytic reorganization from cell types derived from the epithelium was evidence that endocytic response to curvature is a common feature of CME, and not simply an effect of one cell type. Based on their ease of use in cell culture, well-characterized endocytic dynamics, and the abundance of genome-edited cell lines available in our laboratory, we focused on MDA cells for the majority of induced curvature studies. This allowed us to screen the localization and dynamic shape of many different markers of endocytosis, with easy perturbation and reproduction of experimental conditions.

To test the regularity of substrate-induced membrane diameter atop nanoridges, we performed correlative light-electron microscopy (CLEM) to gain replicated measurements of multiple cells on substrates. We first had to detach Mattek CLEM dishes, which bear an etched grid allowing for selection of nanoridges with cells atop them. We then manufactured Ormocomp substrates on the CLEM etched dishes with a standard protocol, except for minor modifications (see Methods).

With CLEM-appropriate substrates made, we plated cells on the Ormocomp/CLEM dishes and prepared them for TEM (see Methods). We selected locations on the substrates with isolated cells atop the ridges of various sizes, embedded the cells, and thin-sectioned the selected areas for TEM (Fig 3.4A). Collection of at least 5 ridges from at least 3 cells per size allowed us to measure the average induced diameter atop nanoridges, which we measured to be 143.9 nanometers atop the 75-nm ridge, with a gradual increase up to approximately 650 nanometers atop the 500-nm ridge (Fig 3.4B). The 1000-nm ridge induced curvature only on the edges of the ridge, with an essentially flat top (Fig 3.4C). The diameter of this semicircular invagination was approximately 210 nanometers, similar to the size induced by the 120-nm nanoridge (Fig 3.4D). This consistent membrane curvature was key to ensuring reproducible experimental conditions for light microscopy.

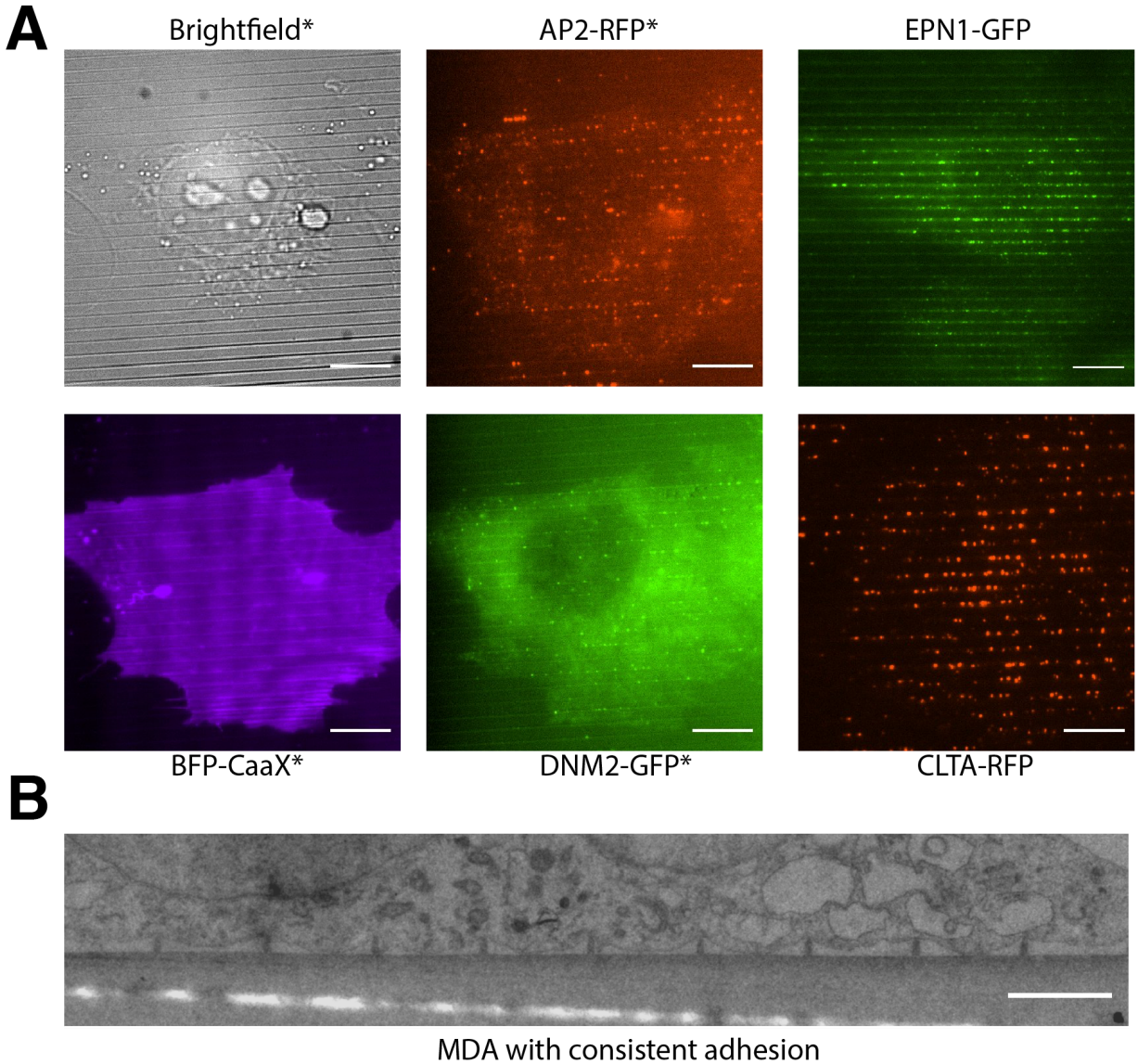

Figure 3.3 MDA-MB-231 cells on Ormocomp nanoridges. A) MDA cells on the 120nm nanoridge, with Brightfield, BFP-Caax marking the cell membrane, and AP2-RFP/DNM2-GFP genome-edited cell showing that while the entire cell membrane is illuminated, the endocytic proteins preferentially localize to the nanoridges. All images with * are the same cell. EPN1-GFP and CLTA-RFP from different cells also demonstrate robust response to curvature. Scale bar 10 microns. B)
Low-magnification thin-section TEM of MDA cell reveals more consistent adhesion of the cell membrane than SKMEL2 cells. Scale bar 2 microns.

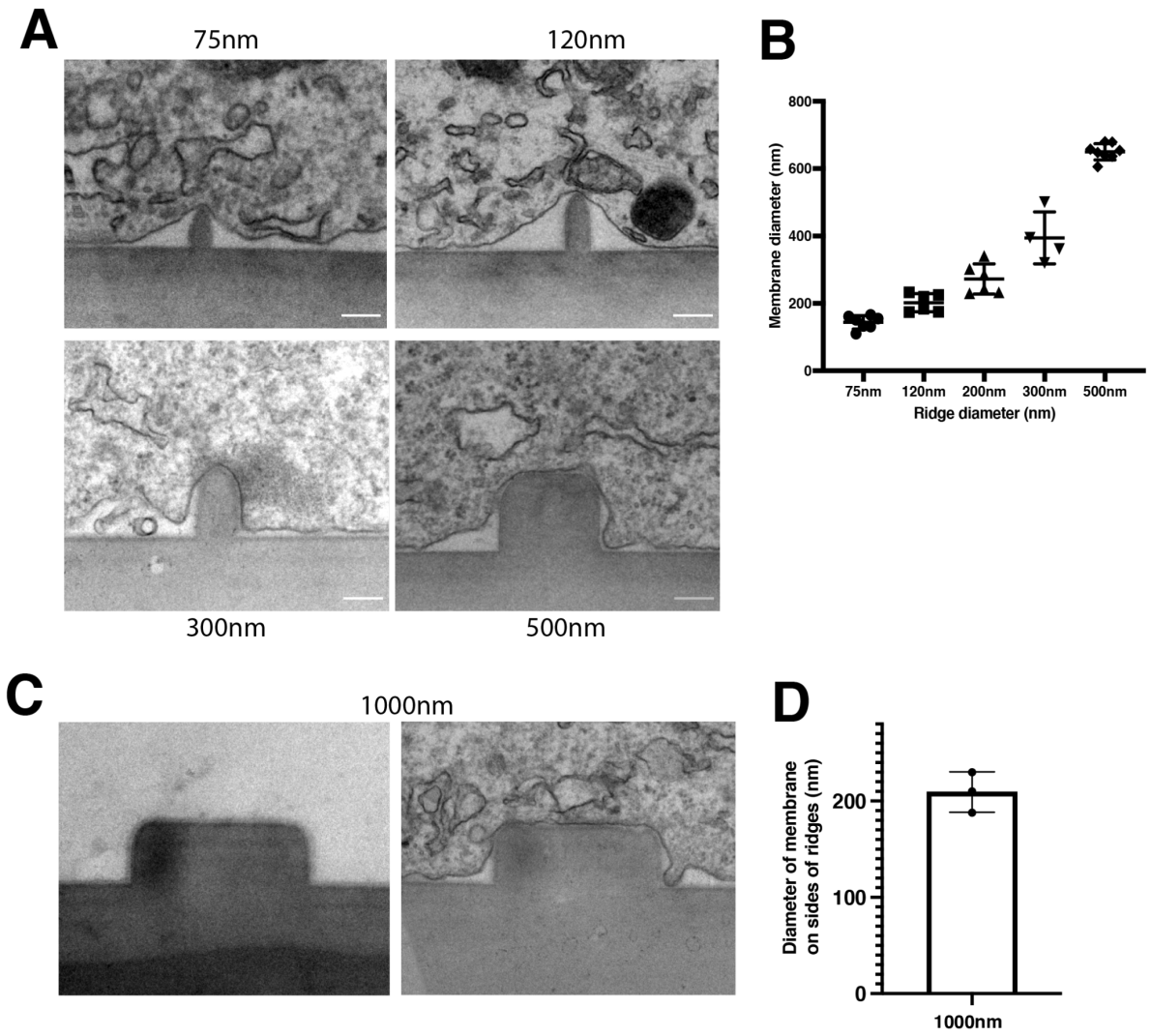

Figure 3.4 Correlative light-electron microscopy of MDA cells to measure the induced radius in response to Ormocomp substrates. A) Representative images of thin-section TEM cells on nanordiges demonstrates the radius of membrane in response to the radius of the nanoridge, with quantification in (B). Scale bars 100 nanometers. C) TEM of bare and membrane-bound 1000nm substrate revealing that the top is flat and the sides curved in response to 1000nm shape, with quantification in (D).

Endocytic proteins localize to substrates as a function of curvature

We next wanted to carry out a screen of endocytic proteins to measure their response to curvature. While the refractive index of Ormocomp is already optimal for optical microscopy, it was not known how the structure of an evanescent field would respond to the nanoridge structure imposed upon Ormocomp substrates, given that the nanoridges are on the order of the wavelength of visible light or smaller (<500 nm). Previous experiments leveraging a TIRF microscope with structured substrates such as zero-mode waveguides have been used for selective illumination of small volumes, or for structured illumination superresolution microscopy (Levene et al., 2003; Byun et al., 2017). Thus, testing the optical response of a cell

atop the nanoridge substrates was essential for determining the reliability of endocytic protein responses to curvature.

To test how the TIRF field was affected by our nanopatterned substrates, we varied the polar (ie, in the X-Z plane of the objective) and azimuthal (X-Y plane of the objective) angles of the TIRF illumination laser with cells grown atop the nanoridges (Fig 3.5). We tested both the cell membrane marker CellMask Orange (CMO) and the endocytic protein dynamin2 (DNM2). For cells on flat Ormocomp, the response was nearly identical to borosilicate glass coverslips, although with slightly decreased signal-to-noise ratio (SNR) over glass because of the slight autofluorescence of Ormocomp (Fig 3.5A).

On the nanoridge substrates, the illumination efficiency was largely unchanged by the polar angle, similar to flat substrates—while the background fluorescence increased because of increased penetration of the illumination laser. However, the illumination of fluorophores was very sensitive to the azimuthal angle. When the azimuthal angle was perpendicular to the nanoridges, there was very little illumination of the fluorophores of membrane stain CMO. However, as the azimuthal angle became more parallel, the illumination increased until it maximized at perfectly parallel angles (Fig 3.5B). Scaled-up intensity images of non-parallel illumination angles revealed that membrane staining was reduced on nanoridges relative to background, indicating decreased penetration of the evanescent field into the nanoridges (Fig 3.5C). The illumination of DNM2-GFP was similarly sensitive to illumination angle; interestingly, while DNM2-GFP puncta were visible between ridges at more perpendicular azimuthal angles, there was a striking number of puncta on the nanoridges when the azimuthal angle was parallel, indicating that the penetration of the evanescent field into the substrate is dependent on the angle at which the laser interacts with the nanoridge (Fig 3.5C).

We then screened proteins across stages of CME to determine the response of endocytic sites to the diameter of induced curvature (Fig 3.6A). There was a clear response of early proteins AP2-RFP and CLTA-RFP to smallest curvature, with decreasing response as nanoridge size increased. Intermediate- and late-arriving proteins EPN1-GFP and DNM2-GFP also demonstrated a striking increase in puncta number on high curvature. The protein CAV1-RFP, a component of the caveolin coat, demonstrated no increase at highest curvature and, in fact, seemed to show a bigger increase in puncta number on larger substrates such as the 500nm ridge (Rothberg et al., 1992). On the 1000nm ridge, the proteins preferentially localized to the high-curvature edges of the ridge, rather than the central part, consistent with the principle that curvature rather than raised substrate was the driver of localization (Fig 3.6B-C). To quantify the enrichment, we developed computational processing tools for automated, unbiased detections.

Computational image processing development

To quantify the robustness of protein enrichment on sites of high curvature, it was necessary to develop computational tools with the following key attributes: 1) Automated, so that the tools can work on the same types of data from different cells, days, etc; 2) Unbiased, so that quantification represents true effects and not sensitivity to the human eye; and 3) High-throughput, so as to gain large statistical power from the thousands of endocytic events happening simultaneously within the cell.

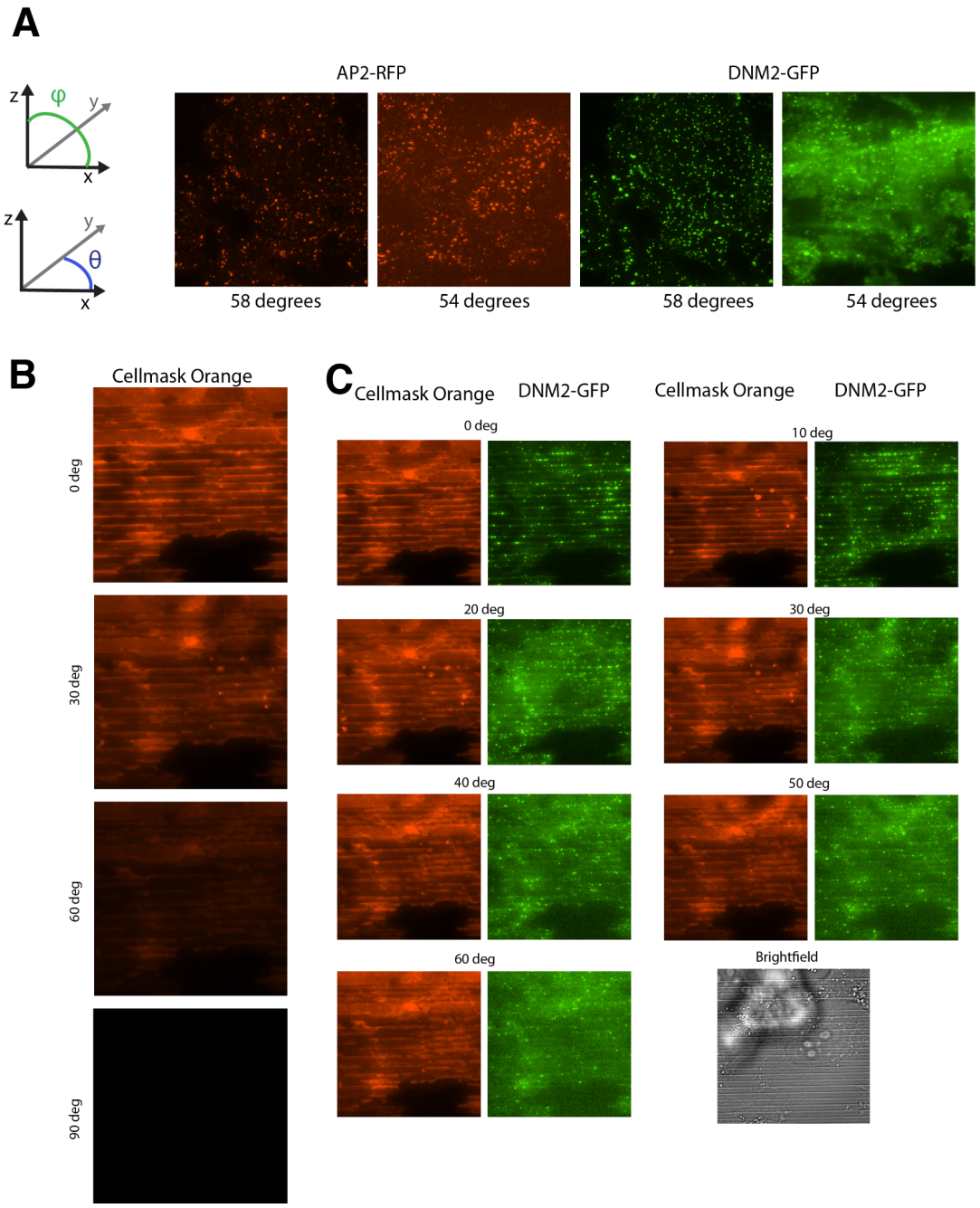

Figure 3.5 TIRF microscopy on Ormocomp nanoridges. A) Cellular response to altering the polar angle of the TIRF microscope, demonstrating increased background at lower angle, as occurs on glass coverslips. B) Varying the azimuthal angle of the TIRF microscope strongly decreases the illumination of the cell membrane marker CellMask Orange. Optimal illumination occurs when the angle of illumination aligns with the angle of the nanoridge. C) Scaled-up intensity images of CellMask Orange and DNM2-GFP with varying azimuthal angle, demonstrating the decrease in on-ridge fluorescence as the mismatch between nanoridge angle and azimuthal angle increases, probably because of decrease of photon penetration of the nanoridge as the angle increases.

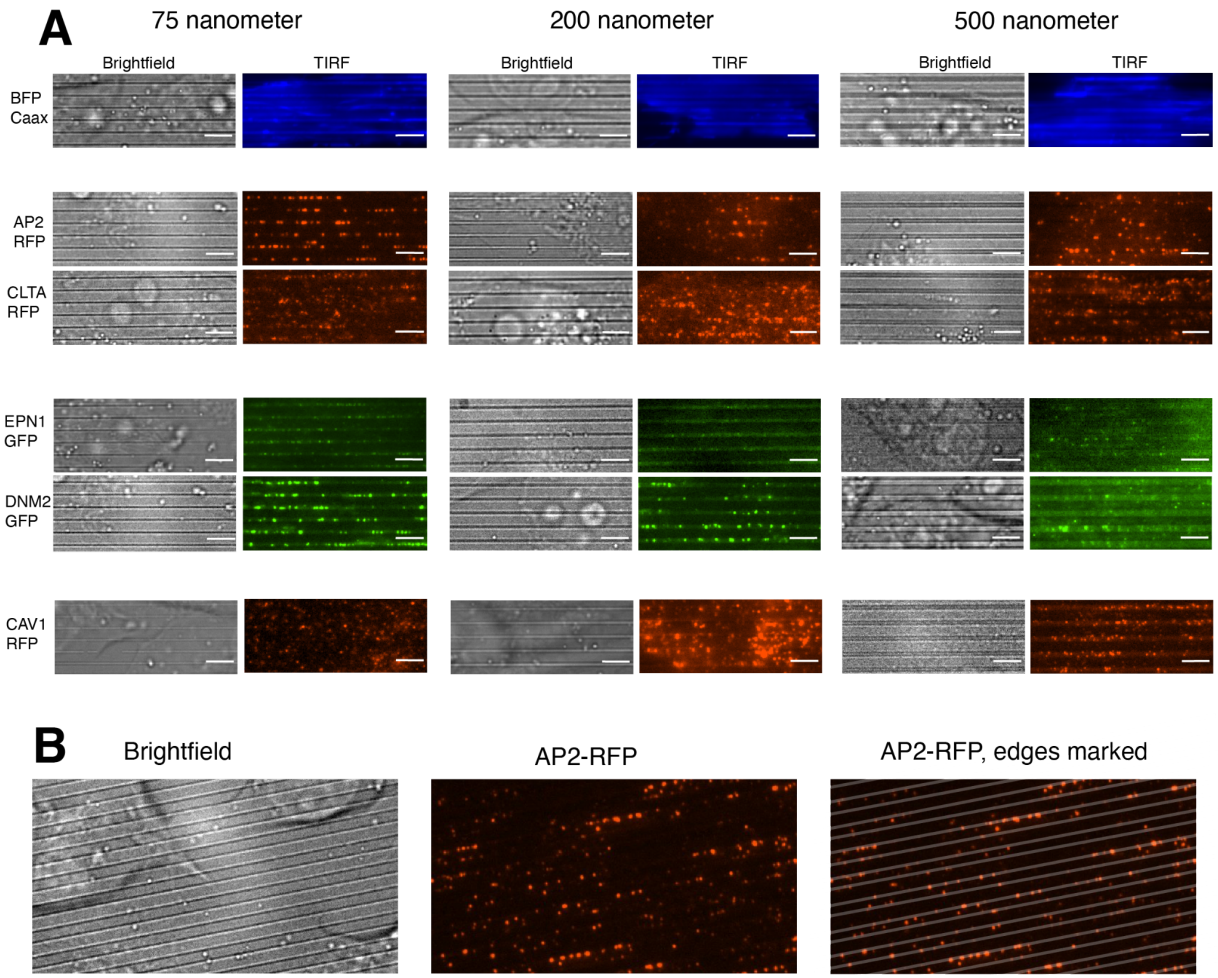

Figure 3.6 Survey of endocytic proteins on nanoridges showing response to curvature. A) BFP-Caax illumination reveals the entire ventral cell membrane is illuminated, while early (AP2-RFP,
CLTA-RFP), intermediate (EPN1-GFP), and late (DNM2-GFP) endocytic proteins are strongly enriched on nanoridges. CAV1-RFP, a marker of another endocytic machinery, is not strongly localized to the nanoridges. Scale bars 4 microns. B) Response of AP2-RFP to the 1000nm ridge, where there is enrichment to the highly-curved edges, showing that the response of CME proteins is to curvature rather than the raised portion of the nanoridge.

Many tools for fluorescence microscopy have been developed that detect, correlate, and track fluorescent signals over time. The key addition necessary for our endocytic quantification was the on-vs-off nanoridge localization. Because the nanoridges are visible in brightfield imaging and have a linear structure, we chose to apply the Hough transform, a standard form of line detection in computer vision algorithms, to automatically detect lines and create a mask that bins on- or off-ridge puncta (Aggarwal and Karl, 2006). This system, requiring only a few minutes per image, allowed for robust and flexible masks that could be applied to many different imaging

modalities and types of analysis. We tested several methods of puncta detection (see Methods) and found highest reliability from the FIJI plugin TrackMate.

To test whether puncta were on or off the ridges, X and Y positions of puncta were loaded into a Jupyter notebook along with the mask array created using the bright field image. The X-Y coordinates of puncta were compared against positions of the mask (see Methods). The results of this algorithm formed the basis of the enrichment score, which was calculated as the percentage of puncta within a mask divided by the corrected area of the mask. To accurately calculate the enrichment score for individual endocytic proteins, we needed to measure the increase in membrane present on nanoridges, as the semi-circular shape created a relatively higher amount of membrane present over an equivalent number of pixels on flat substrate.

Membrane area corrections on nanoridges

We used two fluorescent membrane markers to determine the membrane increase: the lipophilic dye CellMask Orange (CMO) and TagBFP2 fused to a membrane-linking Caax box (BFP-Caax) (Fig 3.7A). Both of these membrane markers demonstrated an increase in fluorescence intensity atop the nanoridges relative to flat regions either in between the ridge or on adjacent flat Ormocomp (Fig 3.7B, see Methods). This method offered two practical advantages over theoretical calculation: 1) It was simple to apply, requiring only components that were already involved in establishing that the entire ventral surface of a cell was illuminated by the TIRF field of the microscope, and 2) It represents an empirical measurement on the same microscope from which all other measurements were collected, automatically correcting for changes in the evanescent field induced by the Ormocomp nanoridges; thus, any increase in likelihood of exciting a fluorophore atop a ridge or in between was accounted for by correcting against fluorophores with even distribution across the ventral cell membrane.

Enrichment of endocytic proteins on substrates

The final enrichment score is therefore the percentage of spots on a mask divided by the area of the mask and the mask correction factor. The results for these measurements are summarized in Fig 3.8A. The enrichment for AP2 was nearly 4 fold at the 75 nm mask, indicating a 4-fold increase in likelihood of an endocytic site forming on such a region relative to elsewhere within the cell. This enrichment decreased with decreasing curvature until, at 500 nm diameter, there was essentially no increase in AP2 enrichment. For the intermediate- and late-arriving endocytic proteins epsin1 and dynamin2, respectively, the enrichment was even more striking, at >4 fold for highest curvature, indicating that there is an even higher likelihood of localizing the later-stage endocytic proteins. Swapping the fluorophores on AP2 and DNM2 to GFP and RFP, respectively, resulted in little difference in the enrichment, indicating that the effect is not from fluorophores but from the proteins themselves (Fig 3.8B-C).

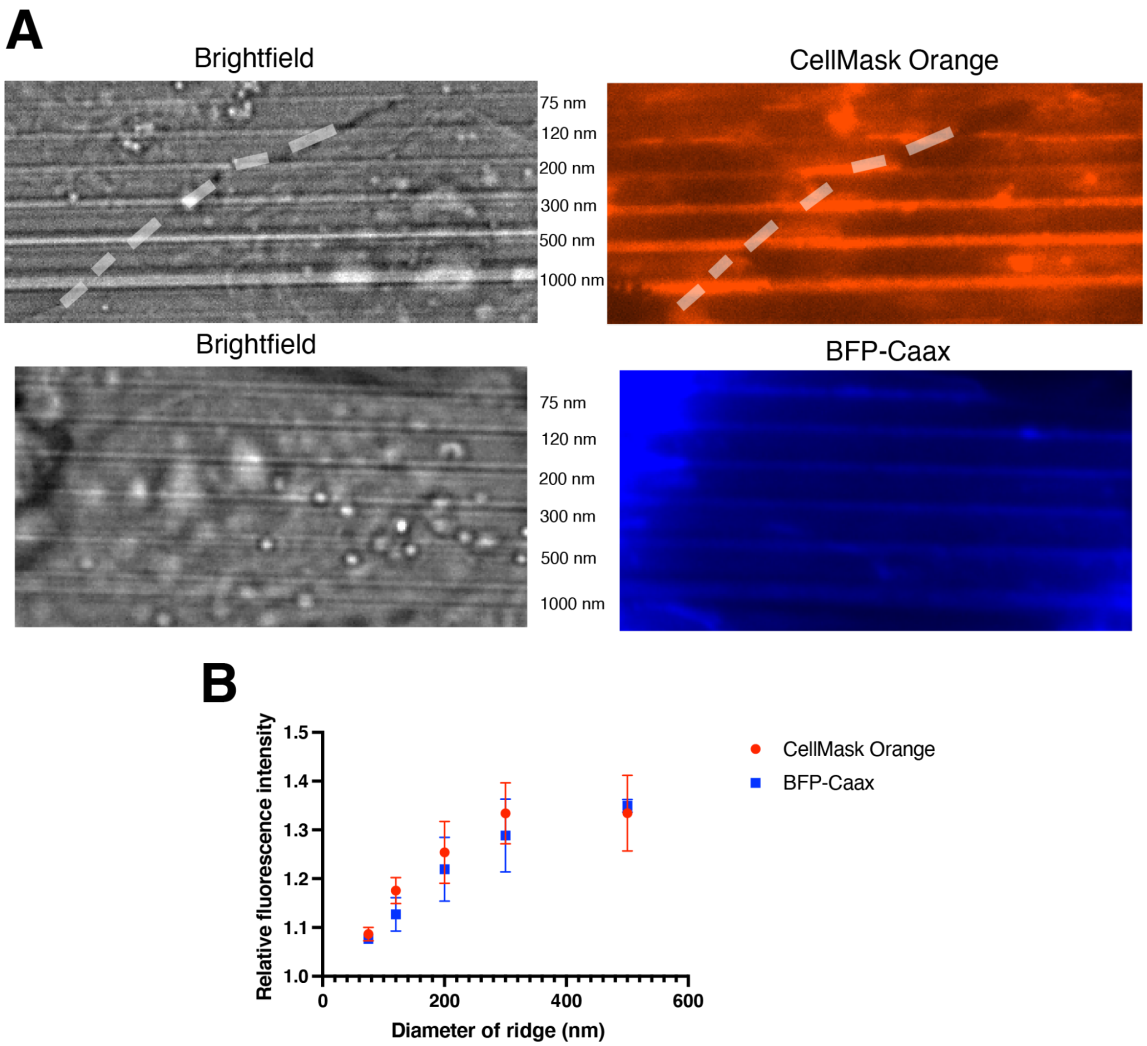

Figure 3.7 Cell membrane area increases as nanoridge size increases. A) example images of CellMask Orange and BFP-Caax showing the increase in fluorescence response on nanoridges vs in-between. B) Quantification of the increases from CellMask Orange and BFP-Caax fluorescence intensity.

The protein clathrin light chain A, a component of the clathrin coat complex, had a robust increase of ~3 at highest curvature but precipitously dropped off as curvature decreased. We hypothesize that, because clathrin is present at other trafficking events within the cell such as the *trans*-Golgi network and endosomes, and because the TIRF illumination employed on nanoridge substrates was significantly deeper within the cell than standard flat-glass TIRF, the presence of non-CME clathrin puncta confounded the measurement of clathrin enrichment at sites of high curvature. Consistent with this hypothesis, there are many more puncta of clathrin light chain A visible within an image than there are of AP2, epsin1, or dyamin2.

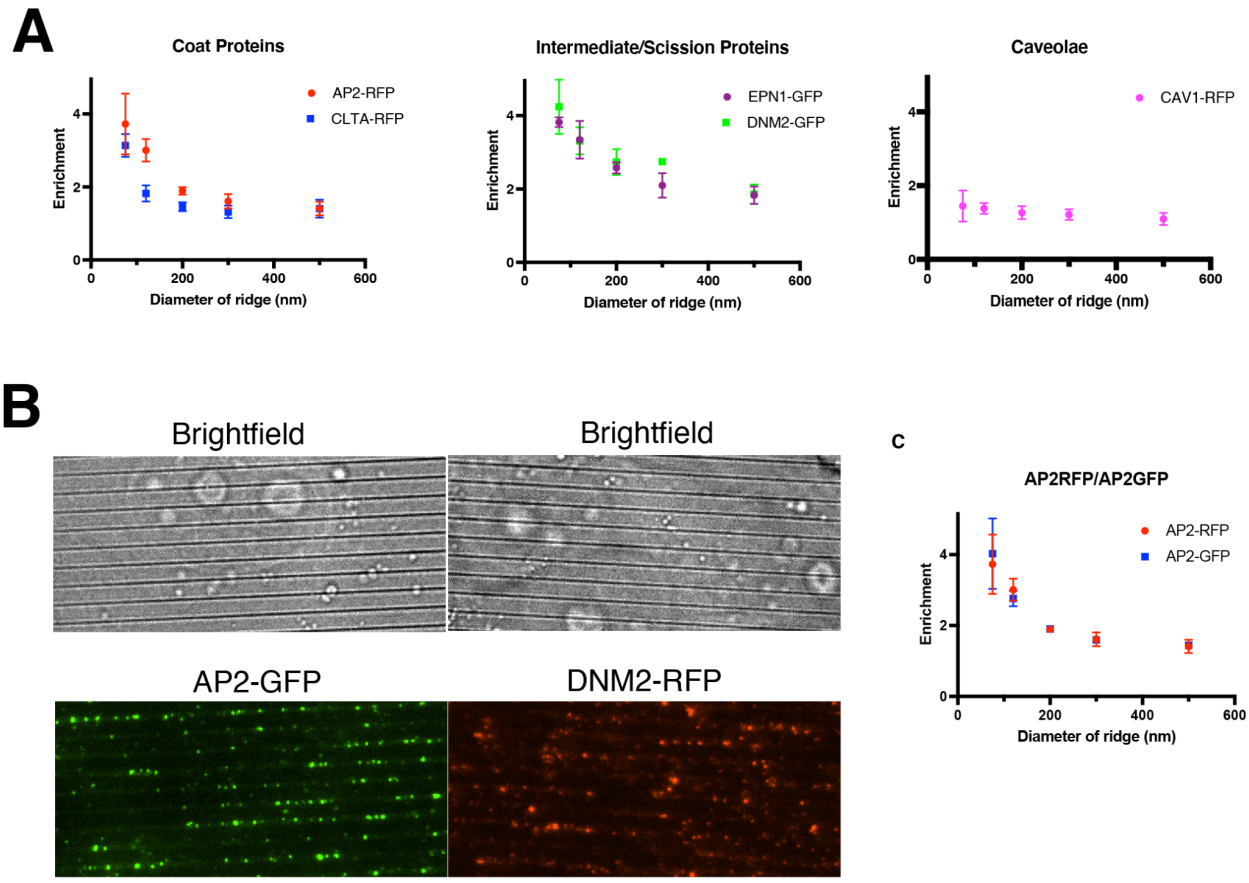

Figure 3.8 Enrichment score for endocytic proteins. A) Enrichment score for early (left) and intermediate/late (middle) endocytic proteins shows a strong response to high curvature, with ~4-fold enrichment of endocytic proteins on the 75nm nanoridges. CAV1-RFP (right) demonstrates no enrichment in response to curvature. B) GFP/RFP-swapped fluorescent proteins demonstrate the same enrichment in response to curvature, showing that the type of FP fusion does not affect enrichment score.

To test the specificity of curvature for clathrin-mediated endocytosis, we also measured the enrichment of caveolin1, a protein marking the coat of caveolar endocytic sites. This protein demonstrated no enrichment on sites of high curvature, with a consistent enrichment score of approximately 1 for all nanoridge sizes. We hypothesize that this difference propensity to be enriched by induced curvature is because of the distinct methods of curvature generation that are employed for the two types of endocytosis: while CME requires rapid evolution from flat to curved membrane, the caveolar endocytic network establishes semi-permanent membrane invaginations.

Endocytic sites on nanoridges are valid CCPs with increased lifetime

Once we had established that nanoscale Ormocomp ridges localize the endocytic machinery, we wondered whether these localizations were true endocytic sites, another structure such as tubular clathrin/AP2 lattices (TCALs), or an ectopic protein localization. Kymographs and montages of individual events on flat substrates as well as on substrates with induced curvature showed

phenotypically similar, canonical endocytic sites, with tracks of gradually increasing AP2-RFP fluorescence followed by a burst of DNM2-GFP marking scission (Fig 3.9A, Fig 3.9B). To determine statistically the effect of curvature on endocytic phenotype, we used an established MATLAB program endocytic site detection and tracking known as cmeAnalysis, as well as custom python post-processing tools for valid track selection and categorization.

MATLAB cmeAnalysis detects tens of thousands of putative endocytic sites within a 300 second movie, because of its highly sensitive Laplacian-of-Gaussian detector. Many of these detections do not correspond to a productive endocytic site. To select for true endocytic sites, we applied the following criteria, according to previously published standards within the field: 1) lifetime between 18-180 seconds, 2) mean-square displacement (MSD) of no greater than 0.02 micron^2, and 3) at least 4 consecutive frames (ie, 6 seconds) of dynamin2 or CLTA.

We applied these selection criteria to flat Ormocomp substrates and found that the average AP2 lifetime was 50.9 +/- 28s, which is very similar to previously reported values on glass (approximately 47 seconds) (Fig 3.9C). Upon selection for sites on induced curvature, we found, to our surprise, an increase in lifetime, to 58.4 +/- 30s on 75 nm, 54.8 +/- 28s on 120 nm, and 53.5 +/- 29s on 200 nm ridges. On 300 nm and higher nanoridges, there was no difference in lifetime relative to flat substrates. By binning the endocytic sites according to lifetime and aligning the intensity profiles, we found the average endocytic profile of automatically-detected CME sites was the same across substrate size, with the canonical rise in AP2-RFP fluorescence followed by burst of DNM2-GFP fluorescence (Fig 3.9D). Profiles of AP2-GFP with CLTA-RFP demonstrated that the two fluorophores follow an identical profile of gradual increase and decrease, showing the concomitant buildup of AP2 and clathrin at an endocytic site prior to internalization (Fig 3.10). CLTA-RFP is a much weaker fluorophore, present at substoichiometric numbers relative to AP2-GFP, causing its much lower fluorescence intensity in binned cohorts (Cocucci et al., 2012).

This lifetime increase for valid endocytic events on high curvature is in conflict with previous findings, in which clathrin light chain lifetime was shorter on 200-nm nanobars than on flat quartz neighboring the nanobars (Zhao et al, 2017). This difference may be because of the more stringent selection criteria for valid tracks employed here, or the settings for tracking and gap closing chosen in cmeAnalysis. It may, however, be a consequence of different materials and geometries of nanofabrication—in particular, nanoridges have high mean but zero Gaussian curvature, whereas nanobars have higher Gaussian curvature and so may require less transition to Gaussian curvature for a productive clathrin-coated pit to form.

The increase in lifetime on nanoridges is consistent with the finding that AP2 lifetimes increase in response to collagen fibers, which have a similar shape to nanoridges; thus, this increase in lifetime might be because of a templating of adhesion molecules such as integrins in response to curvature (Elkhatib et al., 2017). It may also be due to an affinity for curvature on the part of AP2 or other endocytic proteins that require more energy to detach from curved substrates, or because of a higher energy barrier to transition to the Gaussian curvature of a clathrin-coated pit from mean curvature.

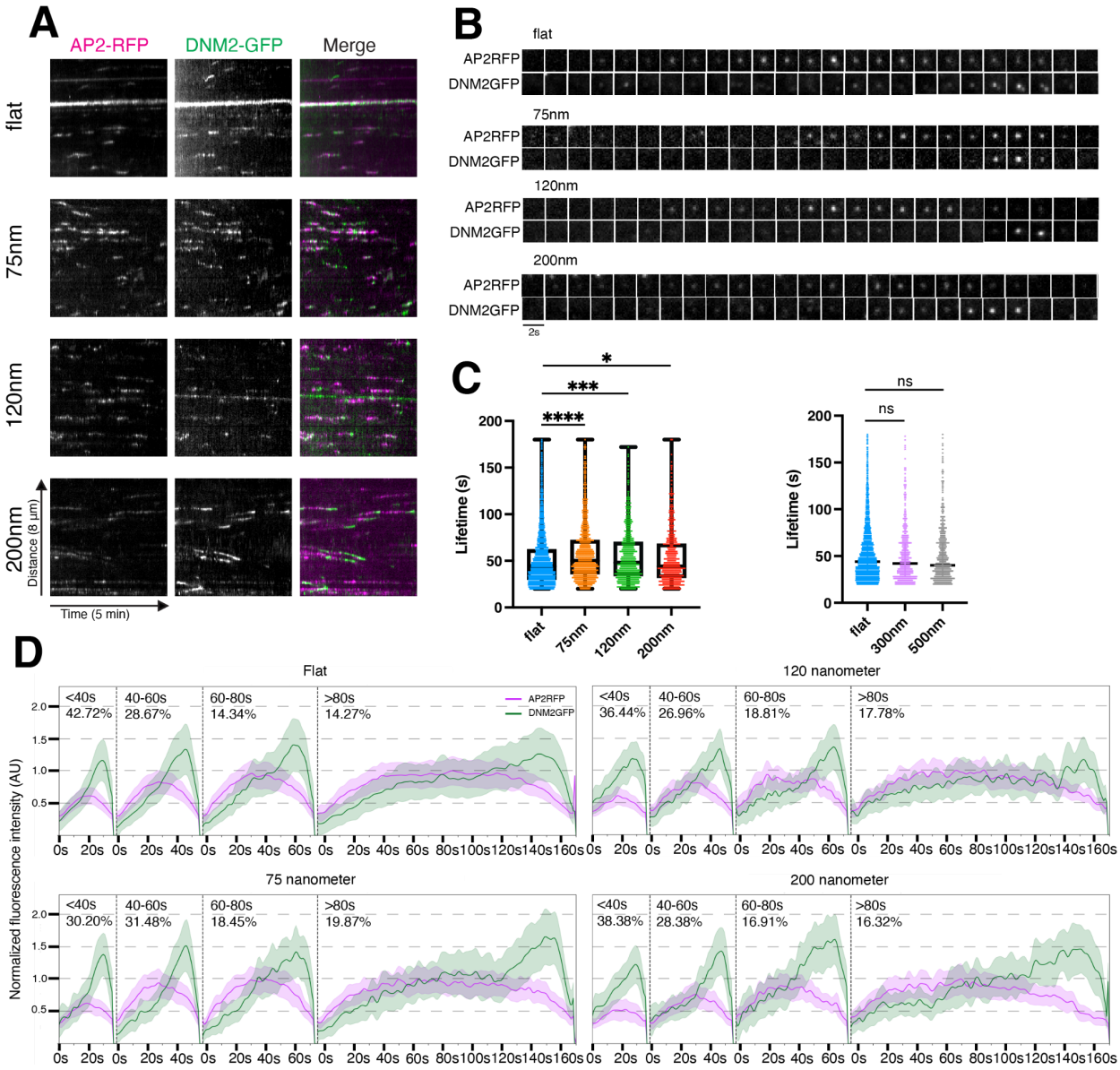

Figure 3.9 Dynamics of CME sites on induced curvature. A) Representative kymographs of AP2-RFP/DNM2-GFP from flat or curved Ormocomp substrates. B) Representative montages of valid clathrin-coated pits (CCPs) showing the gradual increase in AP2-RFP followed by a burst of DNM2-GFP, a hallmark of productive vesiculation. C) Average lifetime of valid CCPs showing an increase of lifetime on sizes <200nm, with no difference above 200nm. D) Binned and average fluorescence profiles for endocytic sites on ridges across curvatures, showing that the sites have the same fluorescence profile irrespective of curvature.

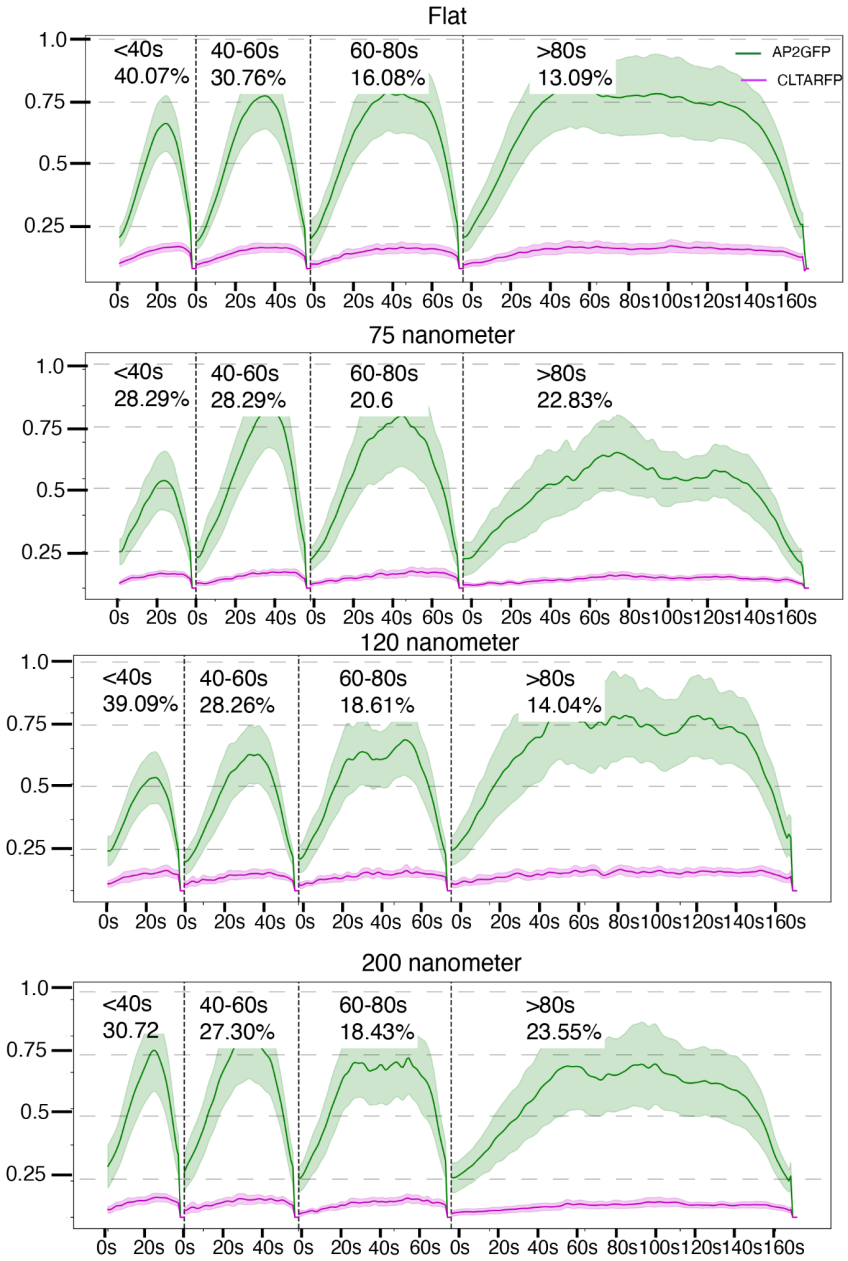

Figure 3.10 Binned average fluorescence intensity profiles for AP2-GFP/ CLTA-RFP cells, demonstrating the same average fluorescence profile of CLTA-RFP on flat or nanoridge substrates, as well as AP2.

Despite the slightly increased lifetime of endocytic sites on nanoridges, there was no difference in the percentages of transient, broken, incomplete, or persistent CCPs as a function of curvature (Fig 3.11A). Additionally, there was no detectable difference in the uptake of fluorescent transferrin after serum starvation and 2-minute pulse of AlexaFluor-647 tagged transferrin on nanoridges of different sizes (Fig 3.11B-C). There was a nanoridge-dependent increase in displacement of CCPs in the last 10 seconds of their lifetime relative to the first 10 seconds, indicating higher migration on nanoridges at late CME stages (Fig 3.11D). Additionally, in TEM, there were examples of near-scission CCPs visible on the edges of nanoridges, along with early

Figure 3.11 Further characterization of CCPs on substrates. A) Nanoridge size does not change the percentage of valid, gapped, incomplete, or persistent CCPs. B) Fluorescent transferrin uptake on nanoridge substrates demonstrates hundreds of puncta of transferrin on each ridge size, showing no difference in bulk rate of endocytosis in response to substrate size. Scale bars 10 microns. Quantification in (C). D) Displacement in the first (left) and last (right) 10 seconds of CCP lifetime shows an increase in mean-square displacement at the end of CCPs on nanoridges, evidence that CCPs migrate off of the nanoridge at a late stage prior to scission. E) Example TEM images of cells on 120nm nanoridges, with CCPs coming from the side of the ridge. Scale bars 100 nanometers.

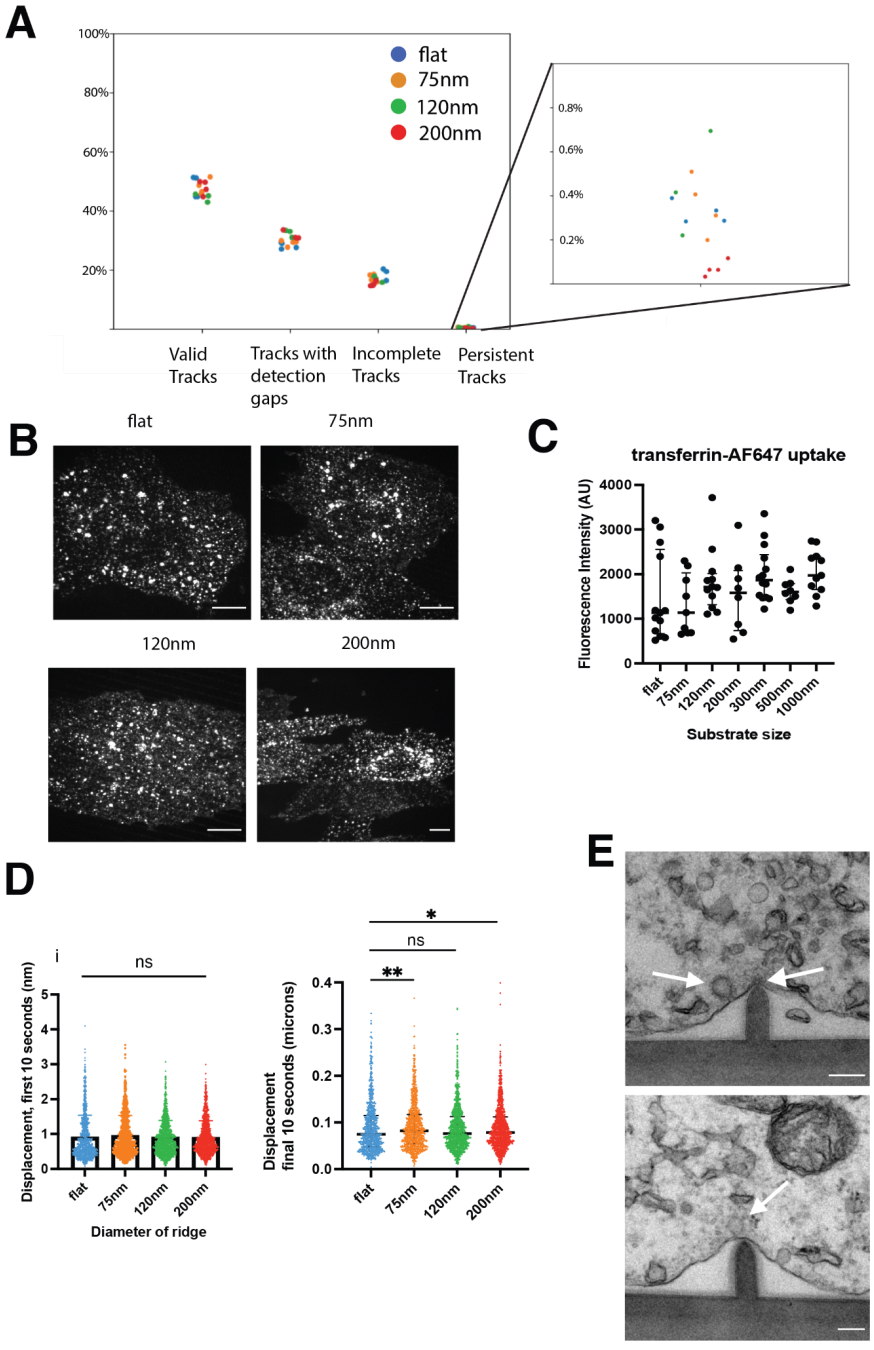

coat stages atop nanoridges, as indicated by the classic spiked coat (Fig 3.11E). These data indicate that the nanoridges induce the localization of nascent CME sites and assist in producing canonical CCPs, which often migrate off the ridge for scission.

Unroofed cells demonstrate the same localization of endocytic proteins to sites of high curvature

We wanted to try platinum-replica EM on substrate-grown cells to visualize the ultrastructure of clathrin lattices on induced curvature. To achieve this, we first had to unroof cells on Ormocomp substrates. Our first attempt at creating platinum replicas failed because of an issue removing the Ormocomp from the platinum replica. However, prior to the COVID shutdown, we found that unroofing MDA cells on Ormocomp worked surprisingly well: there was a clear removal of most cellular components, with only faint membrane shadows left visible by brightfield microscopy (Fig 3.12A). We also found that AP2RFP and DNM2GFP still strongly localized to the sites of high curvature after unroofing (Fig 3.12B). We believe this is a promising route to follow for electron microscopy and also for templating a membrane on Ormocomp substrates, atop which reconstitution experiments can be done.

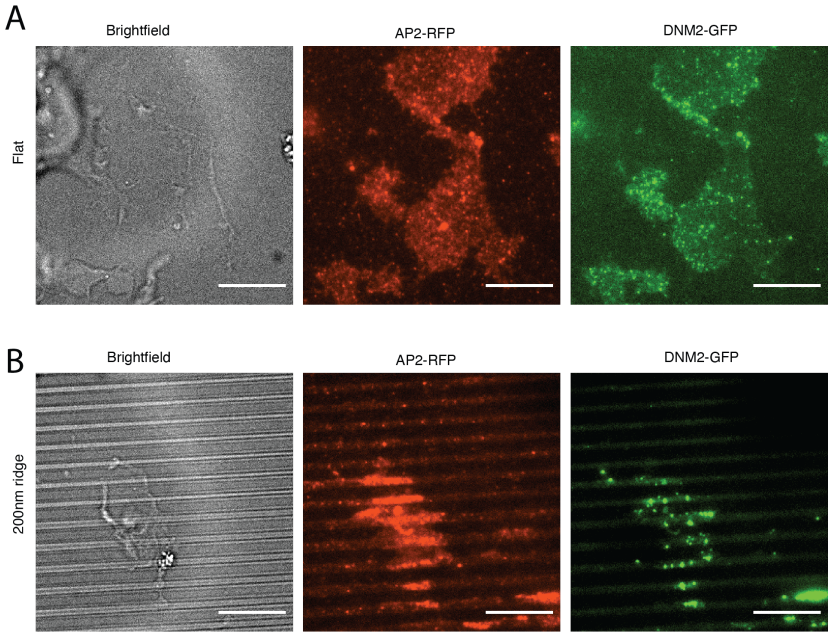

Figure 3.12 Unroofed cells bear curvature enrichment of endocytic proteins. A) Representative image of unroofed MDA cell on flat substrate, with intact cell partially visible to left side of image. B) Example image of unroofed cell from nanoridge substrate, with enriched puncta on curved portions. Scale bars 10 microns.

Methods

Transfection

BFP-Caax in mammalian expression vector (pTagBFP2-C1), a generous gift from the Michael Rape lab (UC Berkeley), was transfected into cells on Ormocomp substrates at 70% confluence using lipofectamine 3000 (Invitrogen L3000008) according to manufacturer protocols (https://tools.thermofisher.com/content/sfs/manuals/lipofectamine3000_protocol.pdf). Cells were imaged 18-24 hours after transfection. CellMask Orange (Invitrogen C10045) was diluted 1000x in media prior to staining; staining was performed for 10 minutes at 37 degrees, followed by two washes in fresh 37-degree media prior to imaging.

CLEM substrate manufacturing

To isolate CLEM dishes, we first soaked the Mattek plates containing CLEM dishes in acetone to remove the glue adhering the plate to the dish overnight; then, carefully isolated the etched CLEM dishes with a razor, creating CLEM dishes ready to act as a base for nanofabrication. Ormocomp substrate manufacturing on CLEM dishes was the same as on glass coverslips but with the following modifications: 1) CLEM dishes were baked in the 180-degree oven for 15 minutes after isopropanol cleaning. 2) Approximately 20 microliters of Ormocomp were applied to the mold prior to adhering it to the HMDS-coated CLEM dish. 3) Care was taken to ensure that the Ormocomp reached outside the edges of the CLEM dish to i) even out the surface if any excess glue remained and ii) allow for easier removal of the substrate from the mold after polymerization.

Preparation for TEM

Briefly, cells were fixed in 2% gluteraldehyde in cytoskeleton stabilization buffer (100 mM methyl ester sulfonate, 150 mM NaCl, 5 mM EGTA, 5 mM MgCl2, and 5 mM glucose in ddH2O, pH 6.8), rinsed 3x in PBS pH 7.4, stained in 1% Osmium tetroxide and 1.6% Potassium ferricyanide in PBS pH 7.4, and rinsed 3x in PBS pH 7.4. Cells were dehydrated in 7-minute washes in 30%, 50%, 70%, 95%, 100%, and 100% ice-cold ethanol and infiltrated in epon-araldite resin. Resin was polymerized in a 60-degree oven for 24 hours. Next, 70 nm sections were cut with an Ultracut E (Leica) and collected onto formvar-coated 50 mesh copper grids. Grids were post-stained with 2% uranyl acetate followed by Reynold's lead citrate for 5 minutes each. Sections were imaged using a Tecnai 12 120kV TEM (FEI) and data recorded using an UltraScan 1000 with Digital Micrograph 3 software (Gatan Inc.). Membrane diameter measurements were made using ImageJ.

Automated line detection

The following steps were implemented for line detection:

0) Capture a brightfield image at the outset of fluorescence microscopy.
1) Convert the bit depth of the brightfield image to RGB.
2) Smooth the image with a 5x5 Gaussian kernel.
3) Take the Hough transform of the image and find all linear structures.
4) Find the dominant mode of the linear features (ie, the common slope).
5) Reject all features outside a small standard deviation of the dominant mode.
6) Store linear features as X and Y endpoints of a line on either side of the image.
7) Adjust X and Y endpoints to ensure that they overlap with the middle of the linear structure visible in brightfield; this step corrects for errors in Gaussian smoothing or nonlinear chromatic aberrations in the lens system.

8) Draw 1-pixel lines connecting the X and Y endpoints.
9) Using a forward model of line thicknesses based on known ridge sizes fed through the PSF of a microscope (see table), apply a thickness to the 1-pixel lines.
10) Store these lines as a numpy array; where the array is valued 1, the mask considers the image "on-ridge," whereas the array value 0 corresponds to "off-ridge."

Fluorescent puncta detection

To detect and localize fluorescent puncta, we tried several different detection schemes to balance automation against sensitivity (to both false positives and false negatives). First, we applied Cellprofiler 3.1.2, a highly automated puncta detection and localization program (McQuin et al., 2018). This software reliably found the brightest 50% of puncta, but upon increasing the sensitivity of the detection algorithm, it began to find many false positives in particular on the ridges. We next used the detection scheme built into the cmeAnalysis MATLAB package, a standard puncta detection algorithm used in the field of clathrin-mediated endocytosis (Aguet et al., 2013). The puncta detection in cmeAnalysis is built on the Laplacian-of-Gaussian edge detection method as applied in micro track software, which is highly sensitive; in this program, the detection is not tunable, but instead relies on linking across time to filter out false positives (Sherbondi et al., 2010). Thus, unfiltered detections had a number of false positives, but interestingly, the false positive detections were largely on the spaces between nanoridges. These false detections would lead to a lower enrichment than was truly present.

To combine high sensitivity of Gaussian-based edge detection with tunable thresholding, we turned to TrackMate, a more manual detection and tracking method than cmeAnalysis (Tinevez et al., 2017). TrackMate offers the advantage of multiple edge detection schemes with manually adjusted thresholds to allow for optimal selection of positive detections rather than noisy background detections. Through trial and error, it was found that the best results came from the Differences-of-Gaussians (DoG) mode with Gaussian smoothing, which corrected for background fluorescence from the nanoridges. Threshold settings of 8 for GFP fusion proteins and 3-4 for RFP fusion proteins offered optimal detections of puncta without false positive detections. Thus, these settings were chosen to detect the puncta. Subpixel localization allowed for localizing the puncta within the image. Saving the localizations as CSV files allowed for easy import and manipulation with custom python analysis packages.

Alignment to mask

Masks of nanoridges were generated as binary 512x512 numpy arrays, where nanoridge positions were 1 and off-nanoridge positions were 0. Puncta X-Y coordinates, as determined by TrackMate, were loaded into python and the distance to the nearest mask position for each punctum was calculated by 1) determining the distance to each mask pixel (ie, every 1 in the numpy array) and 2) finding the smallest value of calculation (1). If that smallest value was below 1, the punctum was considered on-mask; above 1, it was considered off-mask.

Membrane area correction

To quantify the increase in membrane area because of the curvature of the ridge, we drew ROIs around the nanoridges, measured the fluorescence intensity, and subtracted background from adjacent bare ridges (i.e., without cells atop them) to assess the fluorescence of membrane atop a ridge. We next measured the fluorescence intensity from equal-sized ROIs on a patch of flat

membrane between the nanoridges and corrected for bare fluorescence from background ridges to assess the fluorescence of the membrane on a flat substrate. By comparing the corrected fluorescence from nanoridge vs flat substrate, we calculated a ratiometric increase in membrane due to the curvature of a nanoridge

Microscopy

TIRF microscopy was carried out using a Nikon Eclipse Ti2 TIRF microscope with Hamamatsu Orca 4.0 sCMOS camera operated by Nikon Elements software. The TIRF angle was adjusted to pseudo-TIRF to create an evanescent field of approximately 300 nanometers, extending above the bottom of the pillars to ensure illumination of the membrane on the top of the pillars. These movies were formatted for cmeAnalysis processing using AP2 as the primary channel and either DNM2 or CLTA as correlated channels, and tracked with standard model settings (Gaussian PSF, 3-6 pixel maximum search radius, and standard gap closing), loading output into Jupyter for further processing and analysis.

Transferrin uptake assay

Transferrin uptake assays were performed by serum-starving cells in DMEM/f12 with 0.5% (w/v) BSA (Sigma Life Sciences A9647) for 30 minutes followed by adding fresh DMEM/f12/BSA with alexa-fluor 647-labeled transferrin at a concentration of 10 micrograms/milliliter (Jackson Immunoresesarch 009-600-050). Cells were exposed to transferrin for 2 minutes followed by a 2 minute chase in fresh DMEM/f12/BSA. Cells were then washed 1x with ice-cold DPBS. Cells were fixed in 4% paraformaldehyde (Electron Microscopy Solutions) in Tris/potassium chloride cytoskeleton buffer (10mM MES, 150mM NaCl, 5mM EGTA, 5mM glucose, 5mM MgCl2, 0.005% Sodium Azide, pH 6.1) for 20 minutes at room temperature, followed by 3 x 5-minute washes in 50mM ammonium chloride in cytoskeleton buffer, and mounted on microscope slide in fluorescence mounting medium (Vectashield H-2000) and either imaged immediately on a confocal microscope or stored at 4 degrees overnight before imaging.

Confocal microscopy for transferrin uptake assays was done on a Nikon Eclipse Ti microscope with Yokogawa spinning disk and Andor EMCCD, operated by Nikon Elements software. Entire cell volumes were collected at Nyquist sampling frequency (200nm per Z-section), and maximum intensity projections were created in ImageJ for analysis.

Puncta detection and postprocessing

Puncta of endocytic proteins were detected using Trackmate 6.0.3 in Differences-of-Gaussians mode. Nanoridges were detected using custom Python scripts built on the Hough transform in Python package cv2. TIRF videos were analyzed using the MATLAB cmeAnalysis package. Standard settings for model-based detection, Gaussian fitting, radius of detection, and gap closing were selected. Further postprocessing was completed using custom Python scripts, available at github.com/drubinbarneslab. Valid endocytic sites were selected based on lifetime limits of 18-180 seconds, MSD measurement of 0.02 micron^2, and at least 4 consecutive seconds of dynamin2 detection, as has been previously reported for valid CCPs (Pascolutti et al., 2019).

Statistical analysis

Statistical analyses were conducted either with python packages NumPy, Pandas, SciPy, and Seaborns, or with Prism 9. Graphs were produced with Prism 9.

Unroofing

Unroofing of cells was done by shearing cells using a 10 mL syringe (BD biosciences 309604) with a 22 gauge, 1.5 inch needle containing 4 mL of stabilization buffer (70 mM KCl, 30 mM HEPES pH 7.4, 5 mM MgCl2, 3 mM EGTA) with 2% paraformaldehyde. Cells were sprayed evenly in one pass, followed by incubation in 2 mL stabilization buffer with 2% gluteraldehyde for 20 minutes prior to imaging on the TIRF microscope.

Chapter 4
Clathrin disruption, but not other disruptions, is rescued by induced curvature

The principal advantage of Ormocomp substrate manufacturing is its low cost and high throughput, allowing many replicates and exploration of diverse conditions, with precise curvature control. After analyzing the response of endocytic sites to induced membrane curvature, we wanted to use this method to determine which proteins are essential for curvature generation at a CME site, and how curvature generation fits into the timeline of productive vesiculation.

Background

CME is frequently modeled as a modular process, with the following steps: 1) nucleation of an endocytic site, 2) stabilization of the nascent site, 3) curvature generation, 4) force production through the actomyosin network, 5) vesicle scission, and 6) vesicle uncoating prior to trafficking (McMahon and Boucrot, 2011) (Fig 4.1). The modules execute their functions in approximately the order presented above, but with significant temporal overlap. There is debate about the timing of curvature generation vis-a-vis nucleation and stabilization; the two competing models are the constant-curvature model, in which the buildup of the endocytic site is concomitant with the generation of curvature; and the constant-area model, in which an endocytic site builds to its final size on flat membrane and then transitions to curved pit prior to scission (Bucher et al., 2018; Tagiltsev et al., 2021). By manipulating the content of a cell in the presence of stable induced curvature, we hoped to gain insights into how curvature generation fits within the modular CME timeline.

Clathrin functions as an oligomeric complex composed of one heavy chain (called CLTC or CHC) and two light chains (CLTA and CLTB). A heavy chain/light chain dimer forms a

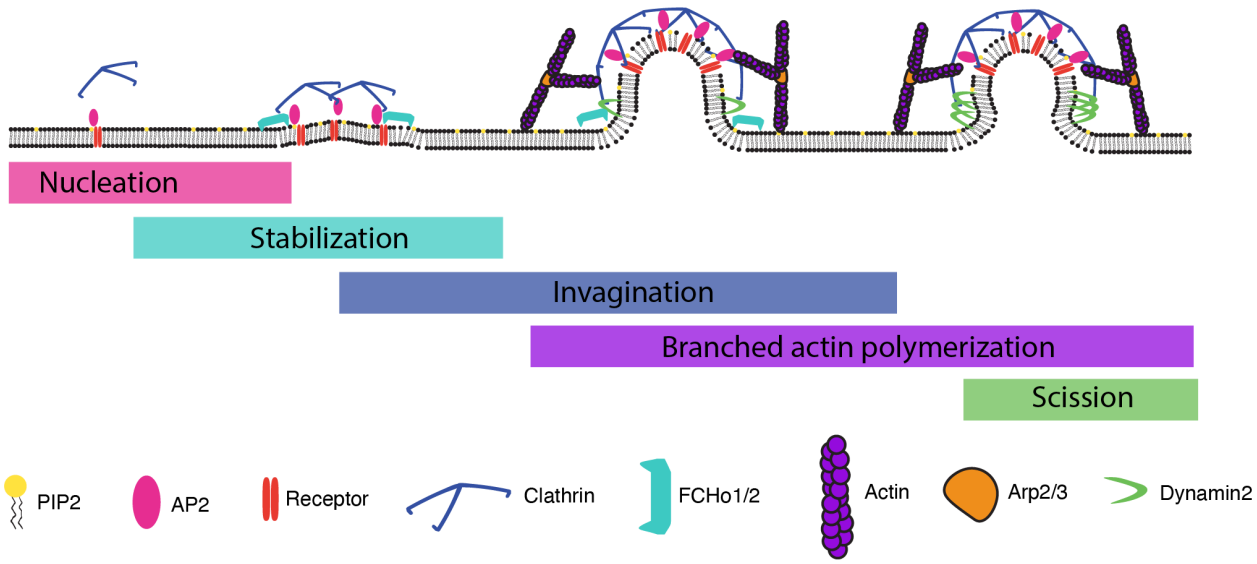

Figure 4.1 Clathrin-mediated endocytosis occurs in overlapping modules, beginning with nucleation of a site and FCHo1/2-dependent stabilization of the nascent site. Curvature is produced during the stabilization and invagination phases, and branched actin produces force as necessary, while the process ends with dynamin2 catalyzing scission.

heterosextamer complex known as a clathrin triskelion, a three-armed polymer of clathrin subunits with approximately 120 degrees between each arm (Ungewickell and Branton, 1981). This complex is thought to assist in curvature generation through bending of the arms downward from the central vertex, forming a small dome. Clathrin triskelia organize largely into hexagons and pentagons to form a soccer-ball shape around a clathrin-coated pit. According to Euler's theorem, 12 pentagons are necessary to form an approximately spherical shape, although the number of hexagons present is flexible (den Otter and Briels, 2011). Electron microscopy of reconstituted clathrin-coated vesicles has demonstrated that *in vitro* a cage of clathrin triskelia can adopt many distinct conformations of different sizes, including dodecahedra, larger spheres with hexagons on the cage, and barrel-shaped clathrin-coated pits (CCPs) (Fotin et al., 2004).

An attractive hypothesis for how the evolution of curvature at a CCP is controlled is termed the Brownian Ratchet model of clathrin function (Henrichsen et al., 2006). In this model, the curvature of an endocytic site is created by various membrane-binding proteins, which have diverse mechanisms for creating curvature, and by thermal fluctuations; the role of clathrin is to lock in the induced curvature, only allowing the invagination to become deeper and not allowing the membrane to relax to its unbent state.

This mechanism is consistent with several important findings: 1) Upon clathrin knockdown, endocytic sites stall as flat patches of protein visible through platinum-replica electron microscopy (Henrichsen et al., 2006). 2) Purified clathrin spontaneously assembles into cage-like structures approximating a sphere (Dannhauser and Ungewickell, 2012). 3) Clathrin is innately curvature-sensing, preferentially binding to small vesicles; however, this affinity for curvature is increased by a factor of 10 with the help of other curvature-sensing CME proteins such as epsin and amphiphysin (Zeno et al., 2021).

However, this model is inconsistent with other findings, namely the presence of clathrin at many distinct membrane shapes, principally the flat clathrin lattice that seems to function as a platform for signaling and assists in cellular adhesion (Leyton-Puig et al., 2017). Current evidence supports a flat-to-curved transition model of CCP formation, in which the endocytic site forms to essentially its final size and clathrin/receptor number on flat membrane, and then, through a mechanism not fully elucidated, curvature is created until a vesicle can be budded into the cell body (Bucher et al., 2018).

Importantly, clathrin also participates in many other functions within the cell, giving it the nickname of a "molecular shapeshifter" (Wood and Smith, 2021). Other endocytic processes do not require clathrin, and in fact may not require coat proteins at all, and so the necessity of curvature stabilization through the clathrin coat is not clear (Sokac et al., 2003). Thus, another potential role for clathrin at CME sites, which is not exclusive or a role in curvature generation, is to assist in the selection and concentration of endocytic receptors and force-producing machinery, rather than creating or stabilizing curvature itself (Traub, 2003). How clathrin fits into the invagination stage of CME mechanistically, and how its role in this subprocess of the CME pathway overlaps with contributions provided by proteins in other modules, can be addressed by manipulating these modules in the context of induced curvature.

Nucleation stage: AP2 knockdown is not rescued by induced curvature

First, we tested the possibility that induced membrane curvature could stabilize endocytic sites in the absence of AP2, a key adaptor protein specific to CME that nucleates an endocytic site. Cytosolic AP2, in a closed conformation, undergoes a change in conformation to its open form and binds to cargoes and PIP_2 on the plasma membrane at the earliest stages of endocytic pit formation (Kelly et al., 2014; Cocucci et al., 2012). In the absence of AP2, CCP formation fails and cells cannot internalize cargoes such as transferrin (Motley et al., 2003). Transfection of MDA-MB-231 cells with siRNA targeting the mu subunit of AP2 resulted in >90% decrease in AP2 expression, as measured by western blot (Fig 4.2A) and fluorescence microscopy (Fig 4.3B). Upon AP2 disruption, there was a clear decrease in number and intensity of CLTA-RFP and DNM2-GFP puncta on flat Ormocomp substrates, indicating a defect in CME site formation (Fig 4.2B). The number of puncta detected by TrackMate decreased two-fold for CLTA-RFP and three-fold for DNM2-GFP (Fig 4.3A), and the intensity decreased 2-fold for CLTA-RFP and 4-fold for DNM2-GFP.

When AP2-knockdown cells were grown on nanoridges, the decrease in CLTA-RFP and DNM2-GFP number and intensity persisted, indicating that induced curvature could not rescue the endocytic site formation in cells lacking the AP2 adaptor protein (Fig 4.2B). The number of puncta detected by TrackMate was unchanged by nanoridge size (Fig 4.3A). This result was accompanied by a decrease in the enrichment score for both CLTA-RFP, from 2.2 to 1.1 on 75nm ridges, and DNM2-GFP, from >4 to <2 on 75nm ridges (Fig 4.2C). CLTA-RFP became essentially curvature-insensitive, suggesting that the remaining puncta detected likely correspond to random detections from non-endocytic clathrin-based trafficking events within the cell (Daboussi et al., 2012). Interestingly, while there was a decrease in DNM2-GFP enrichment relative to control cells, there persisted a modest enrichment at sites of highest curvature; this may be because of dynamin2's role in other endocytic pathways, which may be curvature-sensitive, or because of its binding to PIP_2, which may prefer regions of high curvature (Henley et al., 1998; Schafer et al., 2002).

Stabilization stage: FCHo1/2 knockdown is not rescued by induced curvature, but AP2 still localizes to regions of high curvature

After AP2 marks a nascent endocytic site on the plasma membrane, the pioneer complex of endocytic proteins assists in stabilizing the maturing site as it grows and incorporates receptors. The heterodimer FCHo1/2 is a key component of the stabilizing pioneer complex of CCPs, where it interacts with AP2 through its c-terminal mu homology domain, favoring AP2's open, membrane- and receptor-binding conformation (Pradhan-Sundd et al., 2016). The FCHo1/2 proteins also bind to the membrane through their N-terminal F-BAR domains, which interact with PIP_2 at the nascent endocytic site and induce shallow local curvature (Henne et al., 2010). To assess how curvature influences the stabilization step of CME, we depleted FCHo1/2 using siRNA, which resulted in a decrease of FCHo1/2 expression as demonstrated by western blot and a clear disruption of endocytic site stability by live cell microscopy (Fig 4.4.A).

We visualized AP2RFP/DNM2GFP cells with FCHo1/2 KD by TIRF microscopy, whereupon there was a striking decrease in the number and intensity of puncta of both AP2RFP and DNM2GFP (Fig 4.4B). On flat substrates, the number of AP2RFP puncta, as detected by automated spot detection, decreased >3-fold to 0.6 puncta per square micron; this depletion was

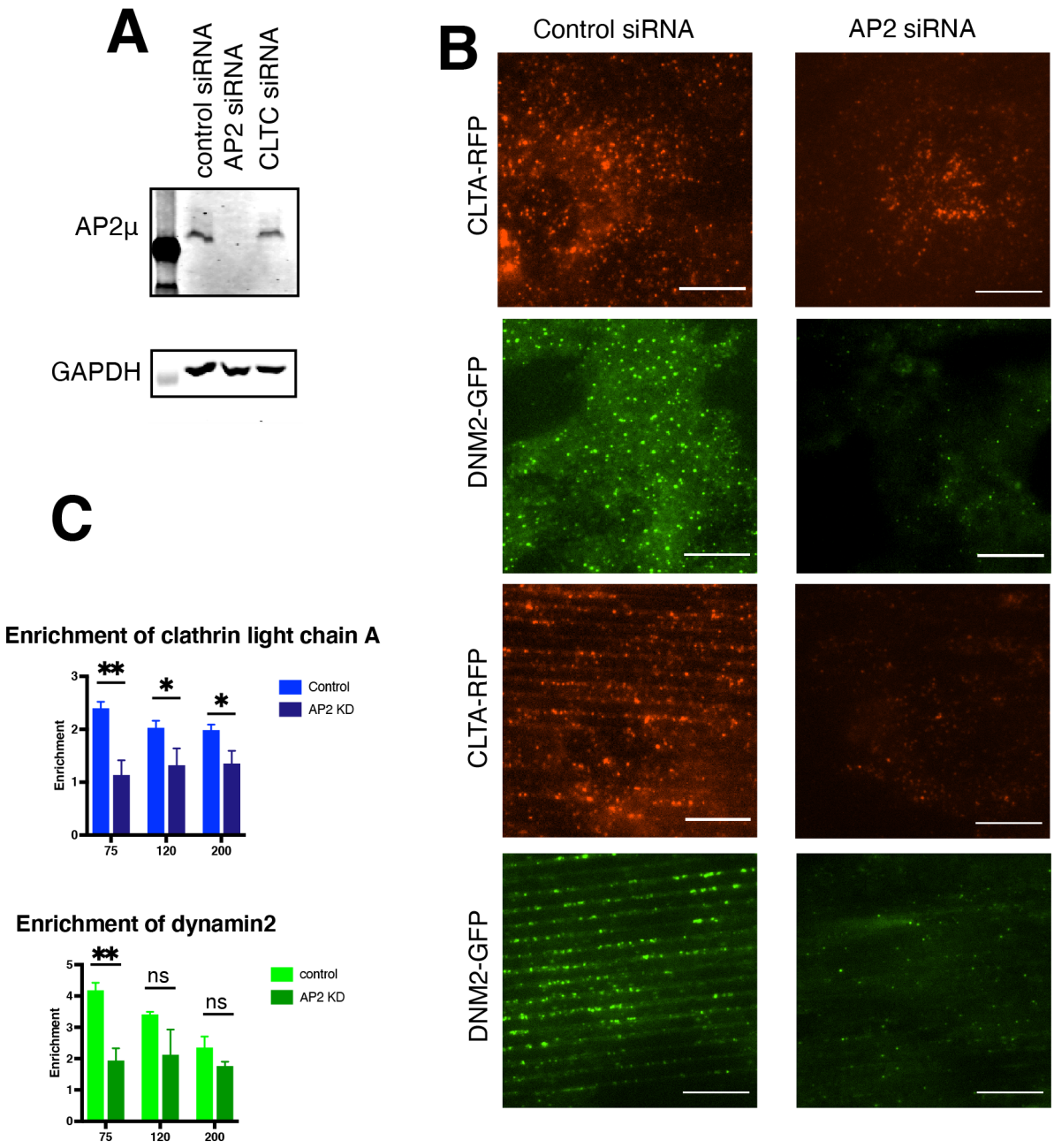

Figure 4.2 AP2 KD is not rescued by curved nanoridges. A) Western blot of AP2u subunit demonstrates a >90% knockdown of AP2. GAPDH is the loading control. B) Representative images of control and AP2-KD cells on flat and 75nm nanoridge substrates, showing a marked decrease in number and intensity of CCPs after AP2 disruption unchanged by curvature. Scale bar 10 microns. C) Enrichment score of CLTA-RFP and DNM2-GFP in response to AP2 knockdown, showing decreased enrichment after AP2 disruption.

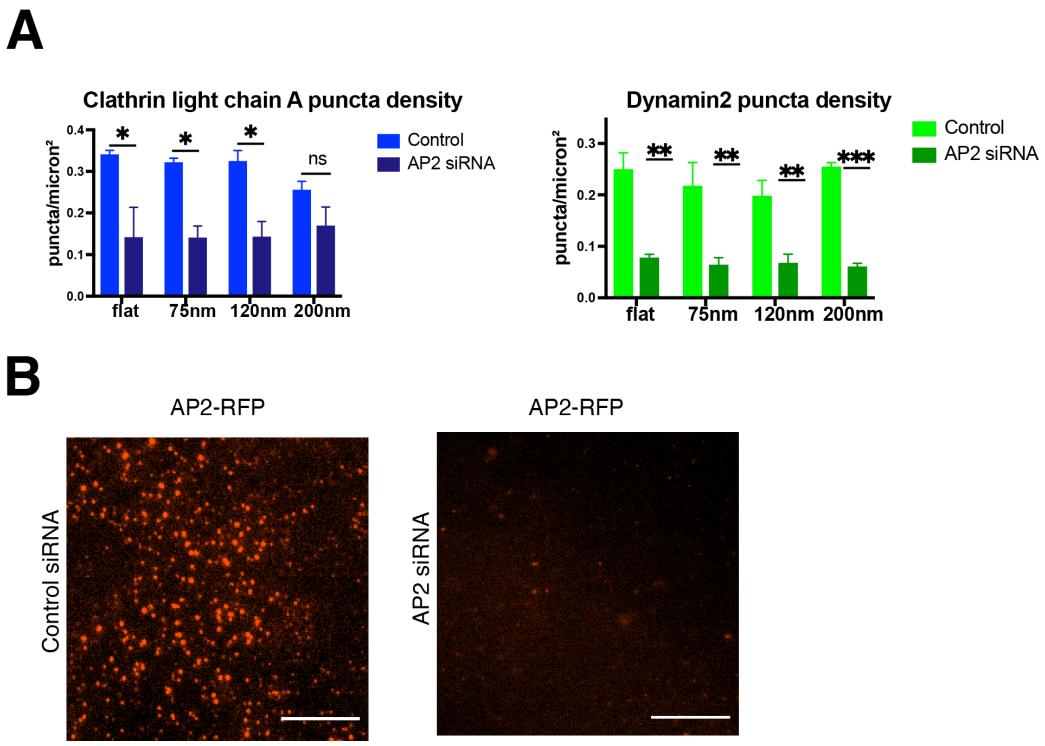

Figure 4.3 Decrease in puncta number and AP2 intensity after AP2 siRNA. A) CLTA-RFP and DNM2-GFP are significantly decreased after AP2 knockdown, and not changed by induced curvature. B) Representative images of AP2-RFP with and without AP2 knockdown, confirming the absence of AP2 puncta after siRNA treatment. Scale bar 10 microns.

unchanged by the presence of nanoridges (Fig 4.4C). DNM2GFP puncta were similarly depleted by >2-fold and unchanged by nanoridges, showing that the defect in endocytic site stabilization could not be rescued by induced curvature. This decrease in puncta number was accompanied by a decrease in lifetime and fluorescence intensity of AP2 tracks over time: the average lifetime of an AP2RFP detection decreased from 40 seconds for control cells to 27 seconds for FCHo1/2 KD cells, and the maximum fluorescence intensity decreased by approximately 75% (Fig 4.4D). These decreases in lifetime and intensity were unchanged by nanoridge size, indicating that stable curvature is insufficient to replace activity provided by the pioneer complex.

Interestingly, of the AP2RFP spots that remained, there was a clear preference for high induced curvature: the enrichment score for 75nm ridges was 2.9 for FCHo1/2 KD cells, compared with 3.7 for control cells (Fig 4.4E). This increased enrichment on curvature persisted across nanoridge sizes, with an enrichment of 2.6 for 120nm and 200nm ridges. This observation indicates that the nucleation stage of CME, in which AP2 molecules bind to cargoes on the membrane, preferentially localizes to sites of high curvature, even when the nascent site fails to become stabilized and progress to CME vesicle formation. This result might reflect intrinsic affinity of AP2 molecules for membranes of high curvature, or it might be the result of clustering of large molecules, creating steric effects that bias association to regions of high membrane curvature (Stachowiak et al., 2012).

DNM2GFP was also enriched on nanoridges, although slightly more modestly than in control

cells: the enrichment score for 75nm ridges was 3, compared with 4.1 for control cells (Fig 4.4F). For 120nm and 200nm ridges, DNM2GFP's enrichment score was approximately 2, indicating a twofold increase in DNM2GFP puncta on these nanoridges. These DNM2GFP puncta frequently do not overlap with noticeable AP2RFP puncta (Fig 4.4B), indicating that they represent other dynamin2-mediated processes on the plasma membrane, such as clathrin-independent endocytosis. In these other roles, dynamin2 may also preferentially bind to curved membrane surfaces, underscoring the importance of nanoscale substrate shape in multiple cell biological processes.

Invagination module: Clathrin heavy chain knockdown is rescued by induced curvature
Clathrin is an essential component of clathrin-mediated endocytosis. Upon clathrin knockdown through siRNA, clathrin expression was reduced by approximately 95% as determined by western blot analysis (Fig 4.5A). Endocytic sites in clathrin-knockdown cells grown on glass or flat Ormocomp substrates are unstable, unproductive protein patches; AP2-RFP puncta are much smaller and approximately 3x lower in intensity than in control cells, with reduced DNM2-GFP colocalization, indicating a defect in CCP formation (Fig 4.5B).

Clathrin knockdown cells on substrates with induced curvature, however, demonstrated a marked increase in the size and fluorescence intensity of AP2-RFP puncta (Fig 4.5B). These AP2-RFP puncta bore a striking overlap with DNM2-GFP as well, indicating that these putative CCPs advance to a later stage of CME, where the scission machinery localizes to the endocytic site. These data were the first we found showing that induced curvature could rescue CCPs from CME protein disruption. We found that enrichment for both AP2 and DNM2 was the same after clathrin siRNA (Fig 4.5D), indicating their preference for curvature is independent of the clathrin coat. Thus, clathrin's essential function in endocytic site formation appears to be in curvature generation rather than nucleation or stabilization. Induced, stable curvature can bypass this role.

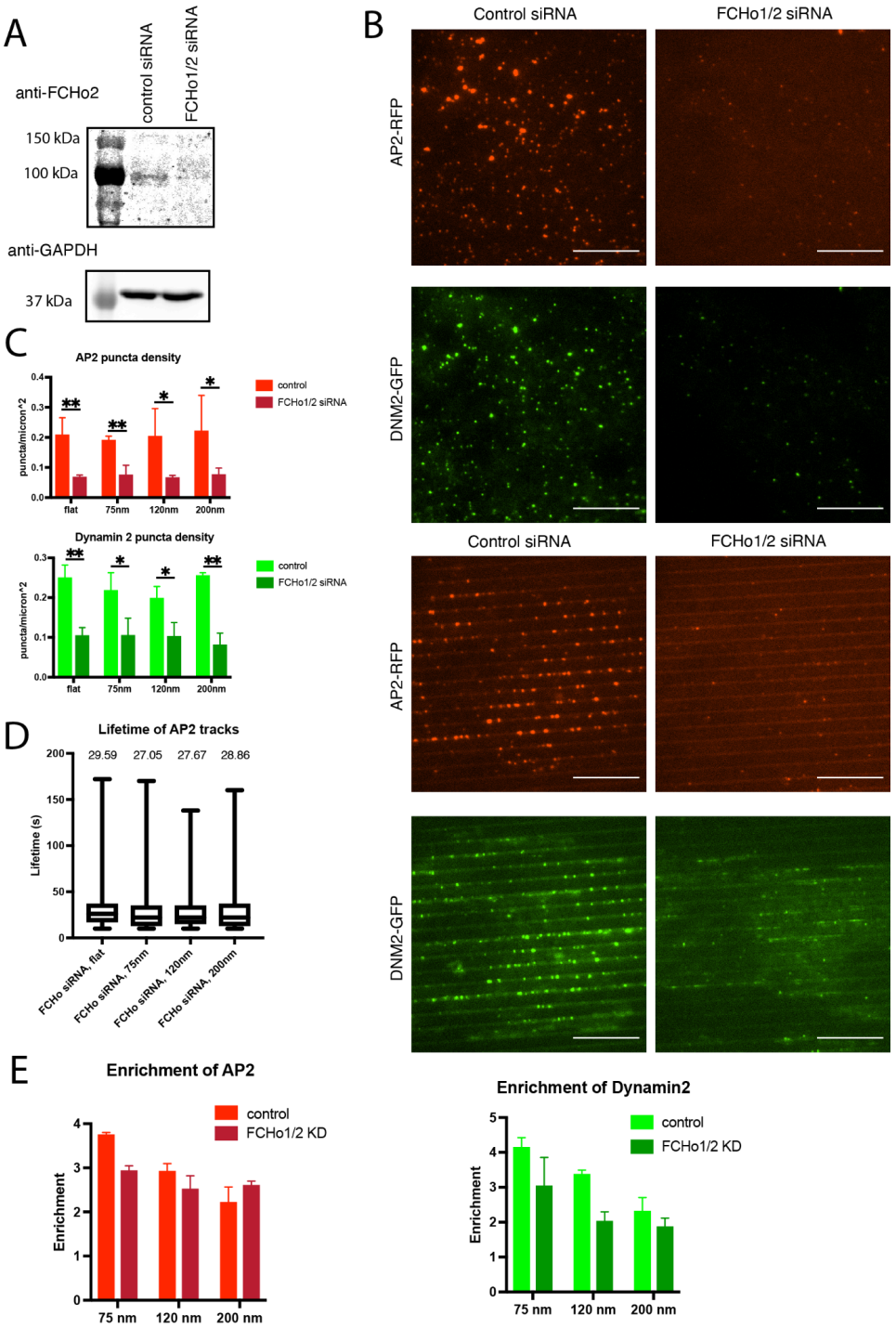

Figure 4.4 Decrease in CCP number and lifetime after FCHo1/2 KD. A) Western blot to FCHo2 indicating decrease in expression. B) Representative images of AP2-RFP/DNM2-GFP with and without FCHo1/2 knockdown, indicating decrease in endocytic sites that is not rescued by curvature. Scale bar 10 microns. C) Quantification of puncta density of AP2-RFP/DNM2-GFP after FCHo1/2 KD. D) Lifetime of AP2-RFP tracks is unchanged by ridge size. E) Enrichment of AP2-RFP and DNM2-GFP on nanoridges after FCHo1/2 KD, indicating both proteins are still enriched after knockdown.

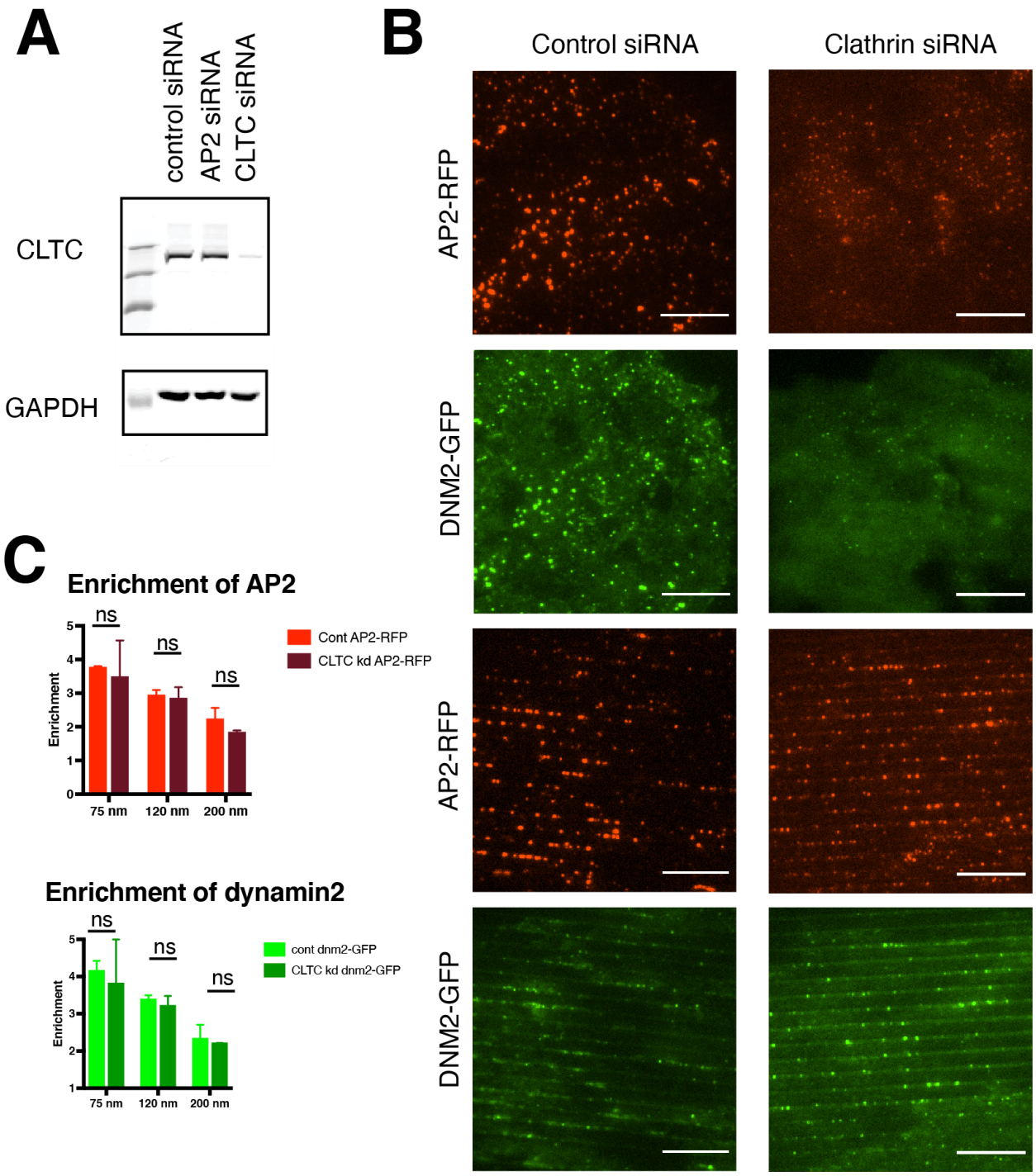

Figure 4.5 Clathrin knockdown is rescued by induced curvature. A) Western blot of clathrin heavy-chain siRNA cells demonstrates ~95% decrease in CLTC expression after siRNA. B) Representative images from flat and 75nm nanoridge cells with control or CLTC siRNA, showing a decrease in number and intensity of AP2-RFP/DNM2-GFP puncta that is rescued by induced curvature. Scale bar 10 microns. C) Enrichment score of AP2-RFP and DNM2-GFP is unchanged by clathrin knockdown.

Curvature-rescued clathrin KD sites are dynamic with longer lifetimes
We next wondered whether these curvature-rescued sites were dynamic, and how their fluorescence intensity profile would compare to those for normal sites. We imaged AP2-RFP/DNM2-GFP cells at 0.5 Hz for 5 minutes with control and clathrin siRNA. After automated tracking, filtering, and binning, we followed the fluorescence intensity of AP2/DNM2 tracks over time. Example montages of AP2/DNM2 tracks over time revealed canonical endocytic dynamics in control cells, while the remaining AP2 tracks in clathrin knockdown cells demonstrate dimmer AP2 spots with decreased DNM2 recruitment, indicating frustrated endocytosis where the spot cannot progress to full invagination (Fig 4.6A). Clathrin knockdown cells with induced curvature, however, demonstrated a marked increase in AP2 fluorescence intensity and DNM2 fluorescence overlap, appearing to be a productive CCP.

We binned all automatically-detected AP2-RFP/DNM2-GFP tracks and normalized the detected fluorescence intensity to untreated cells. Control cells bore the canonical fluorescence profile of valid endocytic sites, with a gradual increase in AP2 fluorescence and a late peak of DNM2 marking scission (Fig 4.6B). The average AP2 lifetime was 50.7s, the same as in untreated cells (Fig 4.6C). For clathrin knockdown cells grown on flat substrates, the fluorescence intensity of AP2-RFP was reduced to only 35% of the fluorescence intensity found in control cells, indicating decreased stability of CCPs, and it did not bear the same gradual increase in intensity over time. The fluorescence intensity of DNM2-GFP was similarly disrupted, with a noisy, almost symmetrical distribution, rather than the late peak typical of productive scission. Thus, clathrin disruption depletes productive endocytic sites on flat substrates.

However, for the curvature-rescued endocytic sites, the fluorescence intensity was rescued to over 70% of that found in control cells, a >2x increase in fluorescence intensity compared to flat clathrin knockdown cells (Fig 4.6B). Additionally, the fluorescence profile followed the canonical signature behavior of a productive endocytic site, with a gradual increase in AP2 fluorescence followed by a late-appearing burst of DNM2 fluorescence. The average lifetime of these sites was significantly longer, at 68s, than in control cells, indicating a persistent defect in CME despite the relatively normal fluorescence intensity and lifetime profiles (Fig 4.6C). This evidence suggests that clathrin's essential function in CME is to stabilize the curvature of the endocytic site, and that in the absence of clathrin, induced stable curvature suffices.

Curvature-rescued CME sites can take up endocytic cargoes
We next sought to determine whether curvature-rescued endocytic sites can take up cargo, indicating that they are truly productive endocytic sites. To assess endocytic cargo uptake we performed an assay using AlexaFluor-647-labeled transferrin (tfn-AF647) as the cargo, because of its constitutive uptake through CME. After serum starvation for 25 minutes and a 2-minute pulse of fluorescent transferrin, followed by a 2-minute chase with fresh media, there were hundreds of puncta of fluorescent transferrin of various sizes detectable in control cells, trafficked into various compartments such as the endosome and lysosome (Fig 4.7A).

After both clathrin or AP2 knockdown, there was a clear disruption of transferrin uptake on flat substrates (Fig 4.7A). In clathrin knockdown cells, the transferrin puncta are much sparser and >10x dimmer, and bear a generally membrane-associated staining, indicative of transferrin binding to its receptor on the surface of the cell but failing to internalize. The puncta come from

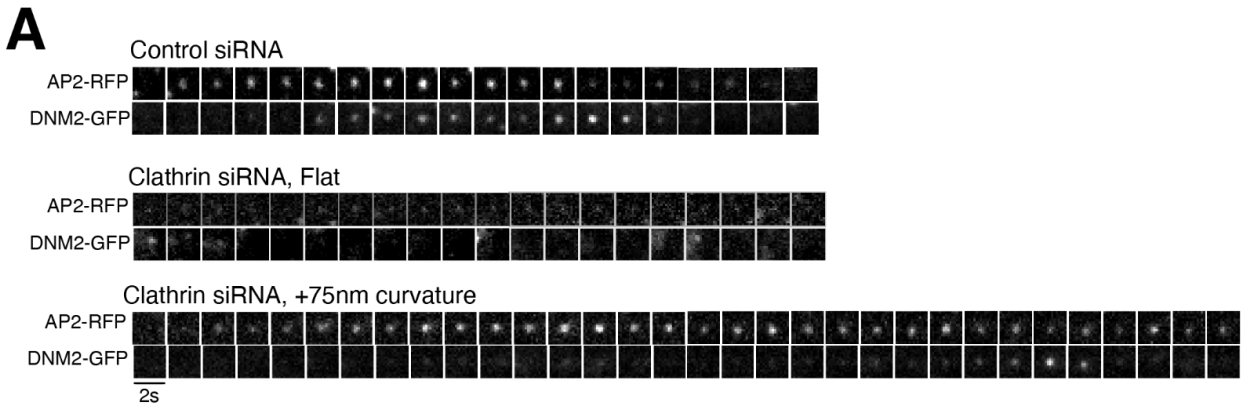
A
Control siRNA
AP2-RFP
DNM2-GFP
Clathrin siRNA, Flat
AP2-RFP
DNM2-GFP
Clathrin siRNA, +75nm curvature
AP2-RFP
DNM2-GFP
2s

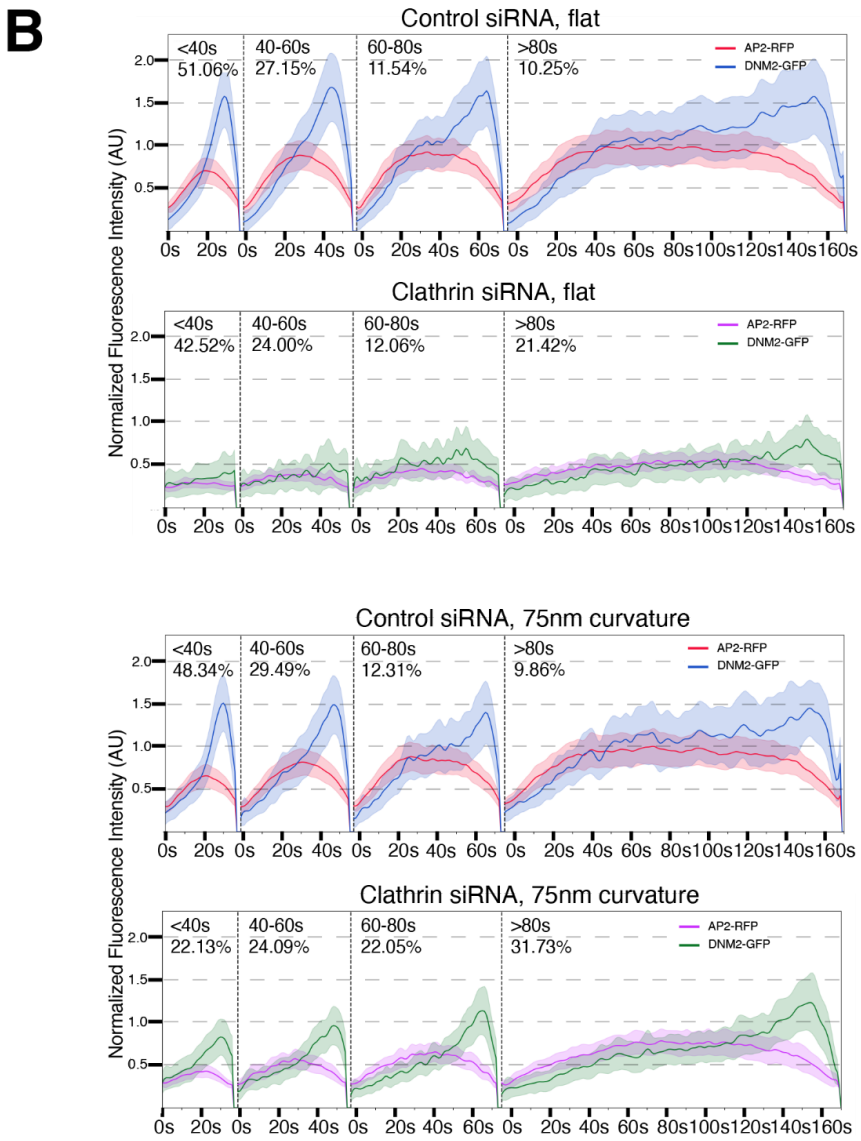
B
Control siRNA, flat
<40s 51.06%
40-60s 27.15%
60-80s 11.54%
>80s 10.25%
AP2-RFP
DNM2-GFP
Normalized Fluorescence Intensity (AU)
Clathrin siRNA, flat
<40s 42.52%
40-60s 24.00%
60-80s 12.06%
>80s 21.42%
Control siRNA, 75nm curvature
<40s 48.34%
40-60s 29.49%
60-80s 12.31%
>80s 9.86%
Clathrin siRNA, 75nm curvature
<40s 22.13%
40-60s 24.09%
60-80s 22.05%
>80s 31.73%
0s 20s 0s 20s 40s 0s 20s 40s 60s 0s 20s 40s 60s 80s100s120s140s160s

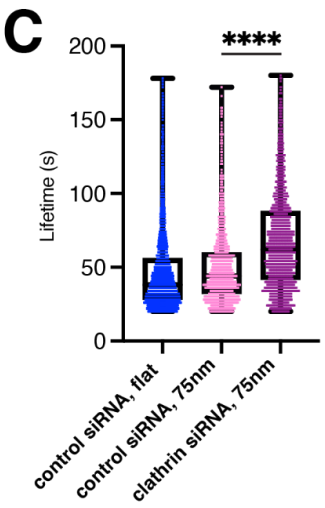
C
****
Lifetime (s)
200
150
100
50
0
control siRNA, flat
control siRNA, 75nm
clathrin siRNA, 75nm

Figure 4.6 Clathrin-knockdown endocytic sites demonstrate canonical endocytic phenotype with longer lifetimes. A) Representative montages from control and CLTC siRNA CCPs with or without induced curvature, showing that with curvature there is a marked rescue of AP2-RFP fluorescence and a typical peak of DNM2-GFP after clathrin knockdown, in the presence of induced curvature. B) Binned, averaged CCPs from control or CLTC knockdown cells with and without curvature, showing the rescue of AP2-RFP fluorescence to ~70% of control cells after clathrin knockdown in the presence of induced curvature. DNM2-GFP peaks are typical of endocytic sites. C) Lifetime of valid CCPs on nanoridges demonstrating the increased lifetime after CLTC knockdown, indicating a defect to endocytosis even with induced curvature after clathrin disruption.

the AP2-dependent concentration of receptors at failed CCPs. However, upon growth of these cells on substrates with curvature, there is a marked increase in the number and intensity of transferrin puncta, and the puncta appear not only on the nanoridges where the induced curvature is present but also in spaces between the ridges, evidence that these puncta may be internalized and trafficked. AP2 knockdown cells demonstrate diffuse membrane staining of tfn-AF647 from the transferrin binding its receptor but failing to cluster; this membrane staining pattern is identical across flat or curved substrates.

To quantify the fluorescent transferrin uptake, we drew regions-of-interest (ROI) around 10 cells per condition and measured the mean intensity of pixels within the ROIs. For control cells, the mean intensity was approximately 1200 AU (Fig 4.7B). Transferrin intensity in clathrin knockdown cells on flat substrates was reduced in mean intensity to 69 AU, while for clathrin knockdown cells on induced curvature, the mean intensity was increased to 250 AU, a >3-fold increase in mean pixel intensity. Although this intensity level represents a dramatic rescue effect, it is still >4-fold lower than the mean intensity in control cells, consistent with 1) Curvature only partially rescuing CME as evident in the increased lifetime of CCPs and 2) only ~⅓ of the cell, the ventral cell membrane, being exposed to induced curvature, while CCPs on the other cell surfaces would still be unproductive upon clathrin knockdown. AP2 knockdown cells showed no difference in transferrin fluorescence intensity as a function of curvature.

To determine whether these puncta marked clusters of proteins on the ventral surface of the cell or trafficked vesicles, we generate X-Z projections of confocal microscopy images after transferrin uptake (Fig 4.8A). Control cells in X-Z have a large number of peri-nuclear transferrin puncta, evidence of trafficking to interior compartments after endocytic uptake. Clathrin knockdown cells, for their part, demonstrate only weak membrane-associated transferrin puncta. Clathrin knockdown cells with induced curvature have membrane-associated transferrin puncta as well as peri-nuclear puncta, indicating that in response to induced curvature the transferrin is not only enriched on the cell surface, but it is also trafficked into the cell.

To determine what curvature-rescued endocytic sites might look like, we prepared clathrin knockdown cells grown on substrates for thin-section TEM. We found examples of elliptical membrane-enclosed structures that appear to be vesicles but lack the canonical spiked coat of clathrin-coated vesicles (Fig 4.8B). These may be vesicles that form in response to induced stable curvature without the stabilization of the clathrin coat as we did not observe such structures in control cells.

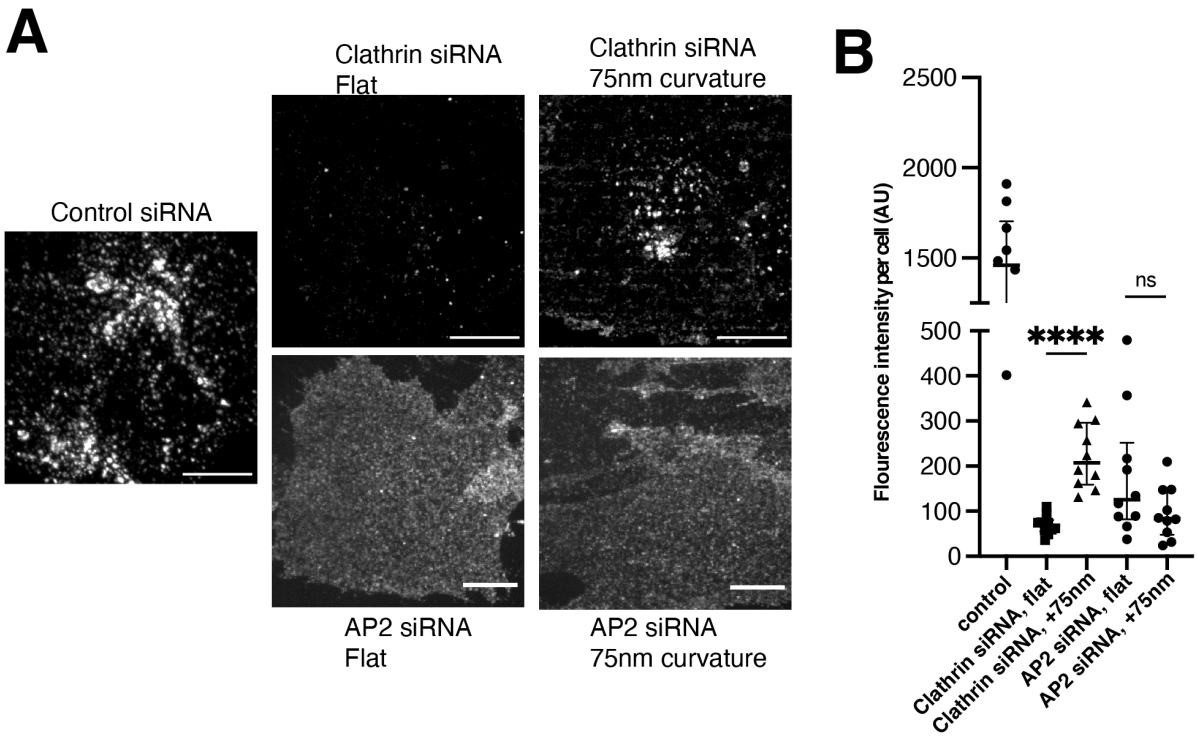

Figure 4.7 Uptake of fluorescent transferrin after clathrin knockdown. A) Representative maximum-intensity micrographs of control, clathrin knockdown, and AP2 knockdown cells with and without induced curvature, showing an increase in fluorescent transferrin with induced curvature after clathrin knockdown, absent after AP2 knockdown. Scale bar 10 microns. B) Quantification of (A).

Conclusions

The decrease in clathrin's enrichment after AP2 knockdown demonstrates that clathrin relies on AP2 and other proteins to stabilize an endocytic site. Interestingly, in MDA-MB-231 cells used in this study, dynamin2 still bore some curvature enrichment after AP2 and FCHo1/2 knockdown, although significantly lower than in control cells, even after these knockdowns eliminated essentially all productive CME sites. This enrichment may be due to some innate curvature preference for dynamin2, or it may be due to dynamin2's roles in other curvature-sensitive endocytic pathways (Schafer et al., 2002; Henley et al., 1998).

Clathrin's role during CME has been a topic of debate since the discovery through electron microscopy some 40 years ago of its heterogeneous conformations on the plasma membrane (Heuser and Evans, 1980). While many CME proteins have been shown to sense curvature on their own in purified systems, clathrin's ability to respond to curvature in vitro depends on its oligomeric assembly into a macromolecular ensemble and is greatly enhanced by other proteins present during CME (Busch et al., 2015; Zeno et al., 2018; Zeno et al., 2021). One proposed model for endocytic curvature formation is that clathrin does not itself generate curvature, but acts as a Brownian ratchet, leveraging subunit exchange as the pit grows to irreversibly stabilize the membrane curvature generated by thermal fluctuations and membrane-bending proteins (Sochacki and Taraska, 2018; Avinoam et al., 2015). Consistent with this model, we find that our artificially induced nanoscale curvature itself is sufficient to produce vesicular uptake in the absence of a clathrin coat. This curvature-induced endocytosis may be relevant to other

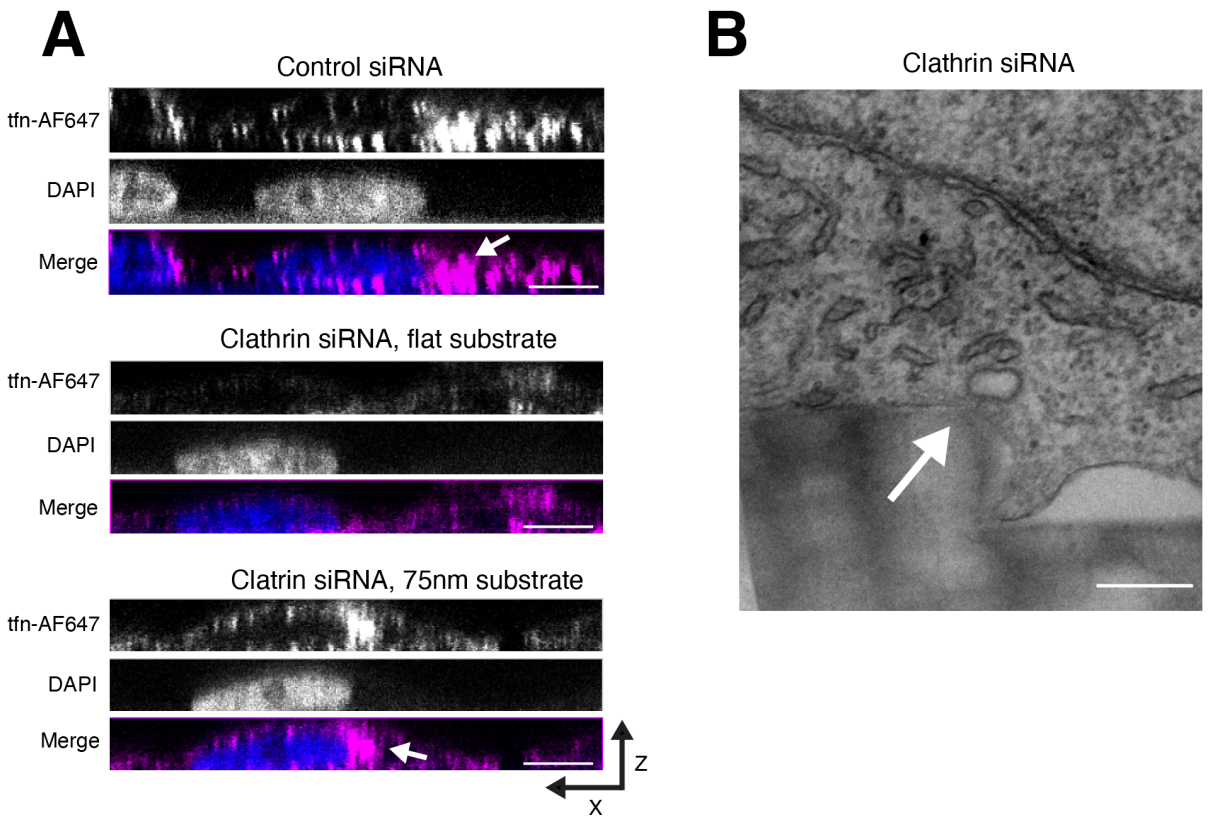

Figure 4.8 Trafficked transferrin after clathrin heavy chain knockdown. A) Representative X-Z projections of control or clathrin knockdown cells after a transferrin uptake assay, demonstrating the presence of perinuclear transferrin after clathrin knockdown when induced curvature is present. Scale bare 10 microns B) Thin-section TEM image of a clathrin knockdown cell on induced curvature, with an elliptical vesicle lacking the spiked coat of clathrin. This may be a clathrin-free CCP, near scission. Scale bar 200 nanometers.

trafficking events such as compensatory endocytosis, where coat proteins might be absent, or in divergent endocytosis such as viral uptake, as viral particles are orders of magnitude stiffer than the human plasma membrane and are often larger than canonical CCP cargoes (Sokac at al., 2003; Mateu, 2012; Ehrlich et al, 2004).

The high-throughput UV-NIL approach described here to nanofabricate substrates from Ormocomp, uniquely enables both precise control of membrane curvature and state-of-the-art imaging. When coupled with quantitative cellular assays, this approach will allow in vivo studies of many other curvature-sensitive proteins so how 3D nano-geometry affects biochemical reaction rates underlying diverse cellular processes can be determined.

Methods

Transfection for siRNA
Dharmacon smartpool siRNAs (L-004001-01-0005, L-008170-00-0005, L-014114-02-0005, L-024508-02-0005, and D-001810-10-05) were used to knockdown Clathrin Heavy Chain, AP2Mu1, or FCHo1/2, or a non-targeting control was used, respectively. Cells were transfected using lipofectamine 3000 according to manufacturer protocols (https://tools.thermofisher.com/content/sfs/manuals/lipofectamine3000_protocol.pdf), using an siRNA final concentration of 20 nM. Cells were incubated for 72 hours post-transfection prior to imaging. 18-24 hours prior to imaging or experiment, cells were split. 50% of cells were seeded on Ormocomp substrates. The remaining cells were re-plated, grown until imaging of Ormocomp substrates, then harvested for western blot analysis to determine knockdown efficiency.

Western blot
Cells were washed on ice in cold DPBS (Gibco 14190-144), lysed on ice using pre-chilled cell scrapers (Corning 3008) in lysis buffer (150 mM NaCl, 1% NP-40, 50mM Tris pH 8.0, 1x Roche protease inhibitor tablet (11697498001)), with immediate addition of 4x Laemmli buffer and 0.5% (v/v) beta-mercaptoethanol. Samples were thoroughly mixed by scraping tubes along a tube rack, boiled for 5 minutes and then centrifuged at 17,900 x g for 5 min before running at 120V on 10% SDS-polyacrylamide gel. Gels were transferred to nitrocellulose membrane (GE Healthcare 10600006) for 90 minutes at 40V in 4-degree transfer buffer (25 mM Tris base, 192 mM glycine, 20% (v/v) methanol), then blocked for 1 hour at room temperature in 5% milk in TBSt (10 mM Tris, 0.09% (w/v) NaCl, 0.05% (v/v) tween-20, pH 7.5). Membranes were probed with clathrin heavy chain antibody (Abcam ab1679) at 1:500 dilution in TBSt with 5% milk, AP2M1 antibody (Abcam ab75995) at 1:1000 dilution in TBSt with 5% milk, FCHo1 antibody (ab272640) at 1:500 dilution in TBSt with 5% milk, FCHo2 antibody (ab122407) at 1:500 dilution in TBSt with 5% milk, or GAPDH antibody (Abcam ab9485) at 1:2000 dilution in TBSt, all for 1 hour at room temperature, followed by 4 x 10-minute wash in TBSt. Secondary antibodies (LICOR, 926-32213) were blotted at 1:2500 dilution in TBSt for 1 hour at room temperature, followed by 4 x 10-minute wash in TBSt and immediate imaging on LICOR Odyssey CLx.

TIRF microscopy was performed as described in Chapter 3.
Transferrin uptake assays were performed as described in Chapter 3.
Confocal microscopy for control siRNA, CLTC knockdown, and FCHo1/2 knockdown cells was done using a Zeiss LSM 900 with Airyscan 2.0 detection, in 4Y multiplex mode, operated by ZEN Blue software. Entire cell volumes were collected at Nyquist sampling frequency (140 nm per Z-section), and maximum intensity projections were created in ImageJ for analysis. Images were batch-processed by ZEN Blue software for Airyscan reconstructions using filter strength setting of 6.

Confocal microscopy for AP2 knockdown cells and for no-treatment transferrin uptake assays was done using a Nikon Eclipse Ti microscope with Yokogawa spinning disk and Andor EMCCD, operated by Nikon Elements software. Entire cell volumes were collected at Nyquist sampling frequency (200nm per Z-section), and maximum intensity projections were created in ImageJ for analysis.

Statistical analyses were conducted either with python packages NumPy, Pandas, SciPy, and Seaborns, or with Prism 9. Graphs were produced with Prism 9.

Chapter 5
Future directions

When I first started working on nanofabrication and its use for studying CME, it was known that nanoscale membrane curvature recruited endocytic proteins (Zhao et al., 2017). However, the complexity of quartz nanofabrication employed in the initial study limited our ability to gain mechanistic insights into CME with stably induced curvature. For instance, which stage(s) of endocytosis have an attraction for curved membranes was not known, nor was how curvature could compensate for protein knockdowns. Within chapters 2-4, I explained how to induce plasma membrane curvature in live cells through UV-NIL, how this curvature affects normal endocytic kinetics, and how it can rescue CME from a clathrin knockdown but not other disruptions. We now have a (relatively) simple and high-throughput method for inducing precise plasma membrane shapes in various cell types, and we have an ever-growing assortment of fluorescently-tagged endocytic proteins with which to study CME. Many outstanding questions remain about curvature generation during endocytosis and beyond, but the tools now exist to answer these questions. In this chapter, I will expand upon some of the interesting remaining topics, including ideas about technique development that could open the door to answering more questions.

Outstanding questions about Ormocomp substrates

First off, while Ormocomp substrates are a fantastic tool for inducing plasma membrane curvature and for watching live cells on a fluorescence microscope, some relatively straightforward further work could improve their utility and answer some important cell biological questions. Fuller characterization of the optical response to substrates would benefit us immensely, allowing much more precise and consistent TIRF illumination. Physical modeling through programs like COMSOL could calculate the shape of an evanescent field as a function of polar and azimuthal angles, which could provide important information about how to align the TIRF microscope prior to imaging (Wang et al., 2011). Some simple engineering changes to the microscope stage and to slides with Ormocomp nanopatterning, allowing for better control of the position of the pattern, could standardize the azimuthal angle prior to any experiments. Further optimization of substrate manufacturing, for instance through better control of glass coating with HMDS and controlling the alignment of glass coverslip with the silicon wafer, could improve the quality of Ormocomp substrates and ensure that substrate quality is not the breaking point for experiments. These changes to substrate manufacturing and use in imaging could allow for single-molecule imaging, super-resolution microscopy, molecular counting for CCPs on substrates, and better comparisons of fluorescence intensity across samples.

Ormocomp is well-suited to normal microscopy methods, but the specifics of CME protein localization and structure are below the diffraction limit. Thus, we do not know precise localizations of the endocytic proteins on nanoridges or the structure of the clathrin triskelia, important factors in productive vesicle formation. Three-dimensional super-resolution microscopy has been applied to nanofabricated quartz substrates with an implementation of SMLM microscopy that is available off-the-shelf (Roy et al., 2021). After some calibration by imaging bare Ormocomp substrates and fluorescent membrane tags in cells grown on nanoridges, I think it would be straightforward to do d-STORM imaging, perhaps even multi-color imaging, to visualize endocytic pits on nanoridges. This would make possible precise

visualization of the position of clathrin triskelia atop the ridges to determine if the endocytic sites typically bind tightly to the substrate in a cylindrical shape or are raised from the substrate, forming spherical vesicles. This analysis may also provide insights into dynamin2's localization on nanoridges. The transition from U-shaped membrane, conforming to the nanoridge shape, to Ω-shaped vesicles prior to scission confounds me: can we localize dynamin2 below clathrin on the ridge through super-resolution imaging? Might dynamin2 preferentially localize to one side of a CCP on a nanoridge at early stages?

I've also been curious about how the actin cytoskeleton responds to nanoridges: does it localize preferentially to certain ridge sizes? Does actin on a nanoridge look similar to actin filaments that align with ECM fibers (Wu and Dedhar, 2001)? Do the nanoridges change the fluorescence recovery after photobleaching of actin markers? Platinum-replica EM studies could also give us insight into what endocytic sites look like on nanoridges, overcoming the current bottleneck for our attempted EM studies, which is to get this method to work upon detaching the Ormocomp from the platinum replica (Rohr et al., 2018). I have been wondering for years about the shape of clathrin lattices on nanoridges, and I think this is the method to tell us.

Questions concerning CCP characteristics and disruptions to CME

Related to the questions above, there are additional outstanding questions about CCP formation on induced membrane curvature, and the relationship between CME on stably induced curvature on flat surfaces. Answering these questions will require more complex experimental manipulations like knockdowns and chemical inhibition. For instance, is there an active mechanism for CCP dissociation from the nanoridge prior to scission, or is the membrane weakly attached to the substrate? Does the dissociation depend on actin polymerization/Hip1R binding, similar to CCPs in high-tension conditions, or endocytosis of large cargoes (Engqvist-Goldstein et al., 2001; Cureton et al., 2009)? These questions could be answered with precise manipulations of the actin cytoskeleton, made possible through pharmacological inhibitors like latrunculin-A, along with siRNA knockdown of actin-binding proteins like Hip1R at CCPs. But another avenue to answer this question, one that I'm pretty excited about, is using mathematical modeling to study the membrane transition from induced U-shape on the nanoridge to a spherical vesicle (Hassinger et al., 2017; Mahapatra et al., 2011). The physical parameters to achieve flat-to-curved transition are solved, so understanding the energetics to create a vesicle from a curved ridge is a matter of solving the same equations for a different starting shape (accounting for the adhesion strength of the membrane for U-shaped nanoridges).

Many different proteins have been proposed to generate curvature during endocytosis. Important examples include epsin, BAR domain proteins, and Hip1R (Ford et al., 2001; Ayton et al., 2009; Engqvist-Goldstein et al., 2001). There is also debate about the role of the actin machinery in generating curvature: is it necessary in generating the initial curved pit, or does it act after curvature has been established by coat proteins (Yarar et al., 2005; Akamatsu et al., 2020)? Evidence for the role of these proteins in generating curvature comes mostly from measuring the shape created by purified proteins or by interfering with the protein in cells and conducting thin-section TEM to measure the proportion of shallow CCPs. These approaches depend on indirect inferences of the protein's role. However, with nanoridges, we can test whether these proteins become dispensable on induced curvature like clathrin heavy chain does. A knockdown screen of the proposed curvature-generating proteins for cells grown on nanoridges would test

whether their essential role is curvature generation. The effects of knockdowns of CME proteins are often subtle, with phenotypes such as an increased lifetime of endocytic sites or a reduction in dynamin2 recruitment. But since we carefully characterized normal endocytosis on nanoridges, subtle effects are expected to be detectable through our analysis pipeline. A protein like amphiphysin might be dispensable as a result of substrate-induced membrane curvature, whereas an enzyme like synaptojanin might still be essential. Since these are just hypotheses I think that it would be really exciting to identify cases in which the expectation is wrong, and a protein is important for more than just curvature generation. Dissecting the role of the actin machinery could be more complicated: actin is thought to be more important in cases of high membrane tension, and, because Ormocomp is ~50x softer than borosilicate glass, the tension of cell membranes on nanoridges is expected to be lower than on glass (Schizas and Karalekas, 2011). Thus, there may be no detectable difference in endocytic rates through inhibition of branched actin polymerization with CK666, even though such an effect is visible in cells grown on glass. It may be necessary to elevate the membrane tension of the Ormocomp-grown cells using hypo-osmotic shock to induce dependence on actin polymerization (Boulant et al., 2011). A combination of hypo-osmotic shock and CK666 treatment may reveal whether actin polymerization is essential for generating membrane curvature in high-tension contexts, which would be rescued by nanoridges.

The clathrin knockdown rescue by induced membrane curvature seems almost complete: localization of early and late endocytic proteins is rescued, and the fluorescence profile of normal endocytic sites is restored, intensity of endocytosed fluorescent transferrin puncta is restored. We even found what appears to be a vesicle around the moment of scission, without the clathrin coat present. However, this is not conclusive proof of clathrin-free endocytic vesicles. It would be relatively easy to apply correlative light and electron microscopy (CLEM) that combines the fluorescence localization of transferrin puncta in clathrin-knockdown cells with thin-section TEM to find vesicles that have transferrin but lack clathrin.

In vitro generation of supported lipid bilayers on curved substrates can answer novel questions in biophysics

In addition to the methods I've already talked about with cultured cells, I think that reconstituting lipid membranes as supported bilayers Ormocomp substrates would open up a huge range of experimental possibilities to probe questions in membrane biophysics or even structural biology. The typical method to create lipid bilayers on substrates *in vitro* consists of the supported lipid bilayer (SLB), in which small unilamellar vesicles of the desired lipid content are dispersed atop glass slides or beads, and the vesicles undergo spontaneous lysis to form a continuous single bilayer (Lee et al., 2015). Usually, glass is cleaned with piranha etching to create a sufficiently clean and hydrophilic surface, but piranha etching destroys the organic crosslinking of Ormocomp, degrading the substrates. However, there are other methods to make surfaces sufficiently clean and hydrophilic, including Hellmanex detergent washes, plasma cleaning, UV-Ozone etching, and others (Shahal et al., 2008). These methods have been deployed in combination with soft lithography techniques like polydimethylsiloxane (PDMS) deposition, and because both Ormocomp and PDMS are based on siloxane polymers, I am hopeful that one of these techniques could work.

However, if SLB deposition turns out to not be possible, we have already established a method to unroof live cells on Ormocomp nanoridges, and this method leaves the basal cell membrane behind along with many endocytic proteins. This technique has already been leveraged by other labs to create a semi-*in vitro* system to study endocytic complex formation with both purified proteins and whole cell lysates (Chen et al., 2019). Unroofing live cells reduces the chemical control that we have over membrane composition, and it leaves behind many other proteins from the cell independent of endocytosis. I think that this is nevertheless a promising method to create a fairly uniform cell membrane with induced curvature. Atop the unroofed membrane, cell lysates or purified proteins could be added, and the interplay between curvature and binding rate or enzymatic activity could be measured. This approach could even be extended for use in negative-stain or cryo-electron microscopy studies to see conformational changes in proteins in response to induced membrane shape, giving insights into biophysical mechanisms of membrane remodelling by protein binding, although it may take a year of another graduate student's life to get nanofabrication to be compatible with electron microscopy grids.

All of this is leading up to questions about endocytic protein activity that I've long been curious about:

1) AP2. AP2 is strongly enriched on nanoridges, even when FCHo1/2 are knocked down so the endocytic site can't proceed to maturation/scission. What is its mechanism of sensing curvature--does a single AP2 complex preferentially bind to to curved membranes, indicating innate sensitivity, or does its curvature preference depend on cargo binding, oligomerization, steric pressure, or some other multi-subunit mechanism?

2) Epsin. Epsin is one of the proteins with the strongest enrichment on nanoridges that we have found. Epsin is also known to bind to PIP_2 (Ford et al., 2002). Does PIP_2 have a natural affinity for curvature that brings epsin along with it? Or does epsin cluster PIP_2 at sites of high curvature? Or is epsin's affinity for curved membranes independent of PIP_2? Any of these mechanisms could provide insights into what epsin is doing at a growing CCP.

3) Synaptojanin. Earlier work using liposomes of known size indicated that endophilin, a binding partner of synaptojanin, has intrinsic curvature affinity which enhances synaptojanin's activity on high-curvature membranes (Chang-Ileto et al., 2011). I think there might be a difference in the actual rate constant of synaptojanin's phosphatase activity as a function of curvature, and we could directly visualize both the binding and enzymatic activity with fluorescently-labeled PIP molecules and synaptojanin on flat-vs-curved membranes to figure out if the curvature-enhancement of synaptojanin is intrinsic to the enzyme itself or depends on other curvature-sensing proteins. This may point to a general control mechanism, in which scaffolding of structural proteins is the key modulating factor for controlling enzyme activity at shaped membranes, or it may point to cooperativity between the scaffolds and the enzymes. In either case, I think it would be very interesting.

All of these problems would require some novel substrate manufacturing/treatments, and so there is a bit more background work necessary for these experiments. However, I think there is also untapped potential in looking at other processes in cells that might respond to substrate shape.

Other curvature-dependent processes on substrates

While CME is a very robust curvature-sensing process, there are many other normal biological processes that involve reshaping the membrane to generate all sorts of curved shapes across scales. Ormocomp substrate manufacturing could be very useful in screening other major cellular processes to see how their localization and rates are affected by membrane shape. I have long wanted to screen the Allen Institute for Cell Science's genome-edited iPSCs to determine how curvature affects the structures and organelles that they have fluorescently tagged. This would require differentiating the stem cells into fibroblast-like cells, as iPSCs do not grow on nanoridges, but I think there are many cases where we could expect to see something interesting:

1) Paxillin. Do focal adhesions respond to curvature, with a preference for ridges of a particular size? Does curvature affect any of the already defined parameters of focal adhesion activity, like their turnover or their ability to produce traction force? This could help explain migratory behavior of cells in the context of ECM shapes that cells encounter within the body.

2) Myosin2B. Does non-muscle myosin2 respond to curvature? Is there an increase or decrease in contractile actin bundles in response to membrane shape? Previous studies have examined how size and connectivity of substrate/ECM affects cell contractility, but I think nanoscale shape may play a role, too (Ng et al., 2012).

3) LaminB. How does the nucleus change when the cell membrane is exposed to nanofabricated ridges? Is there a threshold for size of nanofabricated shape below which the nucleus is unchanged by nanofabrication?

4) Question 3 gets at a general question I have, which is whether there is a smallest definable feature size that the cell responds to, i.e., does the cell even notice a ridge that is 25nm across and 25nm tall? Or is the tension of the cell membrane sufficiently high that such a feature does not induce shape change? This question could be addressed with imaging of the Caax-box membrane label edited into the genomic safe harbor.

A related but slightly more complicated question that I've wondered about is whether and how the cell changes its tension in response to the nanoridges. I think the membrane tension of Ormocomp-grown cells is lower than that of glass-grown cells because Ormocomp is so much more pliable than glass. But does the existence of stable shapes alter the mechanical properties of the membrane? In general, cells grown on nanoridges are elongated, growing almost parallel to the ridges. Does this general shape change have an accompanying membrane tension change? And does this potential tension change appear to be a function of ridge size, placement, etc? If this is the case, then nanofabricated Ormocomp substrates could be very useful in elucidating biomechanical aspects of cell motility, wherein the physical context and not the chemical

makeup of the cellular environment gives cues to grow, divide, and migrate--all the essential components of being a living cell.

References

Aguet, F., C.N. Antonescu, M. Mettlen, S.L. Schmid, and G. Danuser. 2013. Advances in analysis of low signal-to-noise images link dynamin and AP2 to the functions of an endocytic checkpoint. Dev. Cell. 26:279–291. doi:10.1016/j.devcel.2013.06.019.

Ahyayauch, H., Villar, A. V., Alonso, A., & Goni, F. M. 2005. Modulation of PI-specific phospholipase C by membrane curvature and molecular order. Biochemistry, 44(34), 11592-11600.

Aimon, S., Callan-Jones, A., Berthaud, A., Pinot, M., Toombes, G. E., & Bassereau, P. (2014). Membrane shape modulates transmembrane protein distribution. Developmental cell, 28(2), 212-218.

Akamatsu, M., Vasan, R., Serwas, D., Ferrin, M.A., Rangamani, P. and Drubin, D.G., 2020. Principles of self-organization and load adaptation by the actin cytoskeleton during clathrin-mediated endocytosis. Elife, 9, p.e49840.

Anitei, M., Stange, C., Czupalla, C., Niehage, C., Schuhmann, K., Sala, P., Czogalla, A., Pursche, T., Coskun, Ü., Shevchenko, A. and Hoflack, B., 2017. Spatiotemporal control of lipid conversion, actin-based mechanical forces, and curvature sensors during clathrin/AP-1-coated vesicle biogenesis. Cell reports, 20(9), pp.2087-2099.

Antonny, B. 2011. Mechanisms of membrane curvature sensing. Annual review of biochemistry, 80, 101-123.

Ayton, G. S., Lyman, E., Krishna, V., Swenson, R. D., Mim, C., Unger, V. M., & Voth, G. A. (2009). New insights into BAR domain-induced membrane remodeling. Biophysical journal, 97(6), 1616-1625.

Bacia, K., Futai, E., Prinz, S., Meister, A., Daum, S., Glatte, D., Briggs, J.A. and Schekman, R., 2011. Multibudded tubules formed by COPII on artificial liposomes. Scientific reports, 1(1), pp.1-6.

Baumgart, T., Capraro, B. R., Zhu, C., & Das, S. L. 2011. Thermodynamics and mechanics of membrane curvature generation and sensing by proteins and lipids. Annual review of physical chemistry, 62, 483-506.

Baumgart, T., Hammond, A. T., Sengupta, P., Hess, S. T., Holowka, D. A., Baird, B. A., & Webb, W. W. 2007. Large-scale fluid/fluid phase separation of proteins and lipids in giant plasma membrane vesicles. Proceedings of the National Academy of Sciences, 104(9), 3165-3170.

Bender, M., M. Otto, B. Hadam, B. Spangenberg, and H. Kurz. 2002. Multiple imprinting in UV-based nanoimprint lithography: Related material issues. In Microelectronic Engineering. Elsevier. 407–413.

Bigay, J., Gounon, P., Robineau, S. and Antonny, B., 2003. Lipid packing sensed by ArfGAP1 couples COPI coat disassembly to membrane bilayer curvature. Nature, 426(6966), pp.563-566.

Biswas, A., I. S. Bayer, A. S. Biris, T. Wang, E. Dervishi, and F. Faupel. 2012. Advances in top–down and bottom–up surface nanofabrication: Techniques, applications & future prospects. Advances in colloid and interface science, 170(1-2), 2-27.

Blood, P. D., & Voth, G. A. 2006. Direct observation of Bin/amphiphysin/Rvs (BAR) domain-induced membrane curvature by means of molecular dynamics simulations. Proceedings of the National Academy of Sciences, 103(41), 15068-15072.

Bozelli, J. C., Jennings, W., Black, S., Hou, Y. H., Lameire, D., Chatha, P., Kimura, T., Berno, B., Khondker, A., Rheinstadter, M.C., and Epand, R. M. 2018. Membrane curvature allosterically regulates the phosphatidylinositol cycle, controlling its rate and acyl-chain composition of its lipid intermediates. Journal of Biological Chemistry, 293(46), 17780-17791.

Bratton, B. P., Shaevitz, J. W., Gitai, Z., & Morgenstein, R. M. (2018). MreB polymers and curvature localization are enhanced by RodZ and predict E. coli's cylindrical uniformity. Nature communications, 9(1), 1-11.

Bridges, A. A., Jentzsch, M. S., Oakes, P. W., Occhipinti, P., & Gladfelter, A. S. 2016. Micron-scale plasma membrane curvature is recognized by the septin cytoskeleton. Journal of Cell Biology, 213(1), 23-32.

Broers, A. N., Hoole, A. C. F., & Ryan, J. M. 1996. Electron beam lithography—Resolution limits. Microelectronic Engineering, 32(1-4), 131-142.

Bucher, D., Frey, F., Sochacki, K.A., Kummer, S., Bergeest, J.P., Godinez, W.J., Kräusslich, H.G., Rohr, K., Taraska, J.W., Schwarz, U.S. and Boulant, S., 2018. Clathrin-adaptor ratio and membrane tension regulate the flat-to-curved transition of the clathrin coat during endocytosis. Nature communications, 9(1), pp.1-13.

Busch, D. J., Houser, J. R., Hayden, C. C., Sherman, M. B., Lafer, E. M., & Stachowiak, J. C. 2015. Intrinsically disordered proteins drive membrane curvature. Nature communications, 6(1), 1-11.

Byun, M., Lee, D., Kim, M., Kim, Y., Kim, K., Ok, J. G., Rho, R. & Lee, H. 2017. Demonstration of nanoimprinted hyperlens array for high-throughput sub-diffraction imaging. Scientific reports, 7(1), 1-11.

Cannon, K. S., Woods, B. L., Crutchley, J. M., & Gladfelter, A. S. 2019. An amphipathic helix enables septins to sense micrometer-scale membrane curvature. Journal of Cell Biology, 218(4), 1128-1137.

Casal, E., Federici, L., Zhang, W., Fernandez-Recio, J., Priego, E.M., Miguel, R.N., DuHadaway, J.B., Prendergast, G.C., Luisi, B.F. and Laue, E.D., 2006. The crystal structure of the BAR

domain from human Bin1/amphiphysin II and its implications for molecular recognition. Biochemistry, 45(43), pp.12917-12928.

Cavallini, M., Facchini, M., Massi, M., & Biscarini, F. 2004. Bottom–up nanofabrication of materials for organic electronics. Synthetic metals, 146(3), 283-286.

Chang-Ileto, B., Frere, S.G., Chan, R.B., Voronov, S.V., Roux, A. and Di Paolo, G., 2011. Synaptojanin 1-mediated PI (4, 5) P2 hydrolysis is modulated by membrane curvature and facilitates membrane fission. Developmental cell, 20(2), pp.206-218.

Chen, C.S., M. Mrksich, S. Huang, G.M. Whitesides, and D.E. Ingber. 1997. Geometric control of cell life and death. Science (80-.). 276:1425–1428. doi:10.1126/science.276.5317.1425.

Chen, Y., Yong, J., Martínez-Sánchez, A., Yang, Y., Wu, Y., De Camilli, P., Fernández-Busnadiego, R. and Wu, M., 2019. Dynamic instability of clathrin assembly provides proofreading control for endocytosis. Journal of Cell Biology, 218(10), pp.3200-3211.

Cocucci, E., Aguet, F., Boulant, S. and Kirchhausen, T., 2012. The first five seconds in the life of a clathrin-coated pit. Cell, 150(3), pp.495-507.

Courtland, R. 2016. Transistors could stop shrinking in 2021. IEEE Spectrum, 53(9), 9-11.

Cui, Z. 2008. Nanofabrication. Course notes, ECE, 730.

Cureton, D.K., Massol, R.H., Saffarian, S., Kirchhausen, T.L. and Whelan, S.P., 2009. Vesicular stomatitis virus enters cells through vesicles incompletely coated with clathrin that depend upon actin for internalization. PLoS pathogens, 5(4), p.e1000394.

Daboussi, L., G. Costaguta, and G.S. Payne. 2012. Phosphoinositide-mediated clathrin adaptor progression at the trans-Golgi network. Nat. Publ. Gr. 14. doi:10.1038/ncb2427.

Dannhauser, P.N. and Ungewickell, E.J., 2012. Reconstitution of clathrin-coated bud and vesicle formation with minimal components. Nature cell biology, 14(6), pp.634-639.

Dar, S., Kamerkar, S. C., & Pucadyil, T. J. 2017. Use of the supported membrane tube assay system for real-time analysis of membrane fission reactions. Nature protocols, 12(2), 390-400.

Daste, F., Walrant, A., Holst, M.R., Gadsby, J.R., Mason, J., Lee, J.E., Brook, D., Mettlen, M., Larsson, E., Lee, S.F. and Lundmark, R., 2017. Control of actin polymerization via the coincidence of phosphoinositides and high membrane curvature. Journal of Cell Biology, 216(11), pp.3745-3765.

Daumke, O., Lundmark, R., Vallis, Y., Martens, S., Butler, P.J.G. and McMahon, H.T., 2007. Architectural and mechanistic insights into an EHD ATPase involved in membrane remodelling. Nature, 449(7164), pp.923-927.

Dawson, J.C., Legg, J.A. and Machesky, L.M., 2006. Bar domain proteins: a role in tubulation, scission and actin assembly in clathrin-mediated endocytosis. Trends in cell biology, 16(10), pp.493-498.

den Otter, W.K. and Briels, W.J., 2011. The generation of curved clathrin coats from flat plaques. Traffic, 12(10), pp.1407-1416.

Dhara, M., Martinez, M. M., Makke, M., Schwarz, Y., Mohrmann, R., & Bruns, D. 2020. Synergistic actions of v-SNARE transmembrane domains and membrane-curvature modifying lipids in neurotransmitter release. Elife, 9, e55152.

Doyon, J.B., Zeitler, B., Cheng, J., Cheng, A.T., Cherone, J.M., Santiago, Y., Lee, A.H., Vo, T.D., Doyon, Y., Miller, J.C. and Paschon, D.E., 2011. Rapid and efficient clathrin-mediated endocytosis revealed in genome-edited mammalian cells. Nature cell biology, 13(3), pp.331-337.

Drin, G., Casella, J.F., Gautier, R., Boehmer, T., Schwartz, T.U. and Antonny, B., 2007. A general amphipathic α-helical motif for sensing membrane curvature. Nature structural & molecular biology, 14(2), pp.138-146.

Elkhatib, N., E. Bresteau, F. Baschieri, A.L. Rioja, G. Van Niel, S. Vassilopoulos, and G. Montagnac. Tubular clathrin/AP-2 lattices pinch collagen fibers to support 3D cell migration. doi:10.1126/science.aal4713.

Elmer-Dixon, M.M., Xie, Z., Alverson, J.B., Priestley, N.D. and Bowler, B.E., 2020. Curvature-dependent binding of cytochrome c to cardiolipin. Journal of the American Chemical Society, 142(46), pp.19532-19539.

Elowitz, M.B., Levine, A.J., Siggia, E.D. and Swain, P.S., 2002. Stochastic gene expression in a single cell. Science, 297(5584), pp.1183-1186.

Engler, A.J., S. Sen, H.L. Sweeney, and D.E. Discher. 2006. Matrix Elasticity Directs Stem Cell Lineage Specification. Cell. 126:677–689. doi:10.1016/j.cell.2006.06.044.

Engqvist-Goldstein, A.E., Warren, R.A., Kessels, M.M., Keen, J.H., Heuser, J. and Drubin, D.G., 2001. The actin-binding protein Hip1R associates with clathrin during early stages of endocytosis and promotes clathrin assembly in vitro. The Journal of cell biology, 154(6), pp.1209-1224.

Faix, J., & Rottner, K. (2006). The making of filopodia. Current opinion in cell biology, 18(1), 18-25.

Fan, W., Nassiri, A. and Zhong, Q., 2011. Autophagosome targeting and membrane curvature sensing by Barkor/Atg14(L). Proceedings of the National Academy of Sciences, 108(19), pp.7769-7774.

Farsad, K., Ringstad, N., Takei, K., Floyd, S.R., Rose, K. and De Camilli, P., 2001. Generation of high curvature membranes mediated by direct endophilin bilayer interactions. Journal of Cell Biology, 155(2), pp.193-200.

Faúndez, V., Horng, J. T., & Kelly, R. B. (1998). A function for the AP3 coat complex in synaptic vesicle formation from endosomes. Cell, 93(3), 423-432.

Ford, M.G., Mills, I.G., Peter, B.J., Vallis, Y., Praefcke, G.J., Evans, P.R. and McMahon, H.T., 2002. Curvature of clathrin-coated pits driven by epsin. Nature, 419(6905), pp.361-366.

Fotin, A., Cheng, Y., Sliz, P., Grigorieff, N., Harrison, S.C., Kirchhausen, T. and Walz, T., 2004. Molecular model for a complete clathrin lattice from electron cryomicroscopy. nature, 432(7017), pp.573-579.

Gómez-Llobregat, J., Elías-Wolff, F. and Lindén, M., 2016. Anisotropic membrane curvature sensing by amphipathic peptides. Biophysical journal, 110(1), pp.197-204.

Grassart, A., Cheng, A.T., Hong, S.H., Zhang, F., Zenzer, N., Feng, Y., Briner, D.M., Davis, G.D., Malkov, D. and Drubin, D.G., 2014. Actin and dynamin2 dynamics and interplay during clathrin-mediated endocytosis. Journal of Cell Biology, 205(5), pp.721-735.

Hammarback, J.A., S.L. Palm, L.T. Furcht, and P.C. Letourneau. 1985. Guidance of neurite outgrowth by pathways of substratum‐adsorbed laminin. J. Neurosci. Res. 13:213–220. doi:10.1002/jnr.490130115.

Hayer, A., Shao, L., Chung, M., Joubert, L. M., Yang, H. W., Tsai, F. C., ... & Meyer, T. (2016). Engulfed cadherin fingers are polarized junctional structures between collectively migrating endothelial cells. Nature cell biology, 18(12), 1311-1323.

Heck, H.D.A., 1971. Statistical theory of cooperative binding to proteins. Hill equation and the binding potential. Journal of the American Chemical Society, 93(1), pp.23-29.

Helfrich, W. (1973). Elastic properties of lipid bilayers: theory and possible experiments. Zeitschrift für Naturforschung C, 28(11-12), 693-703.

Henne, W.M., Boucrot, E., Meinecke, M., Evergren, E., Vallis, Y., Mittal, R. and McMahon, H.T., 2010. FCHo proteins are nucleators of clathrin-mediated endocytosis. Science, 328(5983), pp.1281-1284.

Herlo, R., Lund, V.K., Lycas, M.D., Jansen, A.M., Khelashvili, G., Andersen, R.C., Bhatia, V., Pedersen, T.S., Albornoz, P.B., Johner, N. and Ammendrup-Johnsen, I., 2018. An amphipathic helix directs cellular membrane curvature sensing and function of the BAR domain protein PICK1. Cell reports, 23(7), pp.2056-2069.

Hinrichsen, L., Meyerholz, A., Groos, S. and Ungewickell, E.J., 2006. Bending a membrane: how clathrin affects budding. Proceedings of the National Academy of Sciences, 103(23), pp.8715-8720.

Hiraoka, H. 1977. Radiation Chemistry of Poly(methacrylates). IBM Journal of Research and Development, vol. 21, no. 2, pp. 121-130, doi: 10.1147/rd.212.0121.

Hong, S.H., Cortesio, C.L. and Drubin, D.G., 2015. Machine-learning-based analysis in genome-edited cells reveals the efficiency of clathrin-mediated endocytosis. Cell reports, 12(12), pp.2121-2130.

Hussain, S., Wivagg, C. N., Szwedziak, P., Wong, F., Schaefer, K., Izoré, T., & Garner, E. C. 2018. MreB filaments align along greatest principal membrane curvature to orient cell wall synthesis. Elife, 7, e32471.

Inamdar, K., Tsai, F. C., Dibsy, R., de Poret, A., Manzi, J., Merida, P., & Muriaux, D. M. 2021. Full assembly of HIV-1 particles requires assistance of the membrane curvature factor IRSp53. Elife, 10, e67321.

Kane, R.S., S. Takayama, E. Ostuni, D.E. Ingber, and G.M. Whitesides. 1999. Patterning proteins and cells using soft lithography. Biomaterials. 20:2363–2376. doi:10.1016/S0142-9612(99)00165-9.

Kelly, B.T., Graham, S.C., Liska, N., Dannhauser, P.N., Höning, S., Ungewickell, E.J. and Owen, D.J., 2014. AP2 controls clathrin polymerization with a membrane-activated switch. Science, 345(6195), pp.459-463.

Kessels, M.M. and Qualmann, B., 2021. Interplay between membrane curvature and the actin cytoskeleton. Current Opinion in Cell Biology, 68, pp.10-19.

Khan, F. A., & Adesida, I. 1999. High rate etching of SiC using inductively coupled plasma reactive ion etching in SF 6-based gas mixtures. Applied physics letters, 75(15), 2268-2270.

Kleinman, H. K., McGarvey, M. L., Hassell, J. R., Star, V. L., Cannon, F. B., Laurie, G. W., & Martin, G. R. 1986. Basement membrane complexes with biological activity. Biochemistry, 25(2), 312-318.

Kollmann, M., Løvdok, L., Bartholomé, K., Timmer, J. and Sourjik, V., 2005. Design principles of a bacterial signalling network. Nature, 438(7067), pp.504-507.

Koster, G., Cacciuto, A., Derényi, I., Frenkel, D., & Dogterom, M. 2005. Force barriers for membrane tube formation. Physical review letters, 94(6), 068101.

Lin, C. M., Li, C. S., Sheng, Y. J., Wu, D. T., & Tsao, H. K. 2012. Size-dependent properties of small unilamellar vesicles formed by model lipids. Langmuir, 28(1), 689-700.

Lee, D. B. 1969. Anisotropic etching of silicon. Journal of Applied physics, 40(11), 4569-4574.

Lee, I. H., Kai, H., Carlson, L. A., Groves, J. T., & Hurley, J. H. 2015. Negative membrane curvature catalyzes nucleation of endosomal sorting complex required for transport (ESCRT)-III assembly. Proceedings of the National Academy of Sciences, 112(52), 15892-15897.

Lee, M. C., Orci, L., Hamamoto, S., Futai, E., Ravazzola, M., & Schekman, R. 2005. Sar1p N-terminal helix initiates membrane curvature and completes the fission of a COPII vesicle. Cell, 122(4), 605-617.

Lehnert, D., Wehrle-Haller, B., David, C., Weiland, U., Ballestrem, C., Imhof, B. A., & Bastmeyer, M. 2004. Cell behaviour on micropatterned substrata: limits of extracellular matrix geometry for spreading and adhesion. Journal of cell science, 117(1), 41-52.

Levene, M. J., Korlach, J., Turner, S. W., Foquet, M., Craighead, H. G., & Webb, W. W. 2003. Zero-mode waveguides for single-molecule analysis at high concentrations. science, 299(5607), 682-686.

Leyton-Puig, D., T. Isogai, E. Argenzio, B. Van Den Broek, J. Klarenbeek, H. Janssen, K. Jalink, and M. Innocenti. 2017. Flat clathrin lattices are dynamic actin-controlled hubs for clathrin-mediated endocytosis and signalling of specific receptors. Nat. Commun. 8. doi:10.1038/ncomms16068.

Liu, J., Sun, Y., Drubin, D.G. and Oster, G.F., 2009. The mechanochemistry of endocytosis. PLoS biology, 7(9), p.e1000204.

Ma, L., Umasankar, P.K., Wrobel, A.G., Lymar, A., McCoy, A.J., Holkar, S.S., Jha, A., Pradhan-Sundd, T., Watkins, S.C., Owen, D.J. and Traub, L.M., 2016. Transient Fcho1/2 · Eps15/R · AP-2 nanoclusters prime the AP-2 clathrin adaptor for cargo binding. Developmental cell, 37(5), pp.428-443.

Mahapatra, A., Saintillan, D. and Rangamani, P., 2021. Curvature-driven feedback on aggregation-diffusion of proteins in lipid bilayers. arXiv preprint arXiv:2104.01243.

McMahon, H.T. and Boucrot, E., 2011. Molecular mechanism and physiological functions of clathrin-mediated endocytosis. Nature reviews Molecular cell biology, 12(8), pp.517-533.

McMahon, H. T., & Boucrot, E. 2015. Membrane curvature at a glance. Journal of cell science, 128(6), 1065-1070.

McMahon, H. T., & Gallop, J. L. 2005. Membrane curvature and mechanisms of dynamic cell membrane remodelling. Nature, 438(7068), 590-596.

Meinecke, M., Boucrot, E., Camdere, G., Hon, W.C., Mittal, R. and McMahon, H.T., 2013. Cooperative Recruitment of Dynamin and BIN/Amphiphysin/Rvs (BAR) Domain-containing

Proteins Leads to GTP-dependent Membrane Scission. Journal of Biological Chemistry, 288(9), pp.6651-6661.

Milo, R., & Phillips, R. 2015. Cell biology by the numbers. Garland Science.

Moreno-Pescador, G., Florentsen, C. D., Østbye, H., Sønder, S. L., Boye, T. L., Veje, E. L., & Bendix, P. M. 2019. Curvature-and phase-induced protein sorting quantified in transfected cell-derived giant vesicles. ACS nano, 13(6), 6689-6701.

Mornet, S., Lambert, O., Duguet, E., & Brisson, A. 2005. The formation of supported lipid bilayers on silica nanoparticles revealed by cryoelectron microscopy. Nano letters, 5(2), 281-285.

Moskowitz, H.S., Yokoyama, C.T. and Ryan, T.A., 2005. Highly cooperative control of endocytosis by clathrin. Molecular biology of the cell, 16(4), pp.1769-1776.

Motley, A., Bright, N.A., Seaman, M.N. and Robinson, M.S., 2003. Clathrin-mediated endocytosis in AP-2–depleted cells. The Journal of cell biology, 162(5), pp.909-918.

Negulescu, P. A., Krasieva, T. B., Khan, A., Kerschbaum, H. H., & Cahalan, M. D. 1996. Polarity of T cell shape, motility, and sensitivity to antigen. Immunity, 4(5), 421-430.

Ng, M.R., Besser, A., Danuser, G. and Brugge, J.S., 2012. Substrate stiffness regulates cadherin-dependent collective migration through myosin-II contractility. Journal of Cell Biology, 199(3), pp.545-563.

Pechukas, P., 1976. Statistical approximations in collision theory. In Dynamics of molecular collisions (pp. 269-322). Springer, Boston, MA.

Peter, B.J., Kent, H.M., Mills, I.G., Vallis, Y., Butler, P.J.G., Evans, P.R. and McMahon, H.T., 2004. BAR domains as sensors of membrane curvature: the amphiphysin BAR structure. Science, 303(5657), pp.495-499.

Pipathsouk, A., Brunetti, R.M., Town, J.P., Graziano, B.R., Breuer, A., Pellett, P.A., Marchuk, K., Tran, N.H.T., Krummel, M.F., Stamou, D. and Weiner, O.D., 2021. The WAVE complex associates with sites of saddle membrane curvature. Journal of Cell Biology, 220(8), p.e202003086.

Posor, Y., Eichhorn-Grünig, M. and Haucke, V., 2015. Phosphoinositides in endocytosis. Biochimica Et Biophysica Acta (BBA)-Molecular and Cell Biology of Lipids, 1851(6), pp.794-804.

Prévost, C., Zhao, H., Manzi, J., Lemichez, E., Lappalainen, P., Callan-Jones, A., & Bassereau, P. 2015. IRSp53 senses negative membrane curvature and phase separates along membrane tubules. Nature communications, 6(1), 1-11.

Rothberg, K.G., J.E. Heuser, W.C. Donzell, Y.S. Ying, J.R. Glenney, and R.G.W. Anderson. 1992. Caveolin, a protein component of caveolae membrane coats. Cell. 68:673–682. doi:10.1016/0092-8674(92)90143-Z.

Römer, W., Berland, L., Chambon, V., Gaus, K., Windschiegl, B., Tenza, D., Aly, M.R., Fraisier, V., Florent, J.C., Perrais, D. and Lamaze, C., 2007. Shiga toxin induces tubular membrane invaginations for its uptake into cells. Nature, 450(7170), pp.670-675.

Roux, A., Koster, G., Lenz, M., Sorre, B., Manneville, J. B., Nassoy, P., & Bassereau, P. (2010). Membrane curvature controls dynamin polymerization. Proceedings of the National Academy of Sciences, 107(9), 4141-4146.

Rovensky Y.A., Slavnaja I.L., Vasiliev J.M. 1971. Behavior of fibroblast-like cells on grooved surfaces. Exp Cell Res 65:193-201.

Roy, A.R., Zhang, W., Jahed, Z., Tsai, C.T., Cui, B. and Moerner, W.E., 2021. Exploring cell surface-nanopillar interactions with 3D super-resolution microscopy. bioRxiv.

Schizas, C. and Karalekas, D., 2011. Mechanical characteristics of an Ormocomp biocompatible hybrid photopolymer. Journal of the mechanical behavior of biomedical materials, 4(1), pp.99-106.

Schmidt, N. W., Tai, K. P., Kamdar, K., Mishra, A., Lai, G. H., Zhao, K., & Wong, G. C. 2012. Arginine in α-defensins: differential effects on bactericidal activity correspond to geometry of membrane curvature generation and peptide-lipid phase behavior. Journal of Biological Chemistry, 287(26), 21866-21872.

Senefelder, Alois. 1911. The History of Lithography. Fuchs and Lang Manufacturing Company, NY. 229pp.

Shahal, T., Melzak, K.A., Lowe, C.R. and Gizeli, E., 2008. Poly (dimethylsiloxane)-coated sensor devices for the formation of supported lipid bilayers and the subsequent study of membrane interactions. Langmuir, 24(19), pp.11268-11275.

Shukla, S., Jin, R., Robustelli, J., Zimmerman, Z. E., & Baumgart, T. (2019). PIP2 reshapes membranes through asymmetric Desorption. Biophysical journal, 117(5), 962-974.
Snead, D., Wragg, R. T., Dittman, J. S., & Eliezer, D. (2014). Membrane curvature sensing by the C-terminal domain of complexin. Nature communications, 5(1), 1-10.

Sitarska, E., Almeida, S. D., Beckwith, M. S., Stopp, J., Schwab, Y., Sixt, M., ... & Diz-Muñoz, A. (2021). Sensing their plasma membrane curvature allows migrating cells to circumvent obstacles. bioRxiv.

Snead, W. T., & Stachowiak, J. C. 2018. A Tethered Vesicle Assay for High-Throughput Quantification of Membrane Fission. Methods in enzymology, 611, 559-582.

Snead, W.T., Zeno, W.F., Kago, G., Perkins, R.W., Richter, J.B., Zhao, C., Lafer, E.M. and Stachowiak, J.C., 2019. BAR scaffolds drive membrane fission by crowding disordered domains. Journal of Cell Biology, 218(2), pp.664-682.

Sokac, A.M., C. Co, J. Taunton, and W. Bement. 2003. Cdc42-dependent actin polymerization during compensatory endocytosis in Xenopus eggs. Nat. Cell Biol. 5:727–732. doi:10.1038/ncb1025.

Stachowiak, J. C., Brodsky, F. M., & Miller, E. A. 2013. A cost–benefit analysis of the physical mechanisms of membrane curvature. Nature cell biology, 15(9), 1019-1027.

Sweitzer, S.M. and Hinshaw, J.E., 1998. Dynamin undergoes a GTP-dependent conformational change causing vesiculation. Cell, 93(6), pp.1021-1029.

Thompson, L.F. 1983. An Introduction to Lithography. ACS Symposium Series, Vol. 219. Ch1 pp1-13. DOI:10.1021/bk-1983-0219.ch001.

Tian, A., & Baumgart, T. 2009. Sorting of lipids and proteins in membrane curvature gradients. Biophysical journal, 96(7), 2676-2688.

Traub, Linton M. "Sorting it out AP-2 and alternate clathrin adaptors in endocytic cargo selection." Journal of Cell Biology 163, no. 2 (2003): 203-208.

Tseng, A. A. 2008. Nanofabrication: fundamentals and applications. World Scientific.

Ungewickell, E. and Branton, D., 1981. Assembly units of clathrin coats. Nature, 289(5796), pp.420-422.

Wang, B., Ho, J., Fei, J., Gonzalez Jr, R.L. and Lin, Q., 2011. A microfluidic approach for investigating the temperature dependence of biomolecular activity with single-molecule resolution. Lab on a Chip, 11(2), pp.274-281.

Waugh, R. E., Song, J. , Svetina, S., & Zeks, B. 1992. Local and nonlocal curvature elasticity in bilayer membranes by tether formation from lecithin vesicles. Biophysical journal, 61(4), 974-982.

Wehbi, H., Feng, J., Kolbeck, J., Ananthanarayanen, B., Cho, W., and Roberts, M. F. 2003. Investigating the interfacial binding of bacterial phosphatidylinositol-specific phospholipase C, Biochemistry 42, 9374−9382.

Westphal, C.H. and Chandra, S.S., 2013. Monomeric synucleins generate membrane curvature. Journal of Biological Chemistry, 288(3), pp.1829-1840.

Whitesides, G.M., E. Ostuni, X. Jiang, and D.E. Ingber. 2001. Soft Lithography in Biology. Annu. Rev. Biomed. Eng. 3:335–73.

Wolf, E. D. 1989. Nanofabrication: Opportunities for interdisciplinary research. Microelectronic Engineering, 9(1-4), 5-11.

Wollert, T., & Hurley, J. H. 2010. Molecular mechanism of multivesicular body biogenesis by ESCRT complexes. Nature, 464(7290), 864-869.

Wood, Katherine M., and Corinne J. Smith. "Clathrin: the molecular shape shifter." Biochemical Journal 478, no. 16 (2021): 3099-3123.

Wu, C. and Dedhar, S., 2001. Integrin-linked kinase (ILK) and its interactors: a new paradigm for the coupling of extracellular matrix to actin cytoskeleton and signaling complexes. The Journal of cell biology, 155(4), pp.505-510.

Wu, C. S., Makiuchi, Y., & Chen, C. 2010. High-energy electron beam lithography for nanoscale fabrication, pp. 41-266. InTech Europe: Rijeka, Croatia.

Yarar, D., Waterman-Storer, C.M. and Schmid, S.L., 2005. A dynamic actin cytoskeleton functions at multiple stages of clathrin-mediated endocytosis. Molecular biology of the cell, 16(2), pp.964-975.

Ye, Y., Tyndall, E.R., Bui, V., Tang, Z., Shen, Y., Jiang, X., Flanagan, J.M., Wang, H.G. and Tian, F., 2021. An N-terminal conserved region in human Atg3 couples membrane curvature sensitivity to conjugase activity during autophagy. Nature communications, 12(1), pp.1-11.

Yu, H. D., Regulacio, M. D., Ye, E., & Han, M. Y. (2013). Chemical routes to top-down nanofabrication. Chemical Society Reviews, 42(14), 6006-6018.

Zeno, W. F., Baul, U., Snead, W. T., DeGroot, A. C., Wang, L., Lafer, E. M., & Stachowiak, J. C. 2018. Synergy between intrinsically disordered domains and structured proteins amplifies membrane curvature sensing. Nature communications, 9(1), 1-14.

Zeno, W. F., Hochfelder, J. B., Thatte, A. S., Wang, L., Gadok, A. K., Hayden, C. C. & Stachowiak, J. C. 2021. Clathrin senses membrane curvature. Biophysical Journal, 120(5), 818-828.

Zhao, Y., Liu, J., Yang, C., Capraro, B. R., Baumgart, T., Bradley, R. P., ... & Guo, W. 2013. Exo70 generates membrane curvature for morphogenesis and cell migration. Developmental cell, 26(3), 266-278.

Zhao, H., Michelot, A., Koskela, E.V., Tkach, V., Stamou, D., Drubin, D.G. and Lappalainen, P., 2013. Membrane-sculpting BAR domains generate stable lipid microdomains. Cell reports, 4(6), pp.1213-1223.